Static and Fatigue Behaviour of FRP-Reinforced Concrete Beams and a SHM System with Fiber Optic Sensors under Different Weathering Conditions

Arash Rahmatian

A Thesis
In the Department
of
Building, Civil and Environmental Engineering

Presented in Partial Fulfillment of the Requirements
For the Degree of
Doctor of Philosophy (Civil Engineering) at
Concordia University
Montreal, Quebec, Canada

April 2014

CONCORDIA UNIVERSITY

SCHOOL OF GRADUATE STUDIES

This is to certify that the thesis prepared

By: **Arash Rahmatian**

Entitled: **STATIC AND FATIGUE BEHAVIOUR OF FRP-REINFORCED CONCRETEBEAMS AND A SHM SYSTEM WITH FIBER OPTIC SENSORSUNDERDIFFERENT WEATHERING CONDITIONS**

and submitted in partial fulfillment of the requirements for the degree of

DOCTOR OF PHILOSOPHY (Civil Engineering)

Complies with the regulations of the University and meets the accepted standards with

respect to originality and quality. Signed by the final examining committee:

_____Dr. Martin Pugh_____ _____Chair

_____Dr. Brahim Benmokrane_____External Examiner

_____Dr. Mamoun Medraj_____External to Program

_____Dr. Khaled Galal_____Examiner

_____Dr. Lan Lin_____Examiner

_____Dr. Ashutosh Bagchi and Dr. Michelle Nokken_____Thesis Supervisors

Approved by

_____Chair of department or graduate program director

_____Dean of faculty

ABSTRACT

Static and Fatigue Behaviour of FRP-Reinforced Concrete Beams and a SHM System with Fiber Optic Sensors under Different Weathering Conditions

Arash Rahmatian, Ph.D.
Concordia University, April 2014

Structural Health Monitoring (SHM) techniques are often used for detecting damage and diagnosing the structural conditions. Fibre Optic Sensors (FOS) are found to be very accurate and durable for outdoor applications including embedment in reinforced concrete structures. However, there are many issues related to installation and constructability of SHM systems and in-situ installation of FOS on rebars in reinforced concrete (RC) elements, especially when Fibre Reinforced Polymer (FRP) bars are used as reinforcements.

Here, a solution is provided for installation of a FOS strain sensor by mounting it on a supplementary bar *a priori* and then attaching it to the main reinforcing bar of interest at the construction site prior to concrete pouring. Such innovative deployment system for FOS is particularly advantageous for developing a practical SHM system for infrastructure. However, the performance of such systems under various loading and climatic conditions is not very well known. The objective of this research is to assess the performance of the said system used in concrete beams reinforced with FRP bars, under normal and adverse environmental conditions.

A set of twelve specimens with and without exposure to various environmental conditions have been tested under static and fatigue loads to determine the effectiveness of the sensing system in these conditions. Apart from measuring the response quantities like strain and

deformation, the Scanning Electron Microscopy (SEM) technique has been used to determine the effect of the adverse environmental conditions on the rebars. In addition, numerical modeling of the beams using the Finite Element Method (FEM) has been applied to carry out a parametric study on the effect of the properties of concrete and the bar sizes on the performance of the above sensing system.

From the present study, it is observed that the proposed system works well in terms of capturing the strain under static and fatigue conditions in normal and adverse environmental conditions. However, the performance of the sensing system degrades in the case of alkaline immersion. The outdoor or wet and dry conditions do not affect the performance of the system.

Table of Contents

Table of Figures

List of Tables

List of Symbols

a	Height of the cross section
b	Width of cross section
C_E	Environmental reduction factor
d_c	Concrete cover measured from the centroid of tension reinforcement to the extreme tension surface in mm
e_1 , e_2	Strain measured at the mid-span and at a quarter-span
E_f	Modulus of elasticity of FRP
f_u^*	Guaranteed tensile strength of the FRP
k_b	Bond-dependent coefficient
f'_c	Compressive strength of concrete
F_r	Concrete modulus of rupture
F_u	Design tensile strength of the FRP
I_{cr}	Moment of inertia of fully cracked section
I_e	Effective moment of inertia
I_g	Moment of inertia of the gross section
L	Cyclic strain span
L_d	Length of development
M_{exp}	Flexural capacity of the beams obtained from the tests
M_n and M_r	Nominal and factored flexural capacities
P	Applied mid-point load

R1 The lower bound cyclic residual strain

R2 The upper bound cyclic residual strain

s Longitudinal FRP bar spacing

V_f Factored shear resistance

w Crack width

y Distance from the neutral axis

$\varepsilon_{FRP,u}$ Ultimate tensile strain of the GFRP

γ_c Poisson's ratio

λ Concrete density

$\mu\varepsilon$ Microstrain

ρ_{FRP} GFRP reinforcement ratio

τ Shear stress

β Ratio of the distance from the neutral axis to the extreme tension fiber to the distance from the neutral axis to the center of the tensile reinforcement

List of Abbreviations

BSE	Back Scattered Electron
CDP	Concrete damage plasticity
CMOD	Crack mouth opening displacement
Controlf	Control conditioning and fatigue loading
CSC	Concrete smeared crack
EDX	Energy Dispersive X-ray Spectroscopy
ESG	Electrical strain gauge
ESG-L	Electrical strain gauge at the left quarter span
ESG-M	Electrical strain gauge at the mid-span
ESG-R	Electrical strain gauge at the right quarter span
FBG	Fiber Bragg Grating
FOS	Fiber optic sensor
FOS-M	Fiber optic sensor mounted on main FRP rebar
FOS-S	Fiber optic sensor mounted on supplemental FRP rebar
FRP	Fiber reinforced polymer

Imm Immersion condition

Immf Immersion conditioning and fatigue loading

Outdoorf Outdoor conditioning and fatigue loading

RT Room temperature

SEM Scanning Electron Microscope

Theoretical-M Theoretical value for middle sensor

Theoretical-R&L Theoretical value for right and left sensor

TRS Total residual strain

WDX Wavelength Dispersive X-ray Spectroscopy

W&D Wet and dry condition

W&Df Wet and dry conditioning and fatigue loading

1. Introduction

1.1. General

The increased usage of fiber-reinforced polymers (FRP) in structural concrete applications is partly due to their high strength, light weight, and high resistance to deterioration. Although there has been some research on various aspects of this relatively new composite material for the use in civil engineering structures, further research is needed to confirm the serviceability and safety performance of these materials in civil infrastructure applications. Since the use of FRP materials in civil infrastructure applications is relatively new, it is often accompanied by structural health monitoring (SHM), particularly in bridges, to assess the structural performance and ascertain the structural reliability. SHM methods are not standardized and present some issues related to choice of sensors, installation process, design and constructability of the sensing systems that remain to be resolved. Fiber optic sensors (FOS) offer an improvement over traditional electrical strain gauges, in terms of accuracy and durability. However, the former are difficult to install, as the bare fibre sensor is very fragile and brittle. In this research, a method of strain monitoring will be investigated that incorporates mounting fiber optic strain sensors (FOSs) on a supplementary bar which would be connected to the main reinforcement bar during construction. The installation of the FOSs on a supplementary bar represents an improvement in

construction practice by protecting and ruggedizing the FOS, and simplifying the installation process. A supplemental bar pre-installed with FOSs as mentioned above, can be quickly attached to the main reinforcements on site prior to concrete placement and will provide adequate protection the sensors and accessories. Such an innovative deployment system for FOSs is particularly advantageous for developing a practical SHM system for durable civil infrastructure such as bridges. This system was originally proposed by Bagchi et al. (2007) and the preliminary results on the performance of such systems in FRP-reinforced concrete beams under static load were presented in Bagchi et al. (2010). Further study on such systems with different lengths and diameters for the supplementary and main bars, as well as for different attachment methods was reported in Torkan (2010), which showed the viability of such systems and also established important design parameters. However, the performance of such systems under fatigue and environmental distress is not yet known. For its practical application in structures like bridges, it is important to establish the long-term reliability of the system under such conditions.

1.2. Advantages of Sensors mounted on Supplemental Reinforcements

Periodic visual inspection is the common method of detecting problems in concrete infrastructure, particularly bridges. These inspections can only detect deterioration after it has reached certain levels. A better understanding of the real behaviour of a structure can be achieved by an easily adoptable, appropriate monitoring system which would help to diagnose the structural conditions and appropriate measures could be taken to prevent failure. The lack of real time assessment of the behaviour of structures under different loading conditions such as gusty winds, earthquake, settlement, heavy traffic loading, deterioration, stress relaxation and so

on makes it even more important to assess the effectiveness of current practices. Even though SHM has developed substantially in the past few years and new technologies for sensing and data acquisition have been helpful in this direction. However, the available studies on the application of fibre optic sensors in reinforced concrete structures have revealed some issues related to the installation and constructability (Benmokrane & Debaiky, 2005). It is difficult to assure a high level of workmanship for sensor installation and the attachment of a sensor, particularly in the case of heavily congested reinforcement.

It should be mentioned that there are some commercially available FRP reinforcing bars that are integrated with fibre optic sensors. These sensor-integrated rebars can potentially be used in SHM solutions and they could be placed among other reinforcements in a RC structure just prior to pouring of concrete. Although such embedded sensor-reinforcement systems appear simpler than the attachment of sensor-integrated supplementary bars, there are several disadvantages with those systems as outlined below:

- Ordering a special length of instrumented rebar in limited numbers would be expensive.
- Changes in the planning and the required reordering and shipment delays would be time consuming and incur extra costs.
- Defining a specific location for each embedded-sensor-rebar in the job site requires highly skilled and accurate workers to follow the plan.
- A rebar's location, once installed, cannot be changed.
- The covers for a sensor and its wires are unsafe during the period between the installation of the sensor-bar and pouring of concrete.

On the other hand, the advantages of using supplementary bars in SHM include the following:

- Fast and safe installation at the last minute prior to casting of the concrete.
- Changing the monitoring location prior to placing concrete is simple and easy.
- No specialized factory orders or shipment costs and time, only the sensors and accessories must be available.
- No need for workers with specific skills, at the time of installation.
- Low cost compared to embedded sensor rebars

1.3. Research objectives and strategy

The proposed research has the following main objectives:

- To study the mechanical performance of pre-installed FOSs on a supplementary FRP reinforcement bar attached to the main FRP bar, and compare the results to more traditional electrical strain gauges.
- To study the impact of fatigue, weathering, and alkaline solution on this attachment and on the behaviour of the FRP-reinforced concrete beams and the FOS strain sensors.
- To study the effects of alkaline solution on the FRP reinforcements.
- To develop a finite element model of a test sample to correlate it with the experimental results as well as to study the effect of the key parameters affecting the performance of the supplemental bar-sensor system.

To test the sensor system and the composite material in realistic environments, beam specimens will be subjected to three conditions in addition to a control: outdoor exposure (including natural cyclic freezing), continuous immersion in a highly alkaline solution, and cyclic immersion in the same alkaline solution (with periods of drying). As a very limited number of studies are available on the fatigue behaviour of FRP bars embedded in concrete, this research adds valuable knowledge and combines several novel contributions to the field.

1.4. Outline of this thesis

This thesis consists of eight chapters. Chapter 1 gives an introduction to the topic and explains the scope of the work. Chapter 2 introduces structural health monitoring and briefly reviews bonding, the influence of exposure conditions and of fatigue in relation to FRP performance. The design methodology, the experimental tests and their set ups are described in Chapter 3.

Chapter 4 presents the results of the static tests with details on the FOS strain in both main and supplemental bars under different conditions. The failure modes and results from electrical strain gauges at three locations along with their bond calculations are also covered in this chapter. Chapter 5 specifies the use of SEM to measure the penetration of alkalis into bare and embedded FRP reinforcements. Chapter 6 presents the numerical modeling utilized, and proposes a model for parametric study. In Chapter 7, fatigue is investigated under one million cycles at different conditionings, with crack width, bond level, integrity of the sensors, and the deflection at the beam mid-span all recorded. A formula is suggested for determining beam lifespan under different conditions. Chapter 8 gives an overall discussion and conclusions of this research as well as some recommendations for future work.

2. Literature Review

2.1. Introduction

The combination of high strength, light weight and good resistance to corrosion has made FRP application very popular today. As well, inspection of structures with use of sensor technology has expanded as a domain of research. There are some weaknesses in FRP and difficulties of the installation of sensors in concrete structures. This chapter reviews literature in the topics relevant to the research; Structural Health Monitoring, issues of bond and deterioration of FRP as well as fatigue in FRP reinforced concrete.

2.2. Structural Health Monitoring (SHM)

Structural health monitoring (SHM) and damage detection deployment has increased in recent years due to concerns about the aging and deterioration of civil infrastructure. Traditionally this task has been done by visual inspection and simple non-destructive tests, such as the tap test. Depending on the agency, this job is done at a frequency of at best once per year for bridges and less often for other structures. Non-destructive evaluation methods, such as the tap test, are called local health monitoring and are performed at specific, isolated locations, which can be time consuming, costly and sometimes impossible due to access issues. Global health monitoring refers to the monitoring of the current service condition of an entire structure, typically using

SHM techniques. As SHM cannot currently pinpoint the location or degree of damage, both local and global health monitoring techniques assist engineers in making timely repair decisions (Chang et al., 2003). Figure 2-1 shows the benefits of SHM as compared to visual inspection. SHM techniques have been studied over the last thirty years, and this method has had some success in determining likely damage occurrences. Generally these methods are more helpful when damage has already progressed to a specific level. Some attempts to improve damage detection by the application of FOSs and control theory have been carried out Chang et al. (2003).

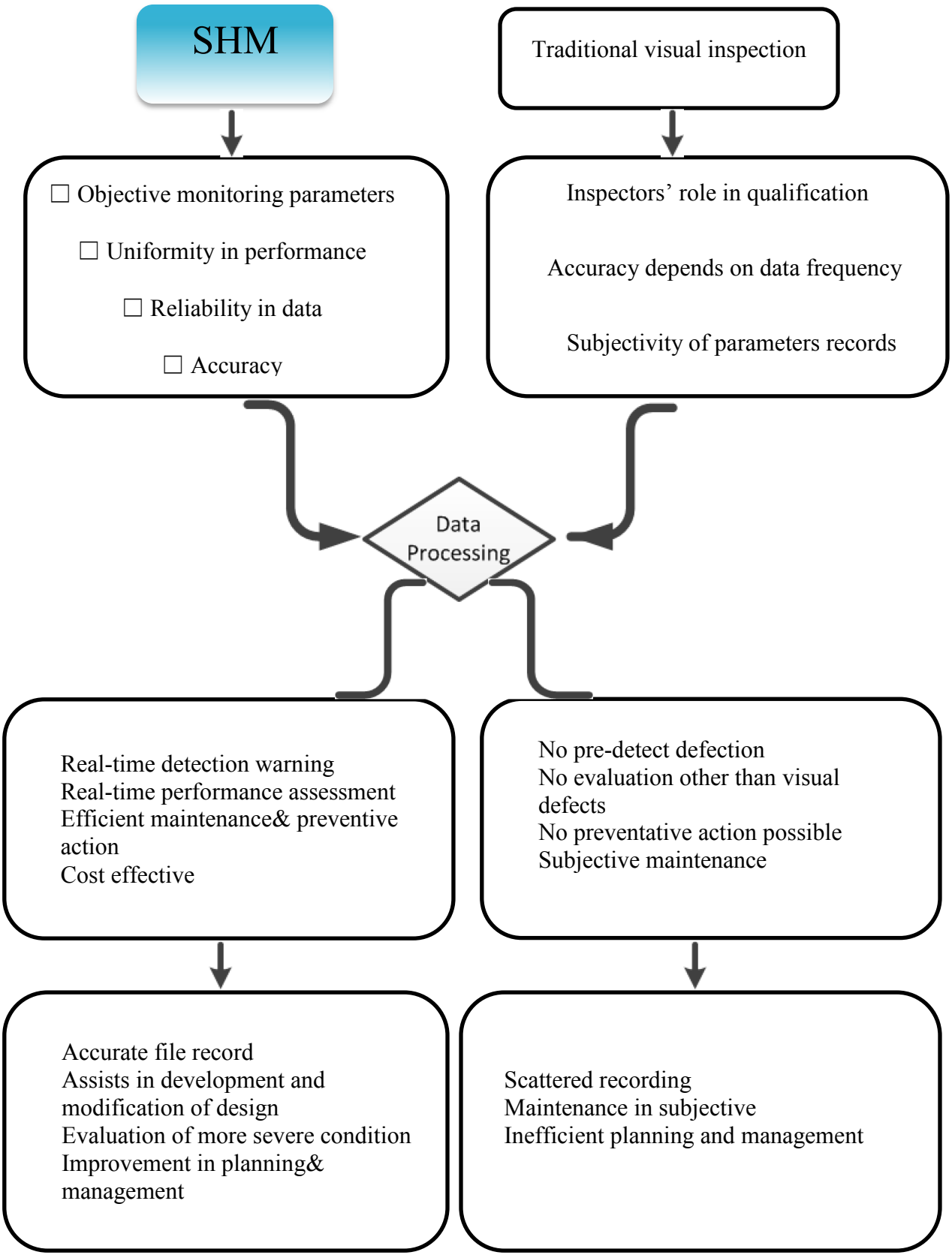

Figure 2-1 SHM and traditional methods of inspection (CISC Magazine, 2013)

Recent advances in sensing and data acquisition technologies and the integration of electrical engineering with civil engineering have made effective implementation of structural health monitoring possible. The objective of Structural Health Monitoring is to monitor the in-service performance of a structure to verify its integrity with regard to the response quantities such as, stress, strain and cracks under operating and unexpected loading conditions. SHM systems are expected to provide appropriate information the behaviour of structures that would help to prevent catastrophic failures and service disruption, and reduce maintenance costs (ISIS, 2007). Strains in the reinforcing bars are of great interest to be measured so that the stresses at desired locations can be calculated. SHM systems can also help engineers minimize service interruptions, develop effective maintenance or repair schedules, and estimate the remaining service life of a structure (ISIS, 2007).

2.2.1. Fibre Optic Sensor (FOS) and FRP

Fiber optic sensors are made from glass and nonconductive dielectric material. The other specification of them is resistance to electrical current and radio or microwaves from nature (e.g., electrical shocks from storms and solar activity) or from manmade sources (Foote ,2009). Fiber optic sensors have been used for SHM for the last three decades; but only a few papers deal with their conditions in other than static loading. Zhang et al. (2003) assessed the impact of Fabry-Pérot Fiber Optic Sensors and electrical strain gauges in measuring strain in GRFP rebar, steel and CFRP grids. They used pre-installed FOSs on the reinforcement to monitor the thermal behavior and static and cyclic loading. The results showed that the FOS sensors performed well in static and dynamic loading and that strain changed linearly under tension and compression. Gheorghiu et al. (2004) performed research on the effect of monotonic and consequential fatigue

loading on the performance of Fabry-Pérot FOSs bonded onto CFRP plates used to externally strengthen reinforced concrete beams. The results indicated that the FOSs precisely measured the strain up to 4000με, and that the load amplitude and the number of fatigue cycles had no influence on the FOS readings for strains smaller than 3300με and a number of cycles less than two million. It was also revealed that the FOSs accurately measured monotonic strains after fatigue cycling. Overall, these test results confirmed the reliability of FOSs in measuring strain for a variety of loadings, loading magnitudes and fatigue cycles. Ruscito et al. (2008) studied on self-monitoring reinforcing composite rods and Sim et al. (2005) carried out application of FBG sensor in FRP and found the strain readings by sensors correlated to the applied load.

Kuang et al. (2004) studied the durability and feasibility of embedded Fabry–Pérot FOS under adverse conditions, including an accelerated corrosion environment. These sensors exhibited excellent durability throughout the study with no notable decrease in performance. Benmokrane et al. (2000) applied FBG on a bridge deck and found FBG results reliable for short and long term (Figure 2-2). Benmokrane et al. (2005) reported the application of FOS in the field test of Val Alain Bridge on Highway 20 East (Québec) and found that difference in the size between the original bars and the instrumented one can lead to errors in strain readings and emphasized importance of placement of instrumented bar at the level of original reinforcement.

Fiber Bragg Grating (FBG) type of FOS are increasingly becoming popular for their small size, flexible applications, dynamic measurement and multiplexing abilities. While the performance of

FBG sensors under static loads has been reported earlier, there is no study available on their fatigue and post-fatigue behaviour.

The thickness of FBG sensors is close to the thickness of human hair which makes their installation very difficult as they are prone to fracture and breakage. Bagchi et al. (2010) proposed a sensor protection system in which a supplementary bar is attached to the main FRP bar. An experimental study was conducted on the performance of Fiber Bragg Grating (FBG) sensors embedded in the epoxy filled grooves of FRP attached at the mid-span of a simply supported reinforced concrete beam. For the sake of comparison, electrical strain gauges (ESGs) were attached at the same longitudinal location of the main bar. The strain recorded by the electrical strain gauges and by the rugged FOSs showed a good agreement. This proposed protection system was further developed by Torkan (2010), where a set of static tests were conducted to characterize the length and size of the FOS-mounted supplemental bar and different mechanisms for attaching it to the main rebar. However, there is no study available on the performance of such systems under fatigue loading or various environmental effects such as freeze-thaw or alkaline exposure. The performance of such sensor systems will be further studied in the proposed research.

Figure 2-2 Instrumented CFRP grid during the installation (Benmokrane et al., 2000)

2.3. The Bond between FRP bar and Concrete

Bond characteristics affect the anchorage of bars, the strength of lap splices, the required concrete cover, and the serviceability and ultimate stress states. The continued integrity of the bond is also a critical issue for the long lasting performance of concrete structures reinforced with FRP bars. Larger diameter bars develop less bond strength, possibility due to more shear lag and the Poisson effect (Achillides & Pilakoutas, 2004). Bond properties of FRP bars depend on the surface preparation of the bar, which may be sand coated, ribbed, helically wrapped, or braided. Friction, adhesion and mechanical interlock all transfer bond forces between reinforcement and concrete. Unlike steel-reinforced concrete, the compressive strength of concrete has no influence on the bond of FRP bars.

Two bond mechanisms for GFRP rebars have been defined: friction resistant and bearing-resistant (mechanical interlock) (Hao et al., 2007). Friction-resistant mechanisms are predominant in smooth and sand-coated GFRP rebars, while bearing-resistant mechanisms are available in deformed rebars, including glued on spirals, twisted fiber strands, and rib and

indented rebars. The results from this study show that the bond of smooth FRP rebars are inadequate for use as concrete reinforcement. Sand-covered continuous fiber rebars showed bond resistance under friction. However, the adhesion between the sand grains and the bars can fail abruptly, leading to brittle failure.

The sources of FRP bond deterioration can originate from alkaline attack and thermal expansion. Alkaline attack occurs at the interface of the concrete and a FRP reinforcing bar with the resulting damage to the matrix of the FRP bar, which results in the degradation of the FRP bar in terms of force-transfer (Davalos et al., 2008). There also may be incompatibility in the coefficient of thermal expansion (CTE) in two directions (longitudinal and transverse), which may cause further deterioration of the bond strength. The effects of alkalis will be treated more in Section 2.5; thermal expansion will not be discussed further.

In an extensive experiment by Katz, (2000), six different FRP bars were tested for pull-out under monotonic and cyclic loading. Aging (at 20 °C and 60 °C in water) was considered for all samples and the bond after cyclic loading was investigated. The results of the tests showed that the type of resin is important; for example, FRP bars with polyester absorbed water, partially dissolving and retarding cement hydration in this area causing a weak bond at the interface of FRP and concrete. Temperature had no serious effect on the bond strength results except with steel rebars. It was also found that sand surfaces performed better than helical wrapping.

Pan and Leung (2007) determined that the bond capacities of RC-FRP beams are mostly dependent on the aggregate content. The ultimate bond capacity was found to increase with increasing concrete aggregate content (Figure 2-3).

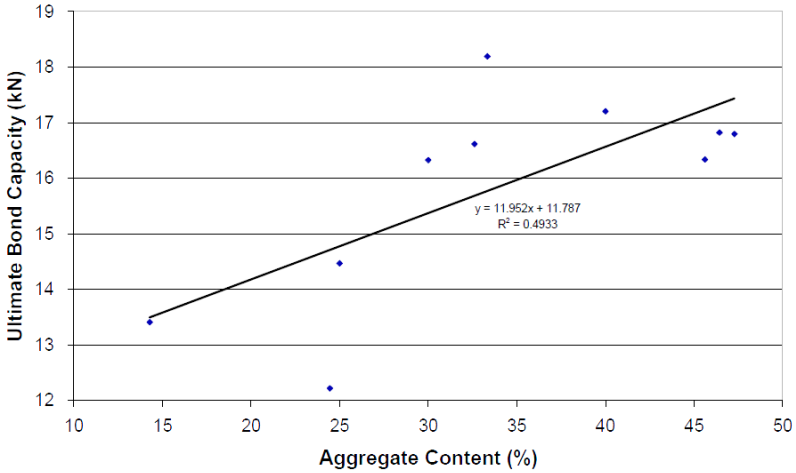

Figure 2-3 Bond and aggregate content relationship (after Pan & Leung, 2007)

2.4. Degradation of Fiber Reinforced Polymer (FRP) bars

FRP bars have been used for structural engineering applications since 1970. Fiber reinforced polymers (FRPs) are composite materials containing two parts: resin (matrix) and fiber, which may be made of aramid, polyvinyl, carbon and improved glass fiber. The strength of the fiber is more than that of the resin and the fiber-volume fraction (volume of fiber to the overall volume of the FRP) significantly affects the tensile properties of an FRP bar (American Concrete Institute, 2006).

Most of the negative factors which limit the life of a structure are corrosion, fatigue, weathering, and creep. Corrosion is one of the most noticeable problems of steel reinforced concrete beams in harsh environments. FRP bars have good resistance to corrosion as well as a higher stiffness to weight ratio and they offer a high degree of handling ease. However, FRPs do have some weaknesses, as they are prone to degradation by hydrolysis, and moisture can decrease their strength (Micelli & Nanni, 2004; ISIS, 2007). The majority of studies have shown that degradation of FRP under alkaline conditions is more severe than the effect of water; however, over time both have almost similar degradation effects (Chu & Karbhari, 2002).

The damage mechanisms for the long term behavior of FRP can be classified as follows (Micelli & Nanni, 2004):

- Fluid absorption and its influence on physical and mechanical properties;
- Creep and stress relaxation;
- Fatigue and environnemental fatigue; and
- Weathering.

External agents, such as those listed below, can create this mechanical degradation (Micelli and Nanni, 2004):

- Moisture and aqueous solutions;
- Alkaline environment;
- Thermal effects (Freeze-thaw, cycling, high temperature);
- Fatigue loading;
- Ultra-violet radiation (UV); and
- Fire.

Bott and Barker (1969) suggested a relation between the rate of fluid absorption and the rate of degradation of environmental exposure. Years later, researchers determined that the absorption of polymer composites is dependent upon the type of fluid, fluid concentration, temperature, applied stress, damage status, and chemical structure of the matrix and fiber/matrix interface. (Chateauminois et al., 1993; Liao et al., 1998).

2.4.1. Effect of Alkali on FRP

Typically, concrete has high alkalinity, in the range of 12.4–13.7 pH (Chen et al., 2007), which is dependent upon the design mixture and the type of cement used (Diamond, 1981). The hydroxyl ion concentration in fresh concrete is partly due to the presence of calcium hydroxide, $Ca(OH)_2$, which in a saturated solution gives a pH value of about 12.4. Higher pH values are due to the hydroxyl ions from sodium and potassium hydroxides (NaOH and KOH). This alkaline environment damages glass fibers in FRPs, leading to a loss in toughness and strength due to their embrittlement. As stated above, FRPs do not show good resistance to alkaline solutions and they are recommended to be used cautiously in such conditions. At present, the principal concern for GFRP bars is the potential degradation caused by the interstitial concrete solution (Nkuruziza et al. 2005). Resins used in FRP are susceptible to alkaline attack, while they have good resistance to water, but in real structures, the presence of groundwater, soils and concrete pore water all contribute to creating a natural condition of alkalinity.

Recently, extensive research has been performed regarding the deterioration and behaviour of FRP bars in alkaline solutions, especially in terms of the fatigue-resistance and durability of RC beams reinforced by FRP bars (Morris & Garrett, 1981; Jungkuist, 2000; Chu & Karbhari, 2002;

Karbhari, et al., 2003; Pan & Leung, 2007;Robert, Cousin, & Benmokrane, 2009) and others, but some gaps remain to be covered.

Research on the effect of alkali on GFRP concluded that GFRP is prone to degradation in direct contact with concrete (Malvar, 1998). Several research studies have been carried out to investigate the durability of GFRP materials under different environmental conditions that are anticipated under actual service conditions (Robert, Cousin, & Benmokrane, 2009). One problem with these studies is that they subjected GFRP to accelerated degradation by increasing the temperature in order to shorten the study time. However, a major study investigated the durability of GFRP reinforcement under real job site conditions and found no serious degradation of GFRP over 5-8 years (Mufti et al., 2007). The findings from the SEM analyses confirmed that the concerns about the durability of GFRP in alkaline concrete, based on simulated laboratory studies in alkaline solutions, were unfounded. They found that the glass fibers and the GFRP/concrete interface remained intact.

The strength reduction factors adopted by current codes and guidelines are conservative. Based on these research studies, it appears that those tests where FRP conditioning was carried out by elevated temperature and high pH solution samples embedded in concrete were not based on valid assumptions. Regardless of the statements regarding accelerated testing, it is important to review the findings of these studies. Based on studies done by exposing FRPs to tap water and to simulated environments of high-performance concrete (12.7 pH) and normal-strength concrete (13.5 pH), degradation of GFRP bars in alkaline solutions, particularly those at higher temperatures, was found to be more severe than that in unexposed concrete (Chen et al., 2007).

This severe degradation is due to the high alkalinity and the high mobility of OH ions (Swit, 2000; Tannous & Saadatmanesh, 1998). High temperature (40 °C and 60 °C) was found to decrease the strength of samples exposed to tap water.

It was found that bare GFRP bars and bars embedded in concrete showed a significant strength loss when exposed to simulated environmental conditions, especially to alkaline solutions at high temperatures (60 °C). Tables 2-1 shows the effect of different environmental conditions on the tensile strength of bare FRP bars at room temperature of 22 °C, elevated temperature (40 °C and 60 °C), and Wet-and-Dry (W&D) condition. On the other hand, Table 2-2 shows the effect of various environmental conditions on the bond and shear strength of bare FRP bars. In Table 2-2, "Environmental Exposure" indicates a combination of cyclic temperature from -18 to +17 °C with various humidity levels. The residual bonding strength of all the FRP rebar specimens decreased by 20% after they were exposed to 60 °C for 50 days (Won & Park, 2006). The shear strength of GFRP showed the same reduction in strength due to the resin weakness, similar to that of tensile strength (Micelli & Nanni, 2004).

The following results describe the reduction factor related to the alkaline effect on bonds and on bare FRP bars. According to the ACI 440.2R (American Concrete Institute, 2011), the design tensile strength is given by the following expression,

Equation 2-1 $$F_u = C_E f_u^*$$

where F_u is the design tensile strength of the FRP in MPa, C_E is the environmental reduction factor that depends on the types of fibers and environmental exposure (values of this coefficient are provided in Table 2-3 and f_u^* is the guaranteed tensile strength of the FRP reinforcement.

Table 2-1 Relative tensile strength of embedded FRP bars exposed to various conditions (Chen et al., 2007)

Type of exposure	**W&D (72 days)**	**22 °C (120 days)**	**40 °C (70 days)**	**60 °C (70 days)**
Tap water	84%	95%	97%	71%
Simulated Pore solution (pH 13.6)	72%	86%	89%	64%
Simulated Pore solution (pH 12.7)	80%	92%	92%	73%

Table 2-2 Effect of Environmental conditions on the strength of bare FRP

Type of exposure	**Environmental Exposure**	**Imm 60°C (21 days)**	**Imm 60°C (60 days)**
Micelli & Nanni (2004) shear strength	90%	70%	60%
Type of exposure	**W&D**	**Imm 60°C (50 days)**	**FT**
Won & Park (2006) bond strength	92%	80%	85%

Table 2-3 Environmental reduction factors, C_E (after American Concrete Institute, 2011)

Exposure conditions	Type of fiber	C_E
Concrete not exposed to moisture or not in contact with the ground	Carbon	1
	Glass	0.8
	Aramid	0.9
Concrete exposed to moisture or in contact with the ground	Carbon	0.9
	Glass	0.7
	Aramid	0.8

2.4.2. Effect of Water on FRP

The migration of moisture into composite materials depends on the type of resin and the surrounding environment. Moisture diffuses into composite materials at various rates at the molecular level. Moisture can be absorbed by capillary uptake along any pre-existing crack or interface between the fiber and resin matrix. The effect of moisture on composites is detailed in Figure 2-4. It comprises an increase of weight followed by the plasticization of the matrix and a decrease in the glass transition temperature. A matrix modulus reduced by moisture and crack density in fact amplifies the role of moisture (Jungkuist, 2000). The following two types of moisture-induced degradation can occur in FRP: the first one is called stress-corrosion cracking, which occurs during stress transformation; and the second is found at the fiber-matrix interface, both leading to a decrease in the capacity to transfer stress (Nkuruziza et al., 2005).

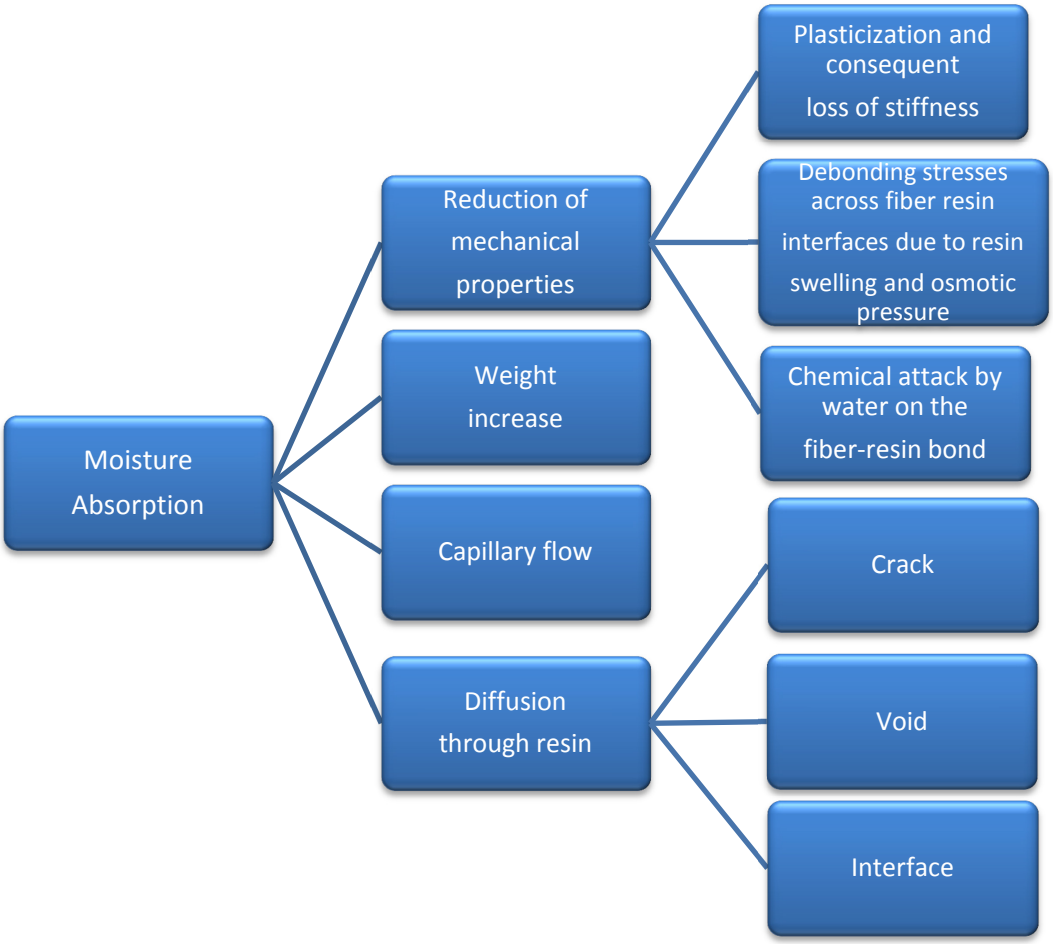

Figure 2-4 Moisture degradation in FRPs (after Nkuruziza et al., 2005)

2.4.3. Effect of Voids in and around FRP

Localized voids and defects can occur during the manufacturing of FRP reinforcements, which can significantly affect their strength, but not their stiffness. Their strength has a direct relationship with localized weak sections, while the stiffness is related to the tangent of the stress-strain curve (Nkuruziza et al., 2005).

The effect of the bar casting position on the bond behaviour of FRP rebars in concrete has been investigated by several researchers. It has been observed that during concrete placement, air, water and fine particles migrate upward through the poured concrete and get trapped under the rebar. This phenomenon decreases the contact surface between the concrete and the rebar and thus causes a significant drop in the bond strength under the horizontal reinforcement placed near the top of the pour. Tests have shown that the bond strength of top-cast bars is about 66% of that of bottom-cast bars (Ehsani, Saadatmanesh, & Tao, 1993). A decrease in the bond strength will increase the required development length of the FRP bars and hence, a modification factor is needed for calculating the required development length for top rebars. A modification factor of 1.1 was proposed for top bars based on pullout tests (Chaallal & Benmokrane, 1993). A modification factor of 1.3 was recommended by the ACI guide (American Concrete Institute, 2003), but more recently changed to 1.5 (American Concrete Institute, 2006).

2.4.4. Other exposure conditions

Two contradictory results have been presented for the effects of freezing-thawing on FRP-RC, which indicates that more research is still required. Chen et al (2007) found that freeze-thaw cycles without the presence of high moisture do not significantly affect the mechanical properties of FRP rods. On the other hand, the study conducted by Subramaniam et al. (2007) show that freeze-thaw cycling produces a significant decrease in the ultimate load transfer capacity and in the interfacial fracture energy. The contradictory findings of the above two studies indicates that further research is needed in this direction. Davalos et al. (2008) found that wetting and drying cycles can lead to more severe degradation than immersion. Chen et al. (2007) found similar results at temperatures of 40°C or less.

2.5. Fatigue Behaviour of FRP

A substantial volume of research on fatigue and lifespan prediction of FRP over the past 30 years is available in the domain of the avionics industry. There are not many studies available on FRP-RC systems. For FRPs and concrete, a report on external FRP reinforcement gives some information (ACI-440-2R, 2008). In this report, tests showed that CFRP is generally the least prone to fatigue of all types of FRP. At 1 million cycles, the fatigue strength decreases to 30-50% of the initial static strength. In 2 million cycles, AFRP (Aramid Fiber Reinforced Polymer) bars for concrete applications lose 27 to 46% of their initial tensile strength. On the other hand, the slope of creep-rupture time versus stress is similar to the slope of the cyclic lifetime versus stress. It is quite useful to know that fibers will fail following a strain-limited creep-rupture process.

Environmental factors play a vital role in fatigue behaviour, especially moisture, alkaline environment and acidic solutions in the concrete surrounding the rebars. Thus, unlike for steel, no clear fatigue limit can be defined. It should be noted that it would be detrimental if the resin/fiber interface degrades under moist and alkaline conditions. It is important to note that the endurance limit is directly dependent on the value of cyclic stress ratio. A higher stress ratio would decrease the endurance limit. In general, FRP fatigue behavior is known to be mainly dominated by the interfacial bond between the fiber and resin matrix.

2.5.1. Effect of Fatigue Loading in Concrete

Due to the high strength of FRP, serviceability becomes a critical issue in terms of crack width control and deflection. Crack growth in FRP-RC beams has not yet been completely understood.

Crack Mouth Opening Displacement (CMOD) is an index for comparing the effect of fatigue on a beam or slab (Zou & Huckelbridge, 2007). The relationship between the number of cycles and CMOD is related to the sum of the elastic and inelastic CMOD growth of crack opening. The amount of elastic CMOD is derived from the maximum and minimum opening of a crack under loading. At a minimum load, inelastic CMOD does not disappear after load removal. This inelastic CMOD will increase as the number of cycles increases and no change occurs for the elastic property. With a much lower modulus elasticity in FRP than steel (almost one-fifth), the crack opening for FRP-RC is much larger (Figure 2-5). In the presence of wider crack interlocking, aggregate bridging and friction within cracks will increase considerably. By increasing the number of cycles, the number of active interlocks is decreased. Cyclic loading would cause degradation in aggregate bridging and crack face friction. As indicated in Figure 2-6, the tensile part at the crack zone is ignored, and the area beyond that stage is included in the following calculations, which show the relationship of the number of cycles with CMOD (Equation 2-2).

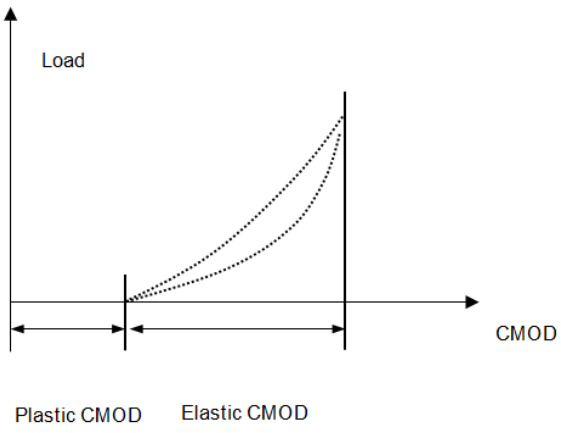

Figure 2-5 Definitions of elastic and plastic CMOD (Zou & Huckelbridge, 2007)

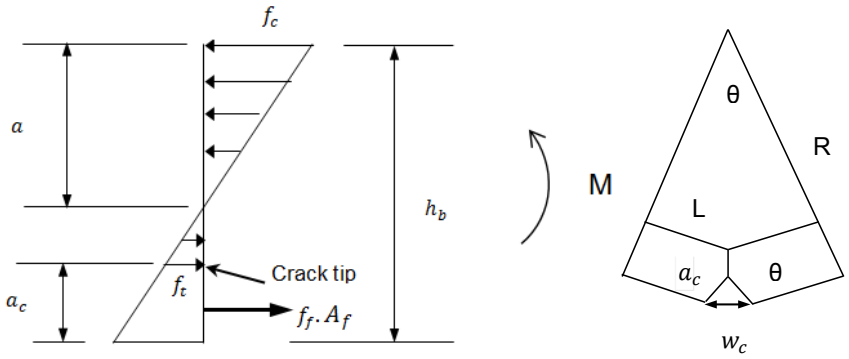

Figure 2-6 Assumed stress distribution at a cracked section, and a hinge model (Zou & Huckelbridge, 2007)

Equation 2-2 $$\frac{dw_c}{dN} = \frac{M}{EI}\frac{(L+w_c)^2}{L}C(\Delta K)^m$$

where

N is the number of cycles;

Δk is the stress intensity factor range at maximum and minimum loading;

C and m are the material parameters;

w_c is the crack width; and

Table 2-4 classifies fatigue based on the number of cycles, dividing fatigue loading into low-cycle, high-cycle and super-high-cycle fatigue categories. For experimental tests, the minimum number of cycles is recommended to be 10^6 (Lee and Barr, 2004).

Table 2-4 Classes of fatigue load (Lee *and* Barr, 2004)

Low-cycle fatigue			High-cycle fatigue				Super-high-cycle fatigue		
1	10^1	10^2	10^3	10^4	10^5	10^6	10^7	10^8	10^9
Structures subjected to earthquakes			Airport pavements and bridges		Highway and railway bridges, highway pavements		Mass rapid transit structure		Sea struc-tures

Repeated cyclic loading can cause internal micro-cracks in materials, which propagate with increasing number of load cycles leading to unpredictable failure. Fatigue phenomena related to metallic structures have been analyzed since the 19th century (Suresh, 1998), whereas research on RC structures under cyclic loading has only been undertaken in recent decades. Degradation under fatigue in concrete is more complicated than in metals due to its heterogeneous nature. The mechanism of the fatigue in reinforced concrete may be attributed to the bond degradation between aggregates and the cement or by the development of existing cracks in the cement paste (Seitl et al., 2009).

Addition of fibers to plain concrete is found to improve its fatigue behaviour as compared to plain concrete (Goel et al., 2012). Ramakrishnan and Lokvik (1992) suggested that Fiber Reinforced Concrete (FRC) reaches an endurance limit at approximately 2×10^6 loading cycles. However, it has been proposed that tests of up to 10×10^6 cycles need to be carried out to confirm this conclusion (Colin & Zemp, (1991). While most researchers believe that FRC has better fatigue behaviour compared to plain concrete, there is some conflicting evidence based on the work of Cachim (1999).

3. Research Methodology

3.1. Overview

This research methodology chapter includes the experimental test set up and the experimental techniques used. The type of concrete, Fiber Reinforced Polymer (FRP) bar specification, beam section size, Fiber Optic Sensor (FOS) and adhesive materials were kept the same for all of the samples. The beams were designed, cast, and after 28 days, subjected to pre-cracking. This pre-cracking was designed to simulate the expected flexure cracks in service and to enhance the effects of subsequent exposure. The beams were then exposed to one of the following four conditions: control (indoor lab environment), immersion in alkaline solution, cyclic immersion in alkali solution (Wet and Dry or W&D condition), and outdoor exposure (local Montreal climate). After 14 months, the beams were tested for their mechanical response in both static and dynamic conditions. Bare FRP bars and concrete cylinders were also exposed to the same conditions to ascertain the effect of environment on the constituent materials.

3.2. Beam Design

The test specimens were beams of 1.75 m in length, designed according to the ISIS Design Manual (ISIS, 2007). (Appendix A provides detailed design calculations). Concrete with compressive strength of 35 MPa and the GFRP bars with ultimate strength as provided in Table

3-1 were used in the design. GFRP reinforcement was used for top and bottom reinforcements, and Table 3-1 shows the details of the material properties as given by the manufacturer. The stirrups were all normal reinforcing steel, 10 mm in diameter, located at 100 mm centers along the entire length of the beam. The top reinforcement consisted of two 10 mm FRP bars and the bottom reinforcement comprised two bars of 19 mm. FRP bars of 6-mm diameter were used as the supplemental bars mounted with FOS strain sensors. Recent research by Torkan (2010) found that the minimum length of the supplemental bar should be twice the development length (Appendix C) of the supplemental bar and bar diameter should be as small as possible as compared to the main rebar so that the strain captured by the FOS in the supplemental is close that of the main rebar at the same location. The main and supplemental bar sizes used in this research comply with those recommendations. The beam and reinforcement can be seen in Figure 3-1.

Table 3-1 GFRP Mechanical specifications (VRod 2011)

Bar size	**Tensile Modulus of elasticity (GPa)** **E**	**Guaranteed Design Tensile Strength** f_{tu}	**Shear Strength (preliminary results)** f_s	**Ultimate Strain in Tension (%)** ε_{tu}	**Poisson's Ratio** γ
#19	47.6	656	200	1.53	0.25
#10	45.4	765	200	1.89	0.21
#6	46.1	784	200	1.90	0.25

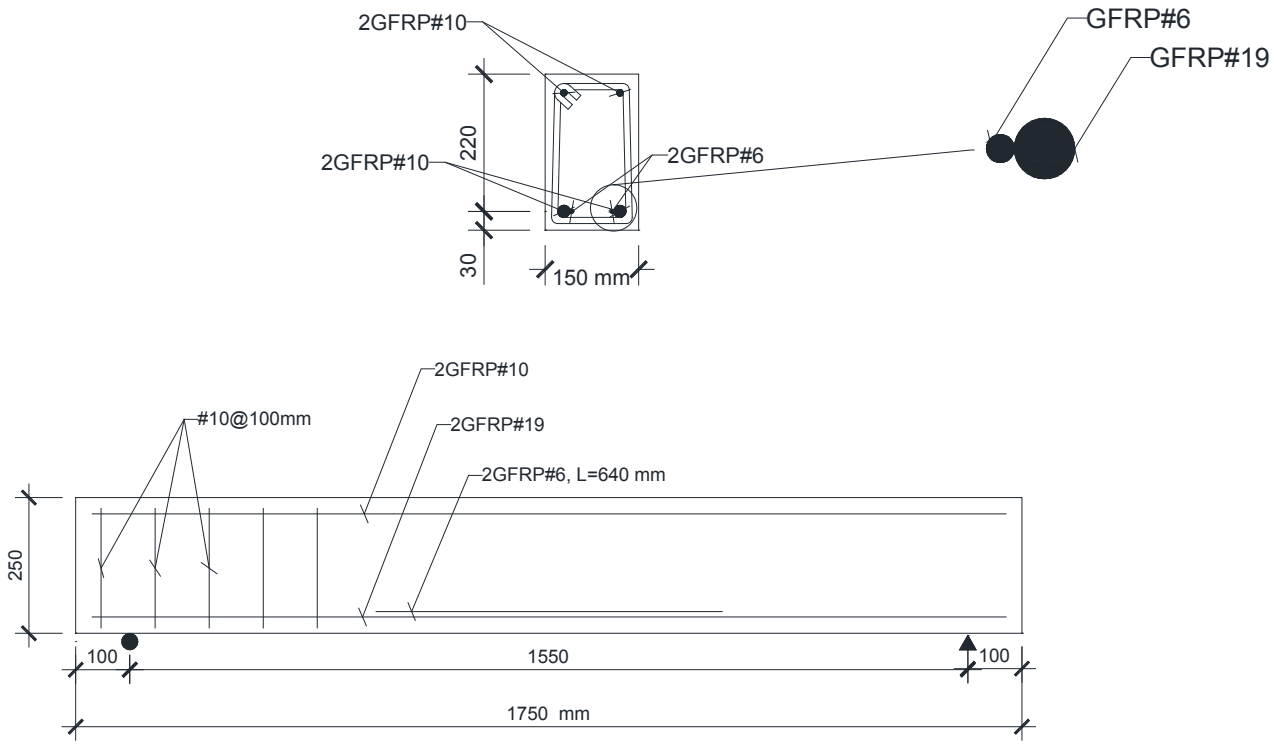

Figure 3-1 Elevation and cross section of FRP-reinforced beams

Torkan (2010) reported a comparison of the performance of Fabry-Perot and Fiber Bragg Grating (FBG) sensors; and the Fabry-Perot sensors were found to work only up to a strain level of 3000μs, while FBG sensors were found to operate at a higher strain level. As FBG sensors are reported to be reliable as reported in the above study and other studies, those types of FOS sensors were used in the current research. More traditional electrical strain gages (ESG) were also used to compare to fiber optic sensors (FOSs) as well as to assess their behaviour in normal conditions. Seven sensors were placed at the level of the bottom reinforcement; two FOSs and five ESGs and one sensor at a bar on the top part of a beam section. Three ESGs were installed along the length of the main bar, and the data from these ESGs should provide the strain profile

along the length of the bar to validate theoretical strain. In the fatigue tests, one ESG was added at the top compression bar as well. Figure 3-2 shows a general scheme of the sensors in a typical specimen. The supplemental bars were connected to the main bar by carbon fiber wrap and plastic “zip” ties, as shown in Figure 3-3. This method was adequate to capture strains in the supplemental bar of at least 80% of the strain in the main bar (Torkan, 2010).

The length of the CFRP wrapping at the ends of the supplemental bar is 100 mm as shown in Figure 3-3. Since the length of CFRP wrapping is small in comparison to the whole length of the main rebar, it is not expected to affect the bond.

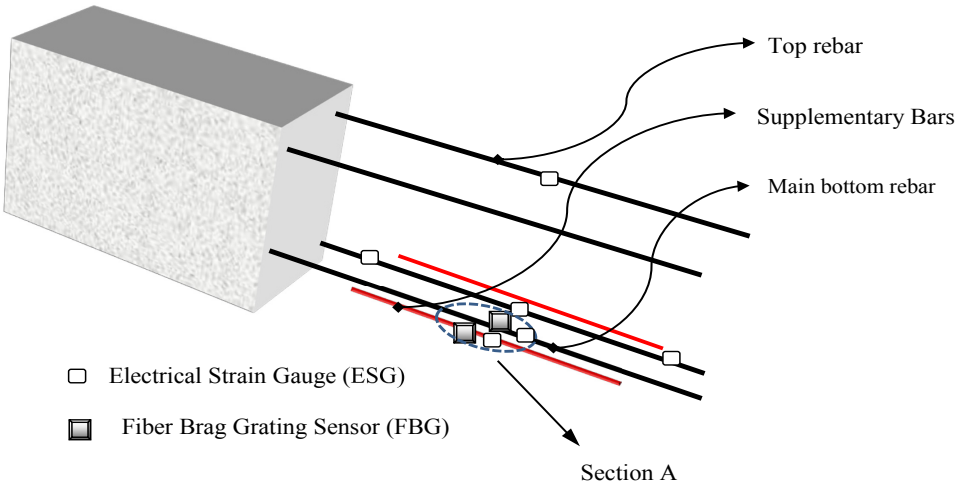

(a)

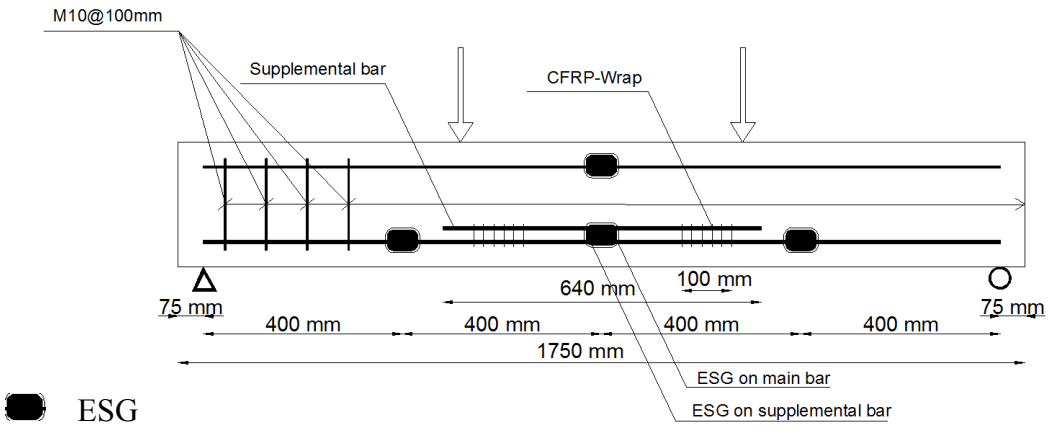

(b)

Figure 3-2 (a) All sensors locations, (b) ESG sensors locations

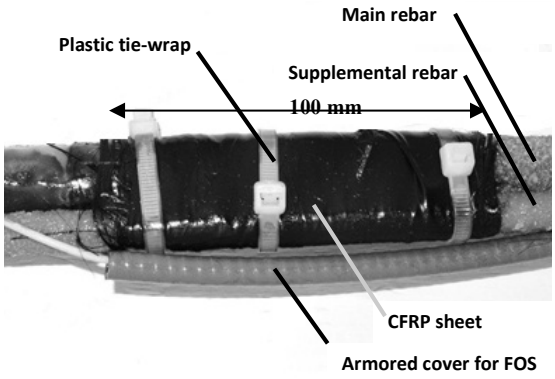

Figure 3-3 Attachment of the supplementary bar (Section A)

3.3. Sensor attachment

Electrical Strain Gauges (ESG) were attached after grinding the surface of the FRP and cleaning it with acetone using a lint-free wipe. In preparing the surface, it is important to have a flat and smooth surface to have a full contact of the sensor with the reinforcement. Two types of sand paper and conditioners helped to achieve the best possible contact: M-Prep Conditioner A was followed by M-Prep Conditioner 5A, and #320 and #600 sand papers. The ESG was connected to the FRP by adhesive type EP-34B. Finally, three layers of coating, AK-22, Araldite and tar, were applied to achieve adequate resistance to the alkaline concrete conditions and to the external solutions (Figure 3-4). The same procedure was followed for the Fiber Bragg Grating FOS, except that the type of adhesive was a specific epoxy recommended by the sensor manufacturer.

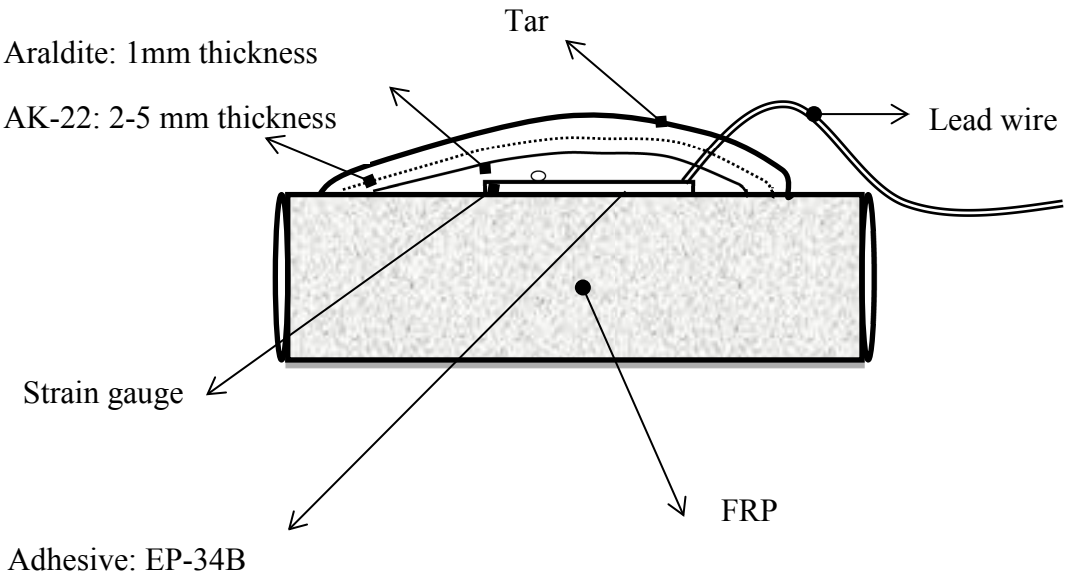

Figure 3-4 Coating details of the ESG

3.4. Concrete casting

The beams were designed with normal density concrete of a type typically used for most civil engineering structures. Concrete with 35MPa was ordered and delivered by Béton Mobile du Québec. A coarse aggregate was selected with 10 mm maximum size and slump designed to be 180 mm. The maximum coarse aggregate size was selected for its workability and use in tandem with congested reinforcement and sensor wires in the bottom part of the formwork. Twelve beams and 15 cylinders were cast according to the ASTM recommendations (ASTM-C31, 2010). The nomenclatures for the testing conditions are given in Table 3-2. There are eight samples for static testing and four specimens for fatigue. There are two specimens for every exposure condition for the static load test, which are identified by the suffix “1” and “2”. All the fatigue samples are identified by suffix “f”.

Table 3-2 Specimen nomenclature

	Control	W&D	Outdoor	Immersion
Static	Control1	W&D1	Outdoor1	Imm1
	Control2	W&D2	Outdoor2	Imm2
Fatigue	Controlf	W&Df	Outdoorf	Immf

External vibration of the beams was accomplished by placing a vibration table under the formwork (Figure 3-5). Beams were covered with wetted burlap and plastic for the first seven days. The formwork was carefully removed so as not the damage the sensors (Figure 3-6). The beams were covered again until 28 days after casting.

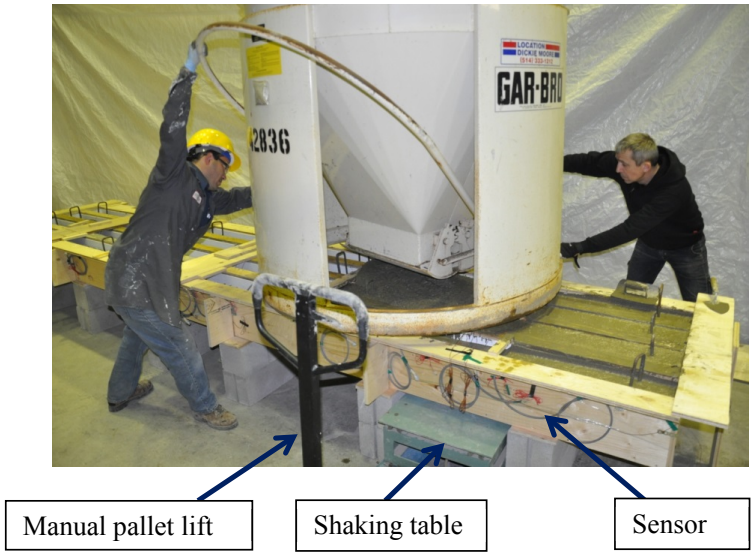

Figure 3-5 Casting concrete and vibration with manual pallet lift

Figure 3-6 Stripping form-work

3.5. Pre-loading

Pre-loading was used to create cracks in the beams exposed to environmental conditions to allow for adequate alkaline solution or water penetration into the concrete, especially, to the level of the FRP. Stewart and Rosowsky (1998) showed that cracking can significantly reduce service life in traditional (i.e. steel reinforced) concrete structures due to chloride-induced corrosion. In this research, corrosion is not an issue but rather alkaline penetration to the FRP and sensors. As detailed in Appendix A, the total magnitude of the vertical point loads corresponding to cracking P_{cr} is 51.3 kN. The load was gradually increased, and some cracks of approximately 1 mm in width appeared at the mid-span, and some micro-cracks were observed near the supports. Figure 3-7 and Figure 3-8 show a typical specimen during pre-loading. Control beams were not pre-cracked.

Figure 3-7 Preloading the beam

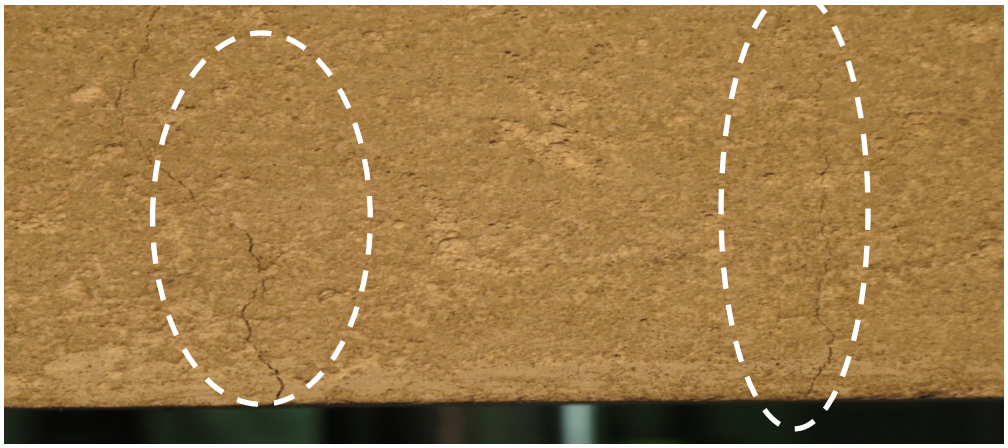

Figure 3-8 *Cracking observed* before environmental exposure

3.6. Exposure Conditions

The beams were exposed to four conditions 28 days after casting the concrete. For each of the four exposure conditions, three beams were cast. The first set of beams (the control) was left in the lab at ambient temperature and humidity. An alkaline solution intended to simulate concrete

pore solution and used earlier by Chen et al. (2007), as given in Table 3-3, was used for two sets of beams. Recently, CSA 806-12 has recommended a specific alkaline solution for FRP research (Canadian Standards Association, 2012). However, this recommendation was published after the start of the present experimental program. The recommended concentrations of sodium and potassium hydroxides are several times lower than that used in this research, but the calcium hydroxide is higher. As the solubility limit of the latter is 1.5g/L, the concentration is not expected to alter the results. The initial pH was measured to be 13.2. However, the pH of the solution increased and after 6 months, it surpassed the limit of the pH meter.

Table 3-3 Composition of the alkaline solution

Chemical Materials	NaOH (g/L)	KOH (g/L)	$Ca(OH)_2$ (g/L)
Chen et al. (2007)	2.4	19.6	2.0
CSA 806-12	0.9	4.2	118.5

Figure 3-9 shows the containers in which beams, cylinders and bare bars were immersed in alkaline solution. These containers were placed in the laboratory and maintained at approximately 21 °C year-round. A polyethylene sheet was placed on top of the containers to avoid excessive water evaporation during the conditioning. Specimens were spaced 200 mm from each other and from the bottom of the container to allow free circulation of the solution between and around the beams and the GFRP bars. Furthermore, the solution level was kept constant throughout the study to avoid a pH increase which could be due to a water level decrease. One set of beams was continuously immersed in this solution. For the purpose of W&D (cyclic immersion), a water pump transferred the alkaline solution to an empty reserved container during the drying phase and back into the container with the samples for the wetting phase. For simulating the wet and dry (cyclic immersion) condition, the following plan was adopted: three days of immersion followed by four days of drying, which provided enough time for the drying of the surface pores in the concrete and enhanced alkaline solution absorption in the subsequent cycles (Figure 3-10). Continuous and cyclic immersions were carried out for a period of 14 months resulting in 120 cycles for the case of cyclic immersion. In addition to the beams, unreinforced concrete cylinders as well as lengths of bare (not embedded) FRP

reinforcement were also placed in the storage tanks. The final set of beams was stored outdoors at the Concordia Loyola Campus yard between February 2011 and May 2012 with no cover and with sufficient gaps in between the beams resting approximately 50 mm above the ground on a wood pallet. Figure 3-11 shows the average monthly maximum and minimum temperatures of this area for this period of time. The amount of precipitation shows that the samples were covered by snow or rain to a considerable extent (Figure 3-12). The samples were tested after at least one week after the weathering conditions were applied and when it was completely dry on the surface at the time of the tests.

Figure 3-9 Alkaline containers

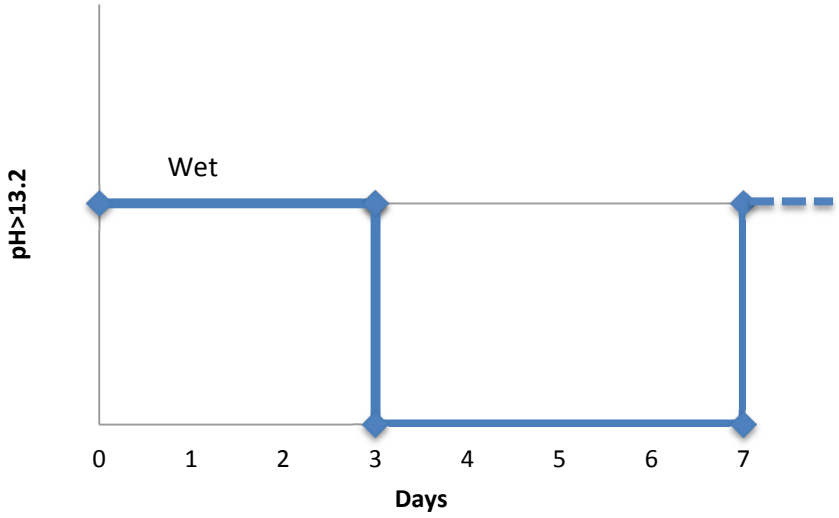

Figure 3-10 Wet-Dry Cycles

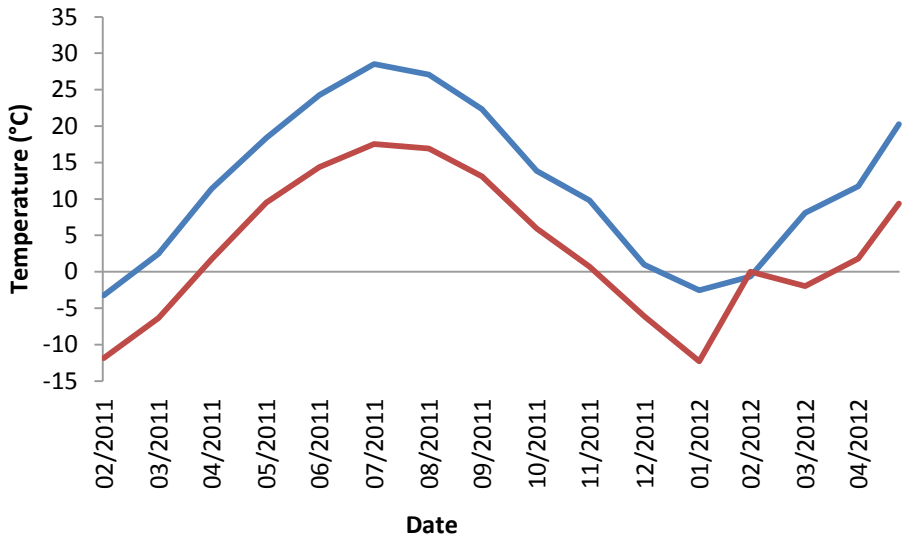

Figure 3-11 Montreal average monthly temperature during exposure period (Weather Canada)

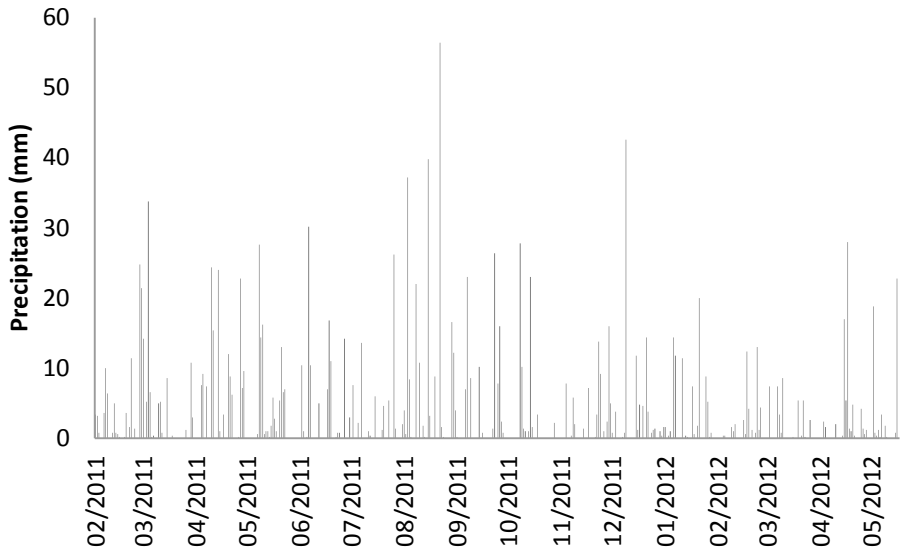

Figure 3-12 Montreal precipitation during exposure period (Weather Canada)

3.7. Mechanical Testing

The following mechanical tests were performed on various specimens:

- Tests on the component materials
- Compressive strength of the concrete cylinders (results in Chapter 4)
- Static flexural test of the FRP reinforced concrete beams (results in Chapter 4)
- Cyclic (fatigue) flexural test of the FRP reinforced concrete beams (results in Chapter 7)
- Post-fatigue static flexural test of the FRP reinforced concrete beams (results in Chapter 7)

3.7.1. Tests on Component Materials – Concrete Cylinders

All of the cylinders were kept in a water tank for 28 days and then moved to the various exposure conditions. Compressive strength was tested for three specimens according to ASTM C39 (ASTM-C39, 2010) just prior to beam testing. These results were used for numerical modeling and strain analysis.

3.7.2. Tests for Flexure FRP-RC Beam under Static Load

Figure 3-14 shows the four-point (also referred to as third-point) loading protocol used for testing the beams in flexure. The rollers were inserted at two ends of the spreader beam to ensure concentrated loads. The beam samples were instrumented to measure the vertical deflections at the mid-point of each sample by means of two sets of potentiometers (Figure 3-14). Each beam was loaded at a rate of 500N/s until fracture. Strain was measured from the FOS and ESG sensors at one Hz using a Strain-smart 5000 data acquisition system. The white painted surface of concrete was carefully (visually) inspected for any cracks developing on the concrete surface during loading. The interrogator system was Micron Optics sm130, with its 130 core equipped with on-board averaging capabilities. For recording data in every FOS connected to a channel, data averaging on the entire module can be done, and thus a control over the recorded data per second can be implemented. This control reduces the volume of data transmitted by the interrogator. The maximum data rate is 1000 Hz, which has the following relationship with the acquired data (Micron Optics, 2012).

Equation 3-1 f (frequency) = Collected data (Hz) × Interleave =1000 (Hz)

In order to get one average data per second of the collected data in the present test, the value of 1000 of interleave is used here. For each beam, two strain values, one from the main and one from the supplemental bar, were captured.

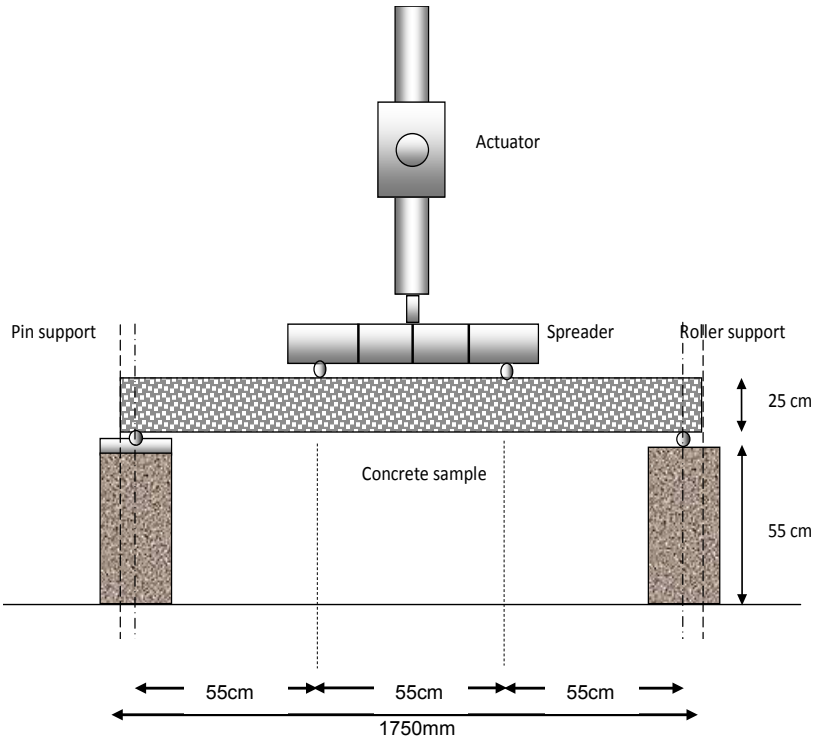

Figure 3-13 Test set up

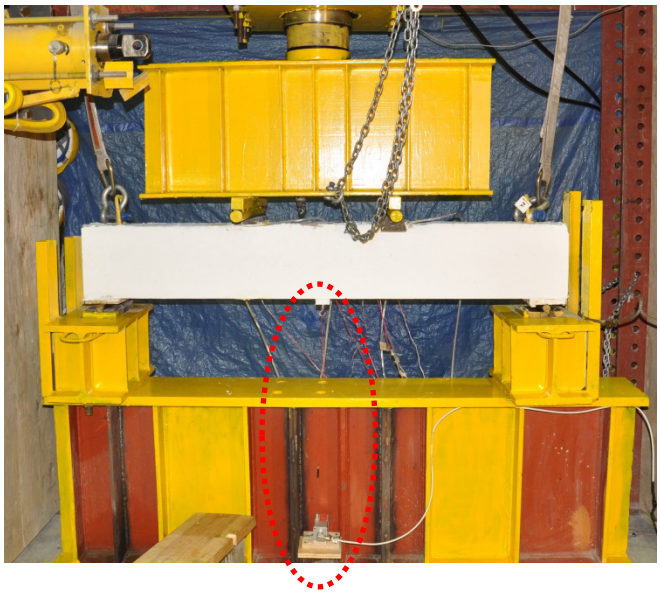

Figure 3-14 Location of the potentiometers

3.7.3. Cyclic load Tests in Flexure

Fatigue loading is created by cyclic loading at a beam's mid-span (Figure 3-15). For every specimen a constant amplitude load of F_{Ave} was applied (Figure 3-16), so that $F_{Ave}= (F_{max}+F_{min})/2$ where F_{max} is 80-90% of the maximum fracture loading and F_{min} is the superimposed load which is 70-80% of the maximum fracture loading(for all conditions except Controlf). Fatigue loading test started with 1 Hz and then increased to 2 Hz to speed test duration as no change in the strain, deflection and crack pattern were observed in the pilot test using the control specimen (labelled as "Controlf") after 400,000 cycles (Figure 3-17). As a result, the rest of specimens were tested with the cyclic load with frequency of 2 Hz. The stress in FRP bars had tension-tension sinusoidal variation. In Figure 3-16, σ_{min} represents the effect of the superimposed loads on a bridge (pavement, installation etc.), and σ_{max} is about 80-90% of the ultimate nominal

capacity. The upper and lower fibers of the beam will be under compression during the cyclic loading and do not reach to zero loading during cycling (compression-compression). There was uncertainty in application of the load close to the maximum capacity of the actuator and for the pilot test (i.e., the test with the control specimen, Controlf) some load cycles were applied with a mean value of 60% and the peak value of 65% of the ultimate capacity; and later increased to the mean value of 75% and peak value of 80% of the ultimate capacity without noticeable change in the response of the beam. For the Immf specimen the mean value of the load was creased further to 85% of the ultimate capacity to accelerate the damage in the beam. But not noticeable change was observed when a slightly lower level of load was applied in the earlier cycles as shown in Figure 3-17. Based on the experience with the above two specimens, $\sigma_{ave}$for the remaining specimens (i.e., W&Df and Outdoorf) was modified to 85% of ultimate capacity (Figure 3-17). The loading band $\Delta\sigma$ was kept at 10% of the ultimate capacity in all the above cases.

The data from the actuator (deflection, load, cycle number, time) is recorded at 10 Hz for its high sensitivity and the strain from the data acquisition system (Strain Smart 5000) is acquired at 1 Hz. In addition, after every 50,000 or 100,000 cycles *t*he response quantities (strain, deflection and crack width) for one complete loading-unloading cycle was recorded in order to check the crack width and the change in deflection.

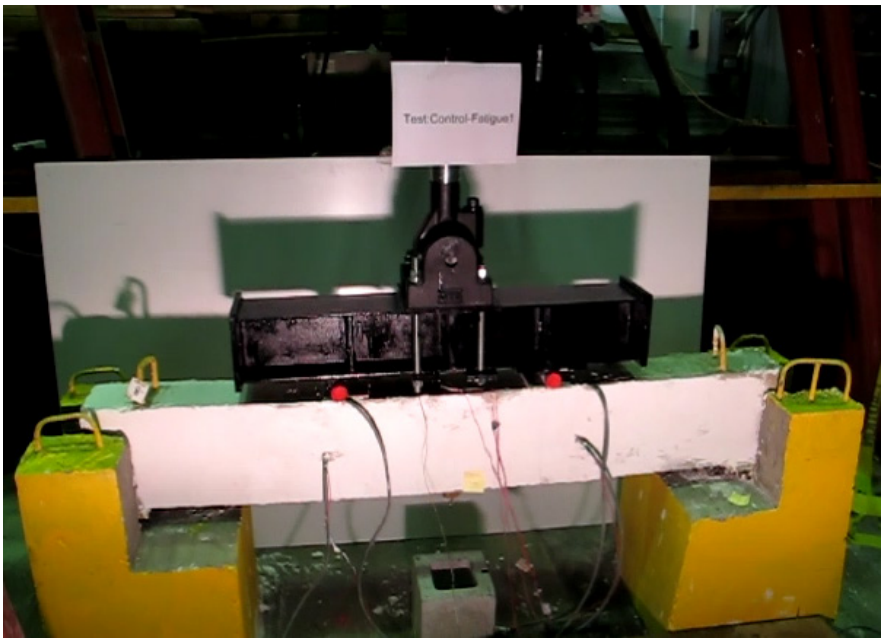

Figure 3-15 Fatigue loading by an actuator

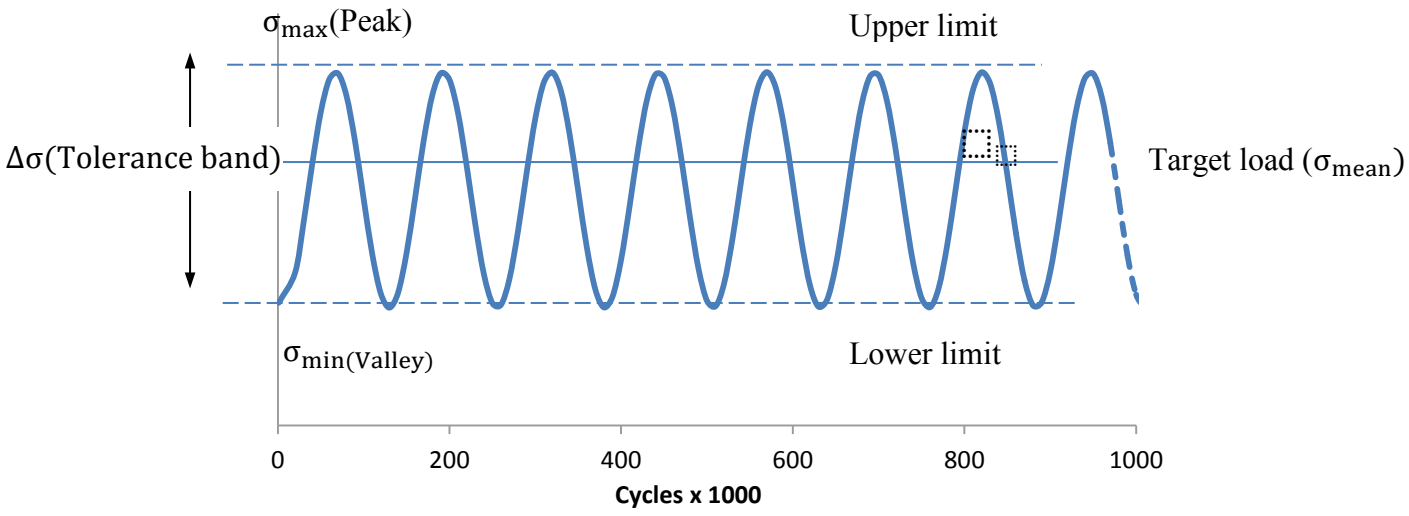

Figure 3-16 Cyclic loading function used for the fatigue tests

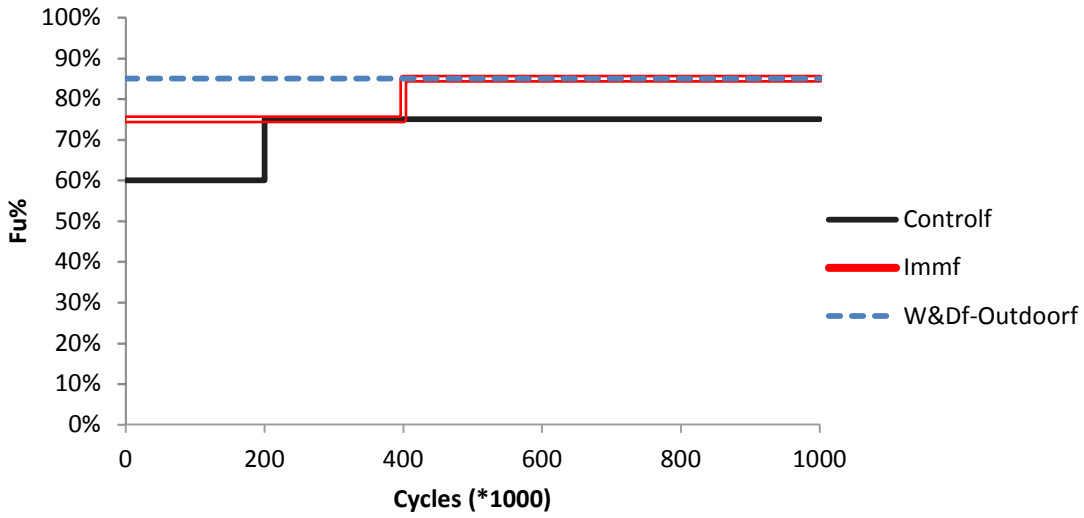

Figure 3-17 Load cycle protocol (Target average load)

3.8. SEM Experimental Procedure

A Hitachi S-3400N Scanning Electron Microscope (SEM) equipped with WDX (Wavelength Dispersive X-ray Spectroscopy) and EDX (Energy Dispersive X-ray Spectroscopy) systems was used for visual observations and for elemental analysis. For the purposes of this study, the Backscattered Electron (BSE) detector and composite mode were utilized to conduct the scanning for compositional analysis and the Secondary Electron (SE) mode used for visual analysis. The Variable Pressure (VP) mode, which allows for the observation of wet, oily or dirty samples as well as of non-conductive materials without the need for sample preparation (such as coating), was applied for this study. A palladium-gold coating was found necessary for good visual images, but not necessary for compositional analysis. A Quorum Q150 sample preparation system was used for sputter coating. An applied pressure of 40 Pa, accelerating voltage of 15 kV,

and probe current of 60 nA were used throughout. For the analysis, the non-normalized option was selected so the results could be given as the weight percentage of a specific material in that spectrum. Since the continuous and cyclic immersed samples were exposed to solutions containing sodium and potassium hydroxides, elemental analysis was focused on the concentration of sodium (Na) and potassium (K). Calcium concentrations did not give reasonable results as other materials (cement, aggregate) also contain calcium, and so it was ignored in study. Several methods were investigated to determine alkali concentration. It was found that point measurement led to high variability depending on the material of the point selected. Spectrums of varying sizes were then investigated; it was found that an area of 0.2 mm^2 gave an adequate area to average measurements while maintaining good spatial resolution.

To obtain samples of FRP embedded in the concrete, the tensile face at mid-span of the specimen which does not contain any sensor (Figure 3-2(b)) was dry cut by a diamond circular saw, and a cubic piece of concrete block with embedded FRP was removed (Figure 3-18). A smaller slice of this cubic piece was then cut easily by clamping the cubic block to a vise. For the bare rebar, a slice was removed sufficiently far from the ends to ensure only radial flow of solution. Bars of two sizes, 6 mm and 19 mm, were embedded into epoxy prior to final preparation and results with the larger diameter studied (Figure 3-19). For both types of specimens, the surfaces of the concrete and of the FRPs were polished by up to one micron dry sandpaper. Care was taken not to expose the samples to water during the cutting and polishing steps to minimize the effects on the absorbed alkalis.

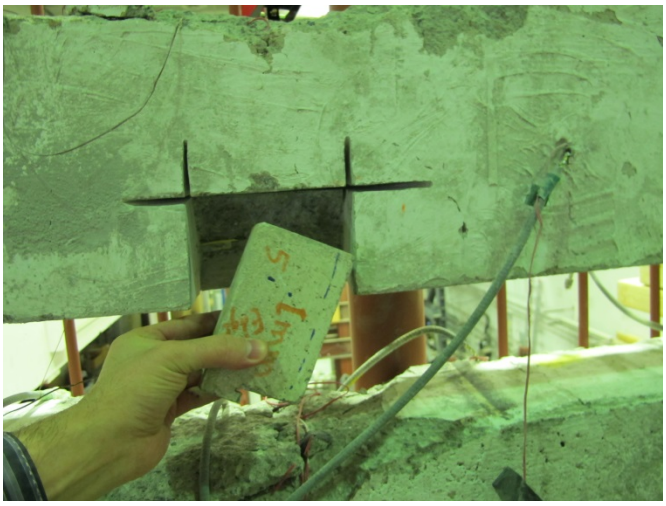

Figure 3-18 Cubic piece extracted by circular saw (embedded bar)

Figure 3-19 Bare bars embedded in epoxy (Φ6 and Φ19)

4. Static Test

4.1. Introduction

The results of the experimental tests conducted on the beam specimens under static loading and the performance of various sensors installed in the beam are presented in this chapter. The performance of the FOS in the main and the supplemental bar is studied and discussed. The performance of the five ESG sensors: three locations including quarter spans and the mid-span on the main tensile rebar, one on the supplemental bar (Figure 3-2 shows the details) are also presented here. Results of strains in the top rebar are discussed in 6.9. A potentiometer at the mid-span was used in the tests to measure the deflection, and another one was used for measuring the crack width (Figure 4-1); these results are presented as well.

Compressive strength of concrete cylinders corresponding to each condition was measured just prior to static flexural testing. The results from three samples tested in each case were averaged. The mean values of the compressive tests for the concrete cylinders in different conditions are presented in Table 4-1, where each entry in the table has been labelled with the abbreviation of the corresponding condition and a numerical index of 1 or 2. These test results are used to present the data in a non-dimensional form in a later section. Cylinders were not stored in the

Outdoor condition; it is assumed that the compressive strength is the same as the Control condition for analysis.

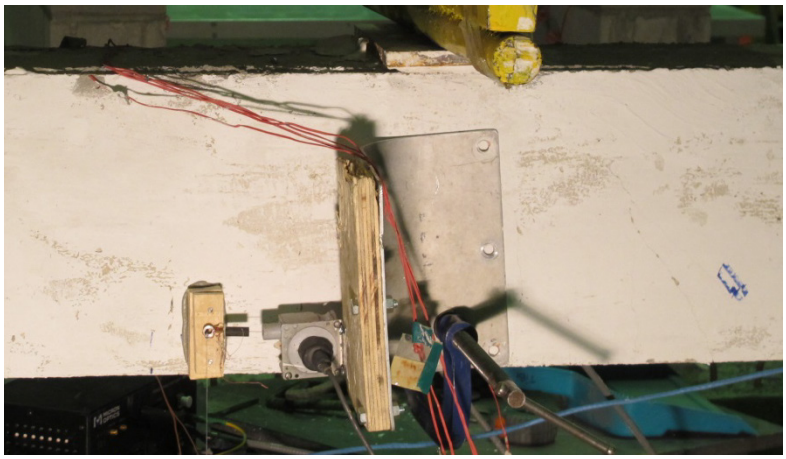

Figure 4-1 Crack measurement by potentiometer

Table 4-1 Compressive strength of cylinders at time of beam testing

	Control/Outdoor	**W&D**		**Imm**	
	Control1 Control2	W&D1	W&D2	Imm1	Imm2
f_c' **(MPa)**	46.2	49.4	55.6	47.2	55.5

4.2. Deflection Response of the Beams

Figure 4-2 shows the variation of the mid-span deflection with applied load (F-Δ graph) for the eight specimens. The deflection data for Control2 could not be recorded after 80% of the ultimate expected load due to a technical problem with the instrumentation system. Figure 4-2 shows that the trends for deflection and the modulus of elasticity are similar in all of the specimens. More details will be given in subsequent paragraphs. One of the specimens in Outdoor conditions (Outdoor2) had shear failure following by ultimate load (Table 4-4), possibly due to deflection incompatibility between the GFRP rebars and the steel stirrups used in the construction of the beams. For the case of Imm1, there was a tensile fracture of the FRP reinforcement along with concrete crushing (Section 4.4 can be referred for discussion of failure modes). This fracture could have resulted from the penetration of alkaline solution to the FRP matrix and its subsequent weakening under such exposure. It was the only case of the fracture of the reinforcing bars amongst all of the different specimens with different conditioning regimes.

The post-peak part of the load-deflection curves as shown in Figure 4-2 of all of the samples with compressive failure were observed to be very similar, in which cases crushing of the concrete was observed. This post-peak curve was not observed in the shear fracture Imm1 and Outdoo2 for their balanced failure (Table 4-4)

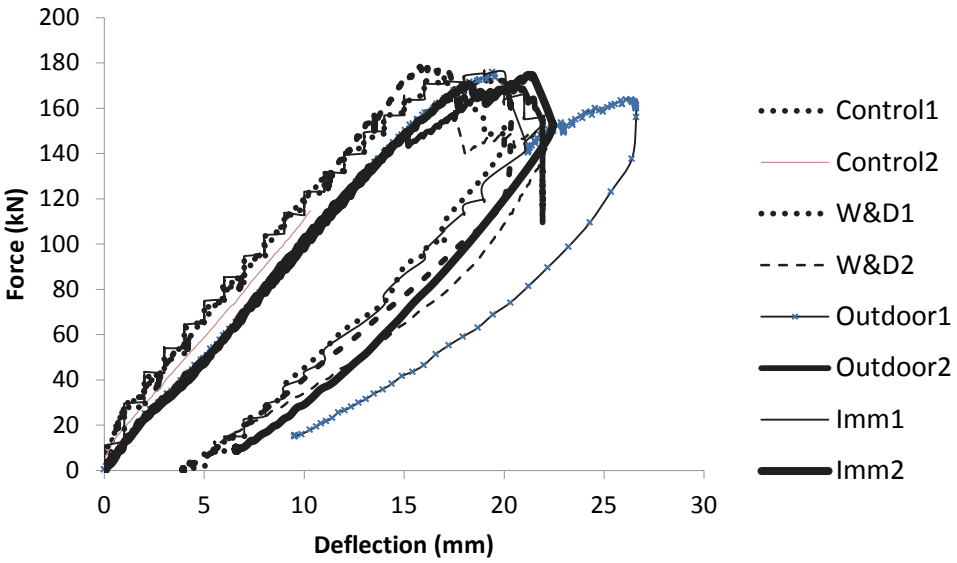

Figure 4-2 Force-deflection (all specimens)

The force-deflection curve from the Outdoor condition (Figure 4-3) shows that the ultimate failure load is very close to that for the Control condition; however more deformability is observed in Outdoor1 specimen. The Outdoor2 specimen does not follow the same post–failure deformation pattern as Outdoor1 which has crushing of concrete in compression followed by shear failure near the support. While both the specimens are identical, there are possibility of variation in the material properties, placement of reinforcements, position of supports and loading which might have played some role in the above differences in their respective behavior and failure modes. The maximum mid-span deflection recorded in the case of the Outdoor specimen (Outdoor1) was 26 mm, and the ultimate failure load was close to 180 kN and the failure load of both the control specimens were close to each other.

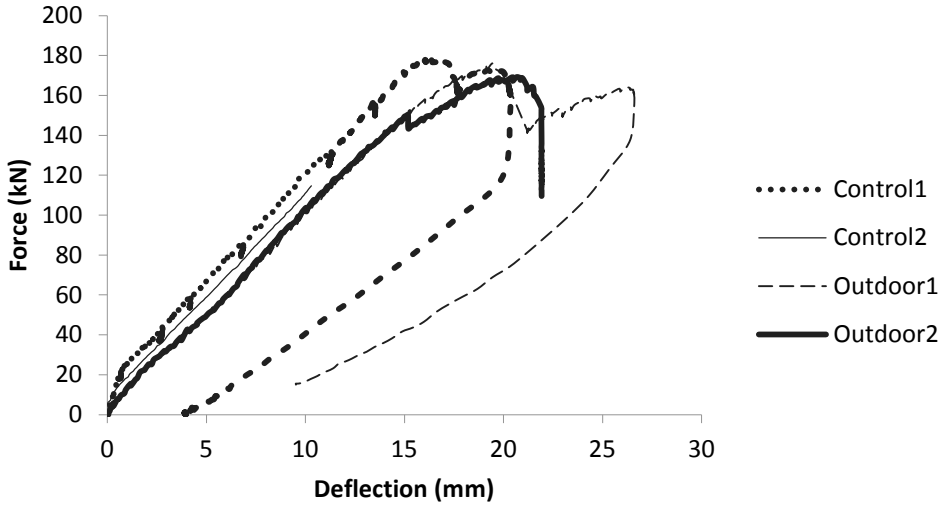

Figure 4-3 Force-deflection in Outdoor conditions

Figure 4-4 shows the load-deflection behaviour of the specimens in W&D conditions, where the failure modes both the specimens (W&D1 and W&D2) were similar to what was observed for the Control condition.

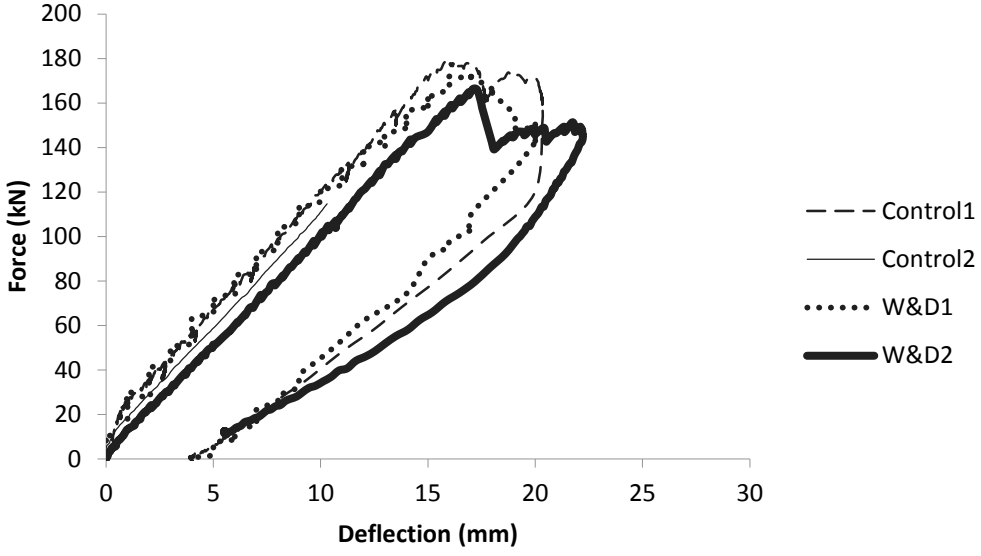

Figure 4-4 Force-deflection in W&D conditions

It can be observed from Figure 4-5 that the load-deflection behaviour of the specimens in Imm1 is similar to that for the Control specimens. However, the tensile-fracture following to the balanced failure is observed. In this case FRP bars elongated significantly for its low modulus of elasticity up to fracture.

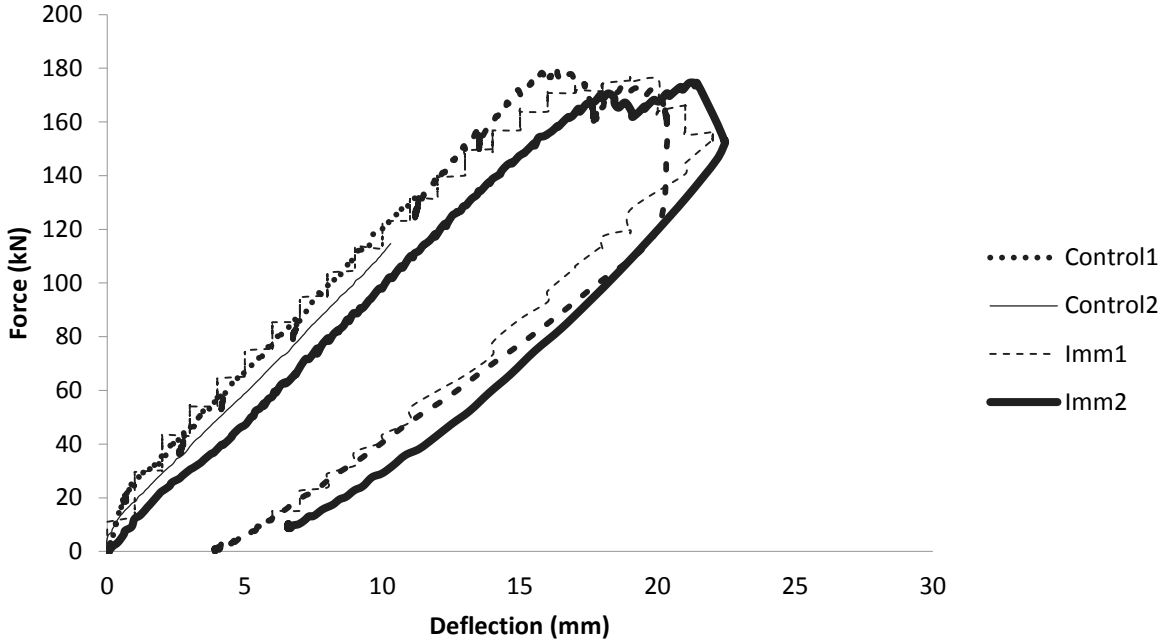

Figure 4-5 Force-deflection in Immersion condition

4.3. Static Load Capacity

From the results of the compressive tests on concrete cylinders corresponding to the beam specimens (Table 4-1), it is observed that the compressive strength of concrete varies based on the type of conditioning and length of conditioning. Therefore, for comparison of the force-deformation curve for all different beam specimens, a non-dimensional value of force, $P/f'_c.a.b$

has been used. Here, f_c' is the measured compressive strength of the cylinder at the time of beam testing (Table 4-1), "a" is the width and "b" is the depth of the cross section. It is observed in Figure 4-6 shows the load-deflection curves for all the specimens and it can be seen from the figure that the Control specimen has the highest flexural resistance and the minimum deflection. The Outdoor1 specimen shows more deformability as compared to the Control specimen, while the failure load is very close to that of the Control specimen. The W&D and Imm specimens also show higher deformability, but lower modulus of elasticity with a drop in the flexural resistance caused by the exposure to alkaline conditions. In Figure 4-6(b) all the specimens are used for comparison with each other, and the load is non-dimensionalized to normalize the effect of the difference in the concrete strength.

Table 4-2 shows the flexural strength ratio (λ) of different specimens as obtained from the static tests, where M_{exp} represents the flexural capacity of the beams obtained from the tests, and M_n and M_r represent the nominal and factored flexural capacities of the beams obtained from the sectional analysis procedure as given in ISIS (2007). It is observed from the table that the experimental capacities of these beams range from 80% to 95% of the nominal capacity, while they are almost double the factored capacities. The following specimens are found to have the lowest range of flexural strength as compared to the nominal capacity: W&D1 (80%), Imm1 (84%) and Outdoor2 (89%). The ratios of M_{exp}/M_r show that the design in any condition is still very conservative. It should be noted that the area of supplemental bar has been considered in calculation of the moment of resistance, M_r; however, its contribution is found to be within 3% of the moment of resistance.

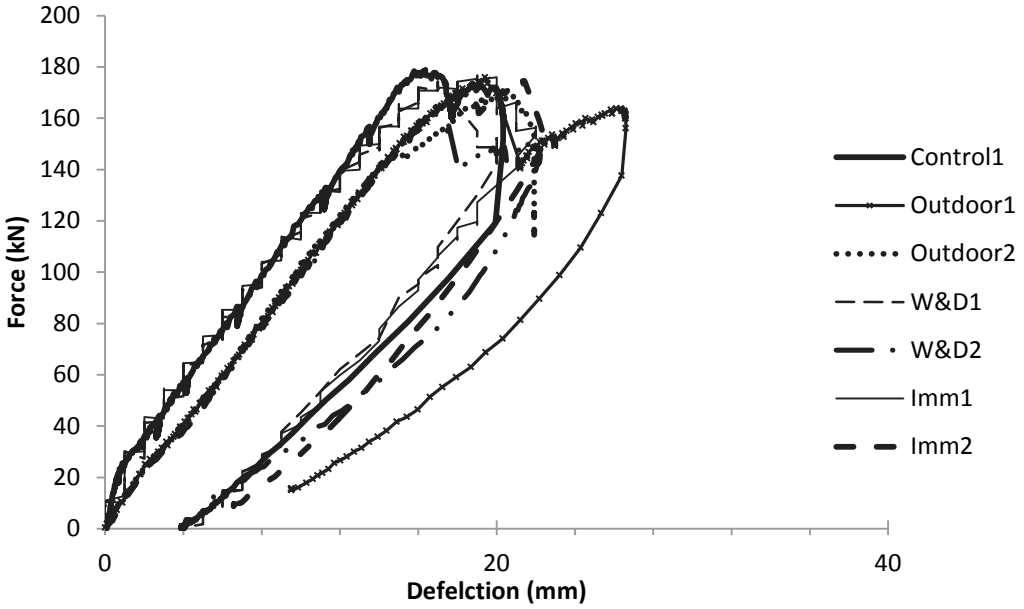

(a)

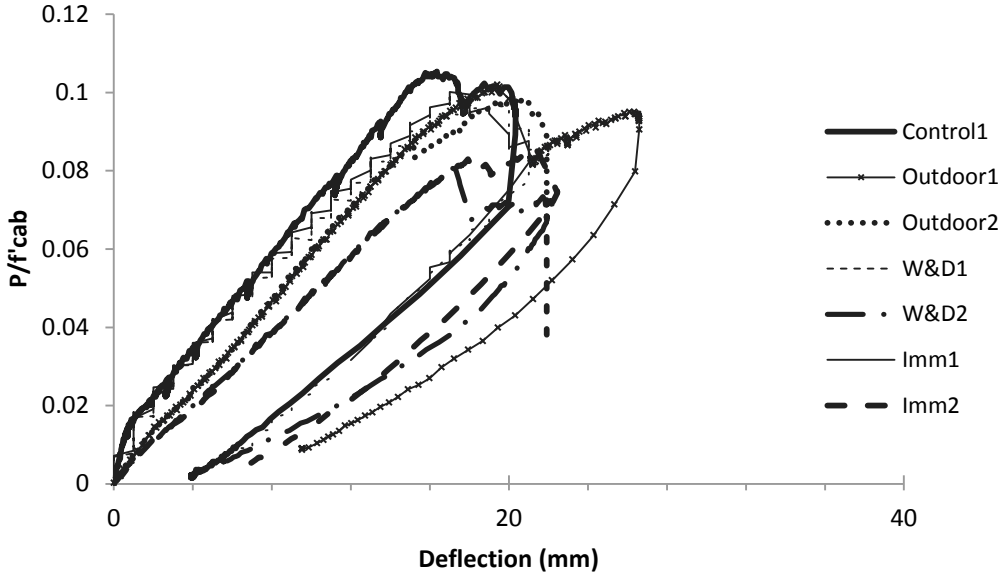

(b)

Figure 4-6 Load-deflection curves for all the specimens in static tests: (a) Load vs. deflection; (b) non-dimensional load vs. deflection

The maximum values of FRP strain recorded by FOS-M (sensor mounted on main FRP rebar), load and deflection from the static tests are shown in Table 4-3. Chen et al. (2007) performed accelerated aging tests for evaluation of durability performance of FRP-RC by making small pull-out specimens. FRP bars were embedded within 100 mm diameter by 200 mm long normal concrete cylinders, at the mid length of the bars. This study is far more realistic in its concrete cover depth. In the cases of W&D and Imm conditions, the strain was found to increase by up to 23% of that corresponding to the Control specimens (Table 4-3), which is mainly due to degradation in the beams in these adverse conditions. In Table 4-3, the calculated theoretical strain from Appendix B has been shown as a percentage of $\varepsilon_{u,frp}$ from Table 3-1. The Outdoor and Control specimens showed the maximum ratio of $\varepsilon_{exp}/\ \varepsilon_{Theo}$ which implies that the bonding between FRP bars and concrete is good. All the recorded strains are greater than the theoretical values derived from Appendix B by considering the different concrete strengths. The capacity of the specimens and the strain in the rebar in different conditions were normalized to those for the control, specimen (Control1) which was taken as the baseline.

Comparing the experimental and nominal flexural strength in Table 4-3, the results were observed to be consistent with the results of the study reported by Chen et al. (2007) for a simulated pore solution (pH 12.7) at RT and W&D conditions after 120 days, with Imm and W&D as given in Table 2-1 and Table 2-2.

Table 4-2 Actual flexural strength from static tests, as a percentage of the nominal strength (λ)

Condition	$\lambda = M_{exp}/M_{Nominal}$	M_{exp}/M_r
Control1	95%	217%
W&D1	80%	200%
W&D2	87%	204%
Outdoor1	92%	212%
Outdoor2	89%	200%
Imm1	84%	208%
Imm2	92%	212%

Table 4-3 Static load capacity (experimental) of the beam specimens

	Beam ID	f'_c(MPa)	ε_{exp} (FRP)	ε_{Theo}	$\varepsilon_{exp}/\varepsilon_{Theo}$	Average ($\varepsilon_{exp}/\varepsilon_{Theo}$)	Normalized
Control	Control1	46	0.01 $0.65\varepsilon_{u,frp}$	0.0084	119%	119%	1.00
Immersion	Imm1	47	0.0085 $0.55\ \varepsilon_{u,frp}$	0.01	85%	96%	0.79
	Imm2	55	0.01 $0.65\varepsilon_{u,frp}$	0.0093	107%		
W&D	W&D1	49	0.0082 $0.53\ \varepsilon_{u,frp}$	0.008	94%	94%	0.77
	W&D2	55	0.0087 $0.57\ \varepsilon_{u,frp}$	0.0093	93%		
Outdoor	Outdoor1	46	0.0111 $0.72\ \varepsilon_{u,frp}$	0.0084	132%	123%	1.04
	Outdoor2	46	0.0097 $0.63\ \varepsilon_{u,frp}$	0.0084	115%		

Benmokrane et al. (1996) suggested formulae for estimating the effective moment of inertia of a beam section as given by Equations 4-2 (Appendix B details these formula variables). As seen in Figure 4-7, proposed formulas give close estimates of deflection up to the cracking moment and overestimates deflection at higher load level because of potential arching action. The CSA-S806

(2012) provides a factor to account for arching action (1<Ka<2.5) while calculating the shear resistance of concrete beams. Further studies on such a coefficient are needed to consider this effect.

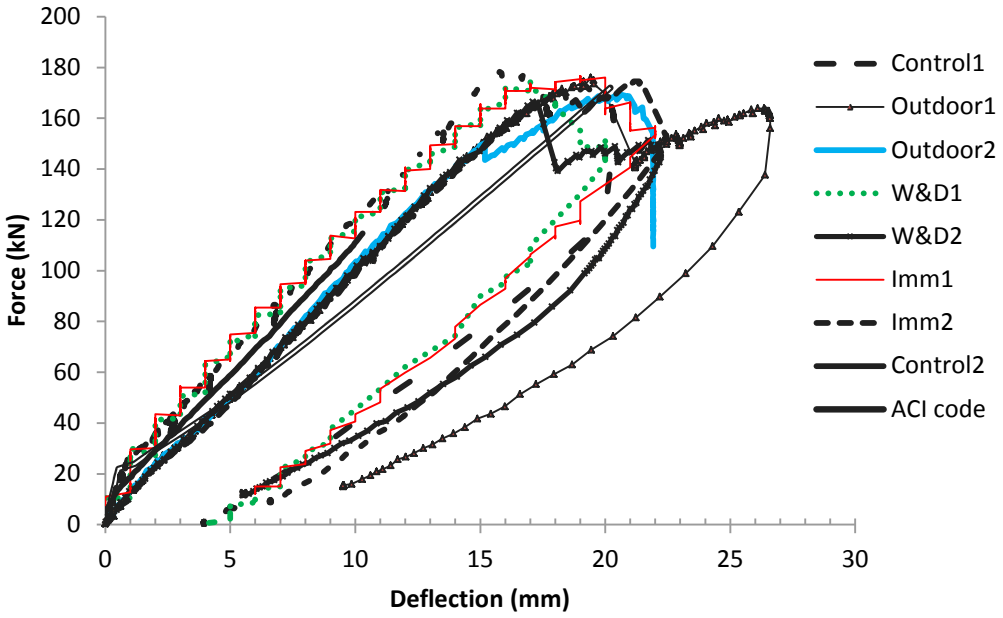

Figure 4-7 Comparing load-deflection to published Theoretical formula

Equation 4-1 $$I_e = \left(\frac{M_{cr}}{M_a}\right)^3 \beta_b I_g + \left[1 - \left(\frac{M_{cr}}{M_a}\right)^3\right] I_{cr} \leq Ig$$ Benmokrane et al. (1996)

4.4. Failure Modes

The failure modes for all the four different conditions are detailed in Table 4-4. The failure mode in all samples is compression in concrete and in some cases followed by FRP shear or tensile fracture. These failure modes are described in the following subsection. The FRP failure occurred by insufficient FRP resistance. The fracture in Imm1 can be correlated to the effect of alkaline environment as explained in Chapter 5 and shear fractured in Outdoor2 can be referred to deflection incompatibility in GFRP and steel stirrup.

Table 4-4 Failure modes in all specimen types

Specimen	**Failure Mode**
Control1	Compression
W&D1	Compression
W&D2	Compression
Outdoor1	Compression
Outdoor 2	Balanced - Compression followed by shear failure
Imm1	Balanced - Compression followed by FRP Tensile fracture
Imm2	Compression

From Table 4-4, it is observed that in the cases of Outdoor and Immersion conditions, the identical specimens corresponding to each condition exhibited different modes of failure. In the case of the Outdoor condition, Outdoor1 specimen failed by crushing of concrete in compression, while Outdoor 2 had balanced failure with crushing of concrete in compression followed by shear failure near the support. On the other hand, in Immersion condition, Imm1 specimen had balanced failure with crushing of concrete in compression followed by fracture of tensile FRP reinforcement, and Imm2 specimen failed in crushing of concrete in compression. As discussed earlier, although the specimens are identical, there are possible of variations in the material properties, placement of reinforcements, position of supports and loading which might have played some role in the above differences in their respective behavior and failure modes.

4.4.1. Compression Failure or Crushing of Concrete

In Figure 4-8 the compression mode of failure is observed by crushing of the concrete at the top middle part of the beam without any tensile fracture in the bottom rebars. The experiment was stopped when the crushing of concrete followed by excessive deflection was observed and the beam failed to take any additional load.

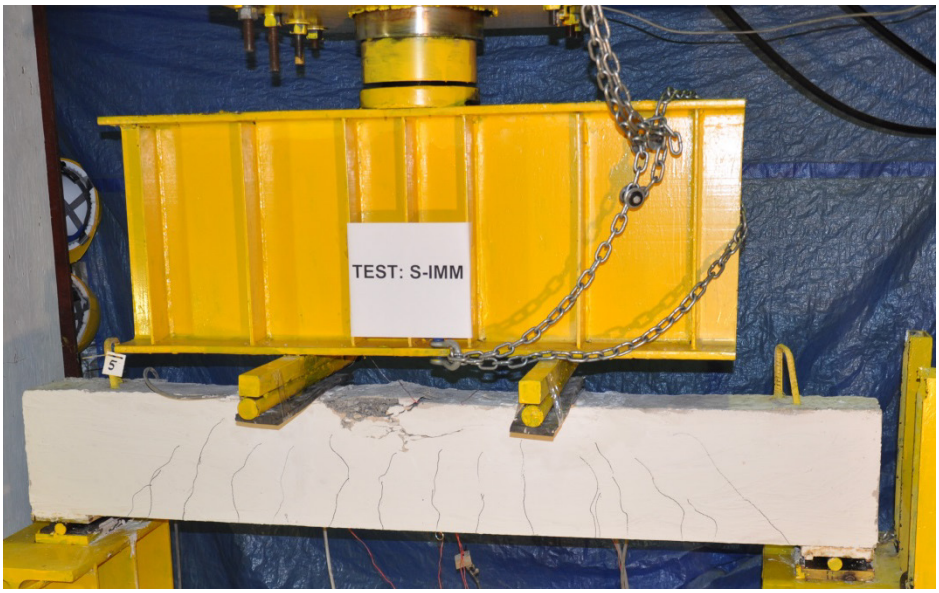

Figure 4-8 Compression failure

4.4.2. Balanced Failure

4.4.2.1. *Crushing of concrete followed by tensile fracture in FRP*

Simultaneous rupture of FRP and crushing of concrete was observed in Imm1. Tensile fracture of FRP caused a sudden failure. While tensile fracture mode is not of interest in the design, this mode of failure is mainly due to degradation of the FRP bars due to alkaline penetration which is discussed more in Chapter 5. Location of the fracture is at the mid-span (flexural area) (Figure 4-9).

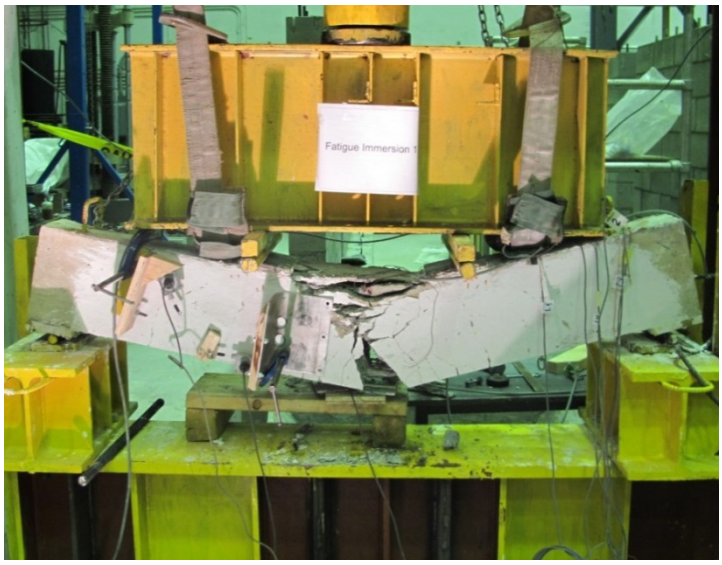

Figure 4-9 Post-failure loading and tensile fracture in Imm1 specimen

4.4.2.2. *Crushing of concrete followed by shear-compression failure*

Crushing in concrete followed by shear failure is shown in Figure 4-10. Fine cracks propagated at the mid-span up to the neutral axis, then the growth and widening of cracks stops while the bond stress near the support starts to increase and steep inclined cracks develop, which quickly propagate towards the neutral axis. The compressive concrete block resists the redistributed load at the inclined crack up to the crushing point, which consequently leads to the sudden fracture of the FRP bars. A similar failure pattern was observed by Aiello and Ombres (2000) and Tang et al. (2006) in their studies of GFRP reinforced concrete beams under flexural load. The penetration of a flexural crack into the compressive block of concrete reduces the engagement of concrete in shear. The cracks in the shear zone can cause detachment of the stirrups from concrete and reduce the effect of aggregate interlocking, resulting in low modules of elasticity and wide cracks in turn leading to shear fracture.

Figure 4-10 Typical shear-fracture in post failure loading of GFRP RC- beam in Outdoor

4.5. FOS Strain Response of the Reinforcement at the Mid-span

The strain data obtained using the FOS installed on the FRP rebars and supplemental bars in the beam specimens subjected to different environmental conditions were compared to the corresponding strain data in the beams in the Control condition. Table 4-5 provides a summary of the observations regarding the performance of the FOS sensors at the mid-span locations. (FOS-M is on the main bar, while FOS-S is on the supplemental bar).

Table 4-5 Functionality of FOS sensors in static testing

Condition	Control1	Control2	W&D1	W&D2	Outdoor1	Outdoor2	Imm1	Imm2
FOS-M	✓	✓	✓	✓	✓	✓	×**	×**
FOS-S	✓	✓	✓	✓*	✓**	✓	×**	×**

×** Internal defect; ✓* Faulty installation (No data recorded); ✓** Connector defect in Shipment

Figure 4-12 to Figure 4-16 show the load-strain behaviour of the FRP bars in tension, where the strain recorded from the experimental test is compared to the theoretical values of the strain as obtained from the sectional analysis. Figure 4-11 compares the ratio of captured strain from main and supplemental bar in different conditions and shows good performance of the sensors except in the immersion condition. In the following figures, FOS-M and FOS-S indicate the FOS installed on the main and supplemental bars, respectively. The experimental strain in all conditions follows the same trend as of the theoretical strain. For calculating the theoretical strain in specimens under different conditions, the relevant mechanical properties of the materials such as the modulus of elasticity and concrete compression strength are applied . The formula in the Appendix A has been used for the calculation of the moment of inertia in these cases. For calculation of the experimental strain, a gauge factor was applied to convert the data from data acquisition system to the experimental strain. Theoretical strain was computed from Equation A2 (Appendix A) by application of Equation B5 and Equation B11 (Appendix B). This gauge factor is shown in Equation 4-2. As compressive strain has no serious change in strain captured by FOS (Detailed in section6.8.1) the same graph is used in Figure 4-12 and Figure 4-13**.**

Equation 4-2 $$\text{Gauge factor (GF)} = \frac{Max.\ \ strain\ reading}{\varepsilon u_{frp}}$$

The following figures show the strain values recorded by the FOS installed on the main reinforcing bar and on the supplementary bar. The maximum strain values were found to be 12,000 με occurring in the immersion and in the outdoor conditions. As it can be observed in

Figure 4-12 the strain measurement in Control2 was not available beyond a load level close to 80% of the ultimate load because of a technical problem in instrumentation.

The results indicated that the FOS installed on the main and supplemental bars performed well except in the case of the Immersion (Imm) condition (Figure 4-16). In the Outdoor (Figure 4-13) and W&D (Figure 4-14) conditions, the measured strains on the main and supplemental agree within reasonable accuracy.

In W&D, the strains in the supplementary bar and in the main bar are close to each other (Figure 4-16). In W&D, only one of the sensors (W&D1) functioned properly up to a strain level of 3000 με, while it did not work at or above that level due to the faulty installation (Figure 4-14). In the immersion condition, the strain profile on the supplementary bar as captured by Imm1 does not correspond to the main bar strain after a strain level of 6000 με (Figure 4-16). In the Imm2 specimen, the FOS on the main bar worked properly, but the FOS on the supplemental bar did not function. These uncertain results in immersion condition can be due to the probable detachment of the main and/or of the supplemental bars or to the disconnection of some of the sensors upon exposure to alkaline solution.

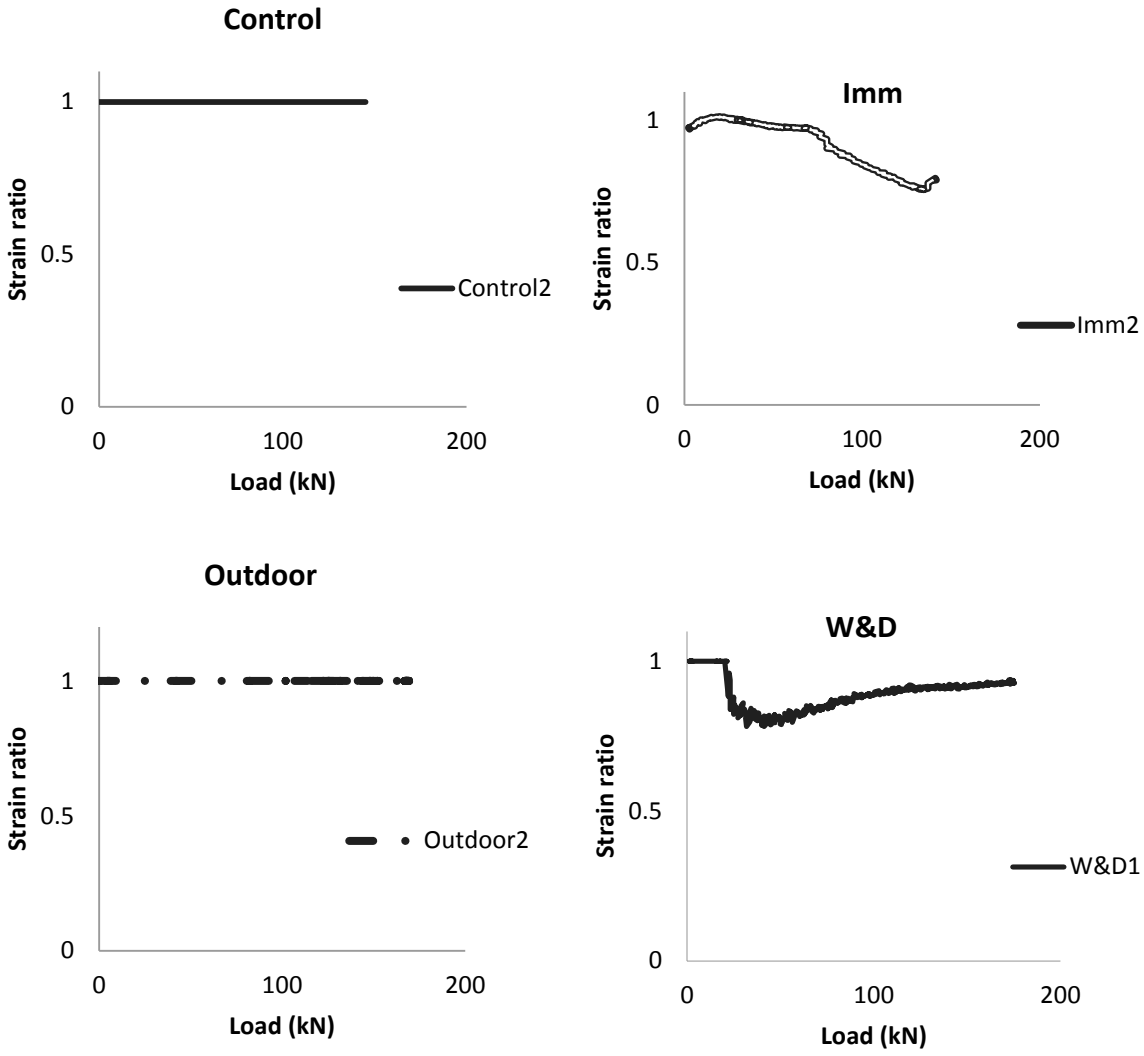

Figure 4-11 Strain ratio (FOS-M to FOS-S) in different conditions

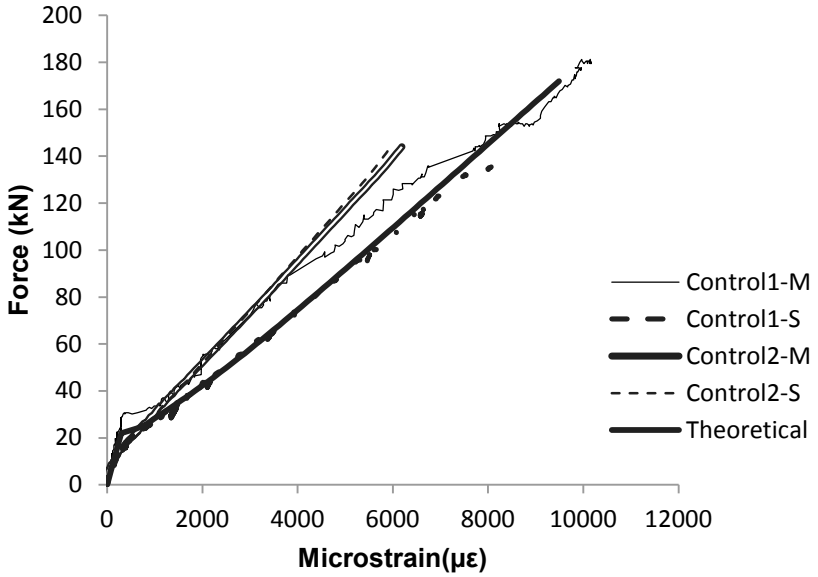

Figure 4-12 Experimental and Theoretical Strain for FOS (Control)

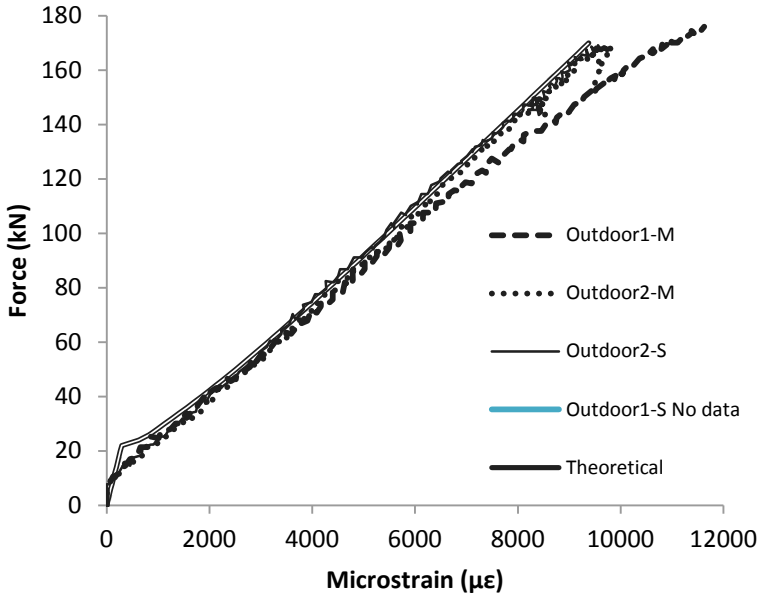

Figure 4-13 Experimental and Theoretical Strain for FOS (Outdoor)

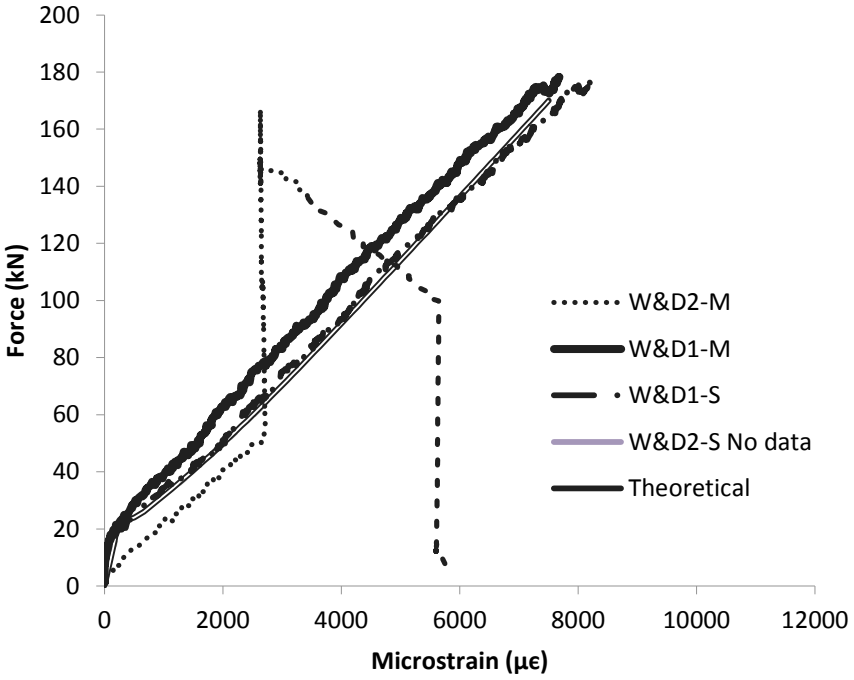

Figure 4-14 Experimental and Theoretical Strain for FOS (W&D)

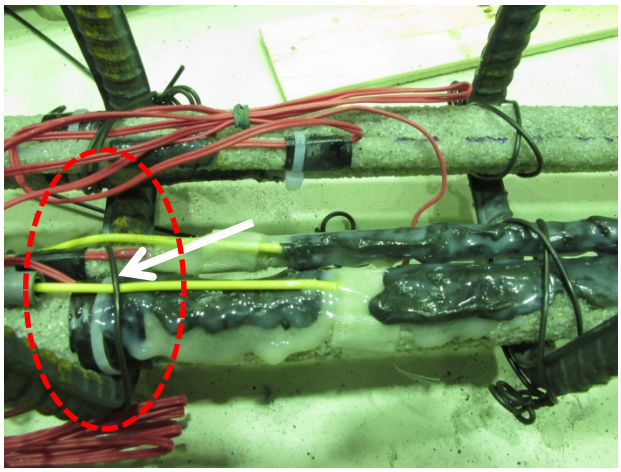

Figure 4-15 Faulty installation of FOS in W&D

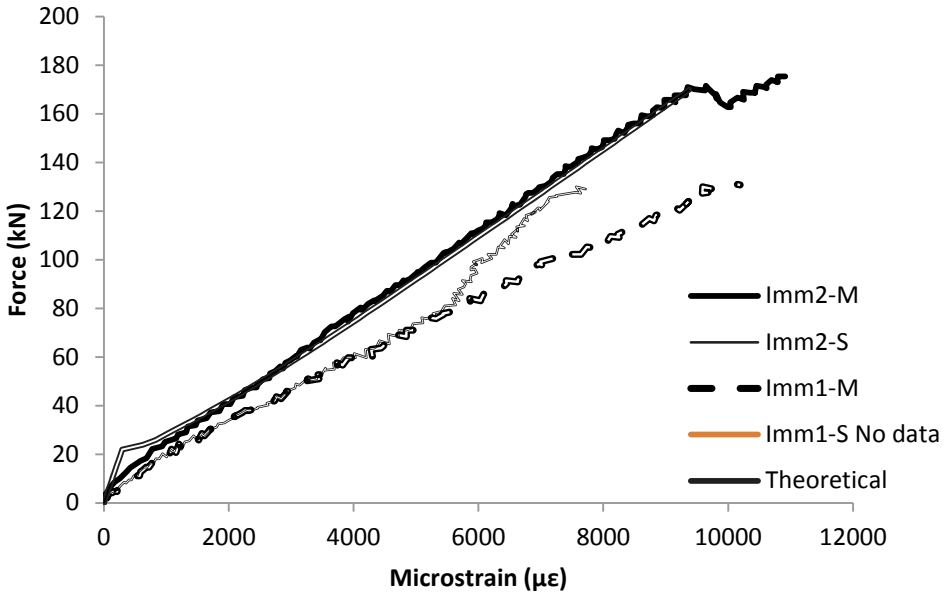

Figure 4-16 Experimental and Theoretical Strain for FOS (Imm)

4.6. ESG Strain Results

As it can be seen in Table 4-6 ESGs did function properly in all conditions except immersion. The ESGs at the mid-span were affected by the alkali environment in immersion condition even though they were coated by tar and protective layers. The pre-cracking of the conditioned specimens created cracks in this region where fluid may penetrate. The top ESG never exposed with alkaline solution as the level of solution in the containers where designed under the level of top ESGs. Top ESGs are intact in all conditions which implies with perfect resistance of ESG and applied coating in concrete pore solution.

Table 4-6 Functionality of ESG sensors

Condition	Control1	Control2	W&D1	W&D2	Outdoor1	Outdoor2	Imm1	Imm2
ESG-L	✓	✓	✓	✓	✓	✓	×*	✓
ESG-R	✓	✓	✓	✓	✓	✓	✓	✓
ESG-M1	✓	✓	✓	✓	✓	✓	×*	×*
ESG-Supl1	✓	✓	✓	✓	✓	✓	✓	×*
ESG-M2	✓	✓	✓	✓	×	×	✓	×*
ESG-Supl2	✓	✓	✓	✓	✓	✓	✓	×*
Top	✓	✓	✓	✓	✓	✓	✓	✓

×* Malfunctioning; × Cut /disconnected wire

4.6.1. Comparing ESG Measurements at Mid-span

Figure 4-17 shows the variation in strain in the specimens at different conditions except immersion, measured using ESGs and FOS (Figure 3-2). Ahmed et al. (2011) performed a full-scale test and measured strain by inserting FOS in FRP and ESG and their results indicates that strains measured using the FBG are slightly higher than measured using the strain by ESG in the cracked stage of the tested beams which conforms the results from this research. The test results for three conditions agree with their findings.

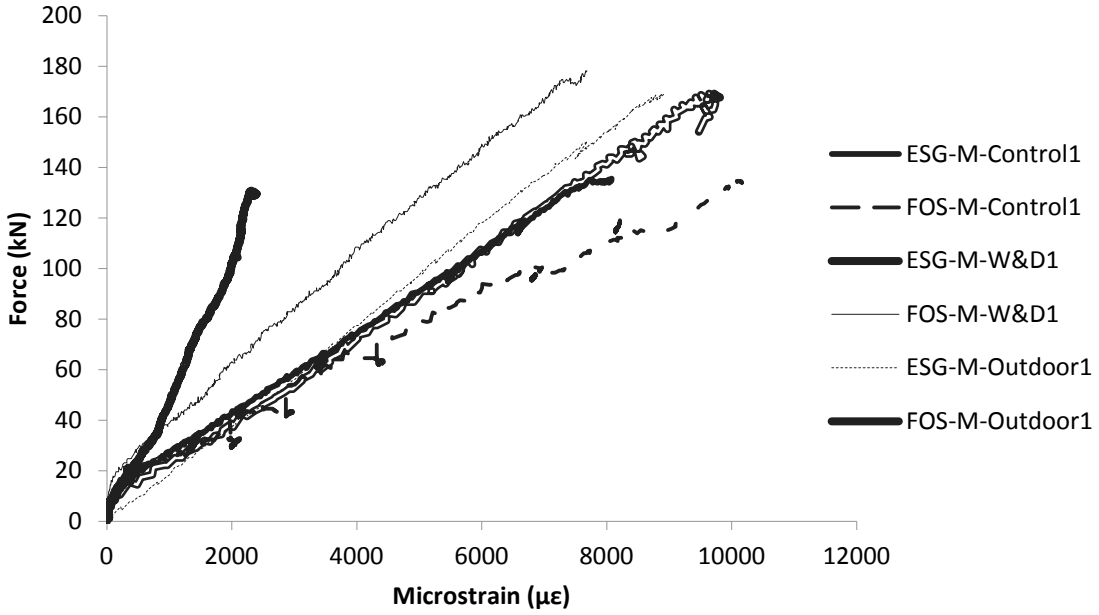

Figure 4-17 Comparison of strain measured using ESG and FOS

4.6.2. ESG Measurements along Main Bar

Strain was measured at several points along the main FRP reinforcement (Figure 4-18 to Figure 4-20). The sensors were placed at mid and quarter spans (Figure 3-2a). These strains were analysed for only one beam of each type of conditioning except immersion. Figure 4-18 shows that the strain at the mid span in a Control1at the loading level of 50 kN was less than the strain measured at its left and right quarter spans as the beam is uncracked and at the location of the applied load shows temporarily more strain. By increasing the applied load and crack propagation the mid-span strain increased and as the crack width at the flexural span gets wider than shear span some detachment to the rebar and further flexural curvature makes the recorded strain for the middle sensor more than left and right sensors. Although in Outdoor and W&D specimens, the mid-span ESG always showed more strain than the two quarter-span sensors for

the pre-crack loading. As seen from Figures 4-18 to 4-20, the strain readings from the left and right quarter-span gauges are not identical because of likely eccentricity in loading or the placement of the sensors.

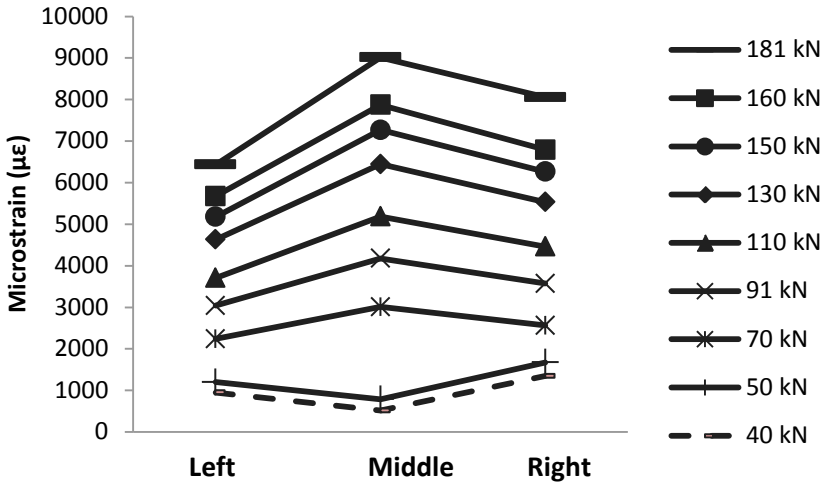

Figure 4-18 Measured strain in main bar for ESGs in Control1.

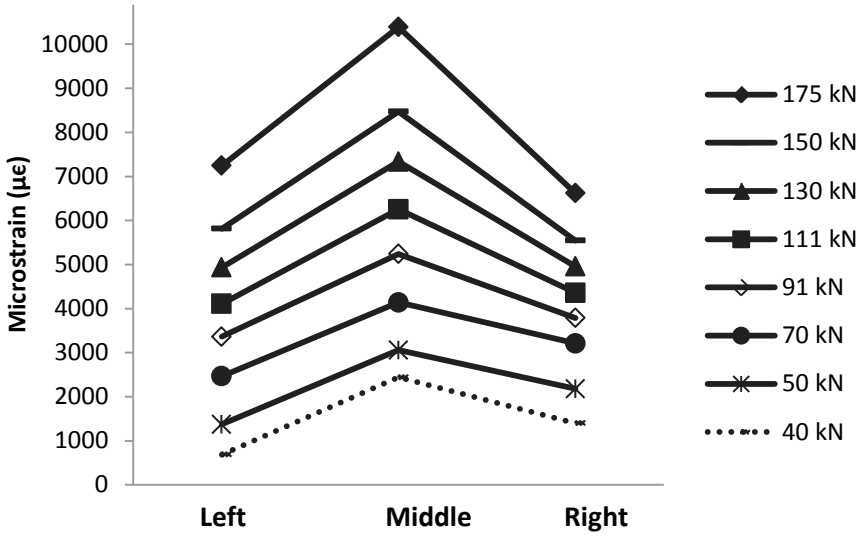

Figure 4-19 Measured strain in main bar for ESGs in Outdoor1

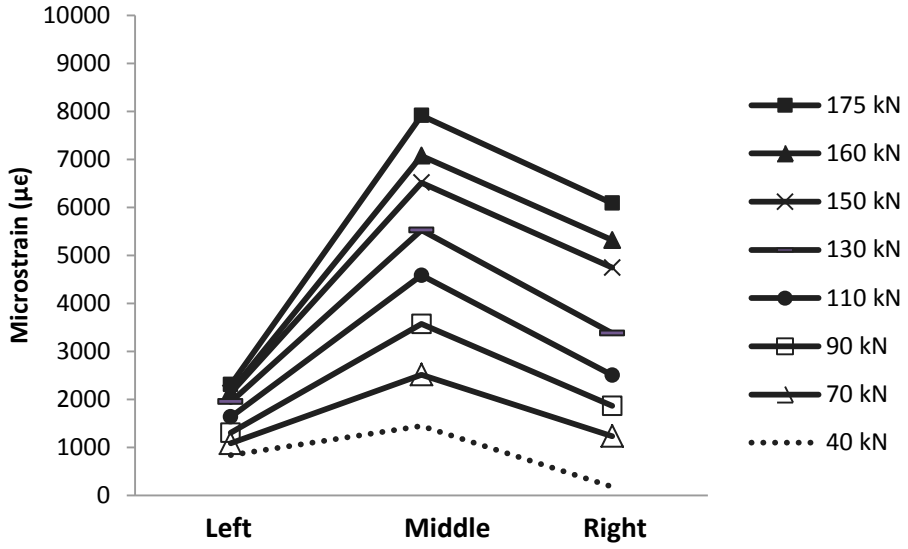

Figure 4-20 Measured strain in main bar for ESGs in W&D1

4.6.3. Moment-strain Behavior under Different Conditioning

The bending moment at the three locations where ESGs were installed and the corresponding strain values are plotted are shown in Figure 4-21 to Figure 4-24. The strain values recorded using the ESGs at these locations are shown in these figures, while the locations of the ESG installed on the main rebar have been presented earlier in Figure 3-2a.

The moment-strain relation in each case as shown in Figure 4-21 to Figure 4-24 can be idealized as bilinear curves with the change in slope at the cracking moment, M_{cr}. In that case, the flexural strain can be estimated using the following formula: $\varepsilon = My/EI_e$, where E is the modulus of elasticity, I_e is the effective moment of inertia of the beam section, and y is the distance from the neutral axis. The effective moment of inertia (I_e) of a cracked section is almost 2/3 of that at the level of *Mcr***.** It should be noted that the Outdoor1 and W&D1 specimens were pre-cracked (partially cracked at the mid-span). Therefore, the moment-strain curves at the mid-span of these specimens do not clearly show a clear transition in slope of the curve as they capture only the post-crack behavior. By comparing ESG-M with Theoretical-M from mid-span strain as captured by the main bar, ESG-M is found to be very close to the theoretical value in the cases of Outdoor1 and W&D1, while for the Control1 specimen, it is found to be higher. The strain values captured by the ESGs at the left and right quarter-spans (ESG-L & ESG-R) in all the tested conditions are found to be less than the corresponding theoretical values. As a result, the theoretical value of the strain is found to be conservative in all the conditions.

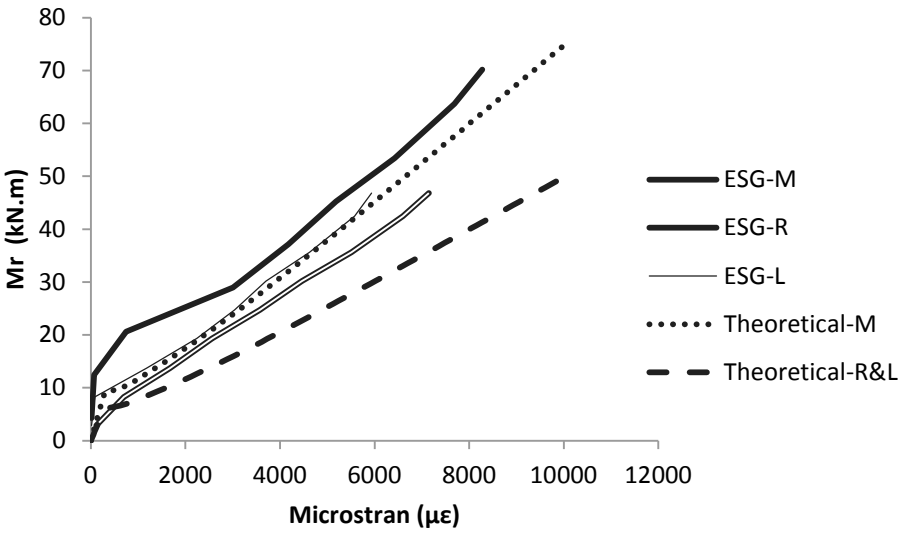

Figure 4-21 Applied moment vs. strain in the Control1 specimen

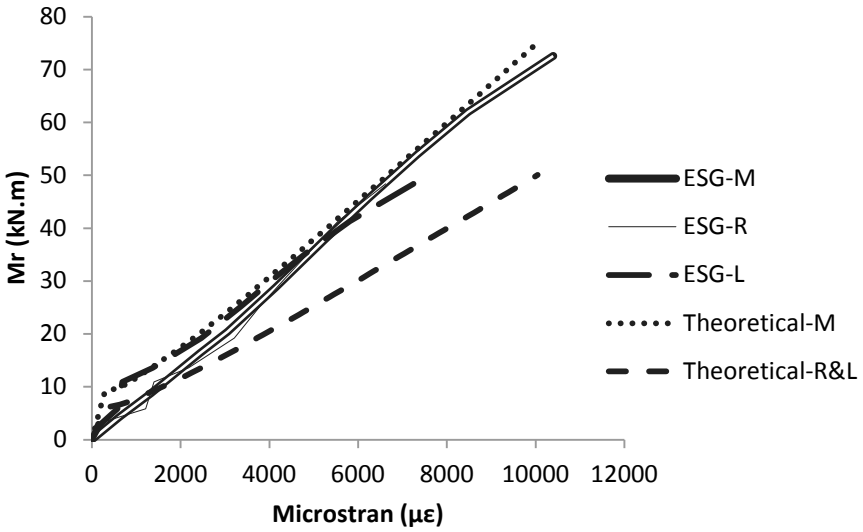

Figure 4-22 Applied moment vs. strain in the Outdoor1 specimen

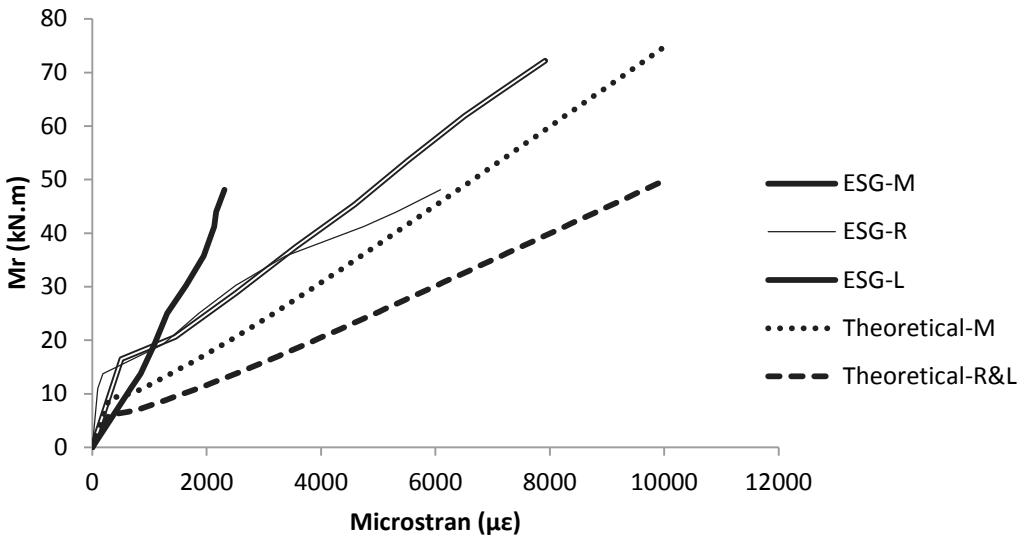

Figure 4-23 Applied moment vs. strain in the W&D1 specimen

4.7. Effect of the Bond Characteristics in FRP-RC Beams

Equation 4-3 can be applied for calculating the relative bond in all conditioning types (Broomfield 1997). Strain from the middle gauge and average from intact right or left gauges was used in this formula. For W&D specimen, the strains at the quarter spans measured using the ESGs are deemed to be reliable as the moisture ingress and the effect of the chemical solutions were minimal in those locations since the beams were not cracked at those locations. The ESG readings in immersion condition are not reliable so those specimens were excluded from the study presented in this section.

Equation 4-3 $\tau = \frac{Ed(e_2 - e_1)}{4L}$

where; τ is the shear stress; E is the Modulus of elasticity of GFRP; D is the diameter of the GFRP bar; L is the distance between two strain gauges (400 mm, in this case); and e_1 and e_2 are

the strain measured at the mid-span and at a quarter-span (average of the strains from the left and right sensors).

In Figure 4-24, the trend of the shear stress vs. force curve is very close in Control1 and Outdoor1 with maximum bond stress of 1.0 MPa and turning point at cracking load level. In Outdoor1 specimen, the bond stress is double that of the other conditions (2.0 MPa) for because of the high deformability (Figure 4-7) in this condition. At P_{cr} more debonding and cracks were deemed to initiate at the region of the middle sensor, which lead to a bigger difference in the strain readings for the Outdoor specimen. The drop and the turning point in these specimens can be explained by the balancing of the strain readings after M_{cr} and crack propagation, to some extent, exceeding the strain variation (e_2-e_1) beyond this level of load. The variation of the bond stress with loading as shown are almost linear from M_{cr} up to the ultimate level of loading, and they give a good indication of the performance of the ESGs. In the Outdoor1 specimen, a similar trend, but with a higher level of bond stress is observed, and more tests are needed to verify the accuracy of the bond stress.

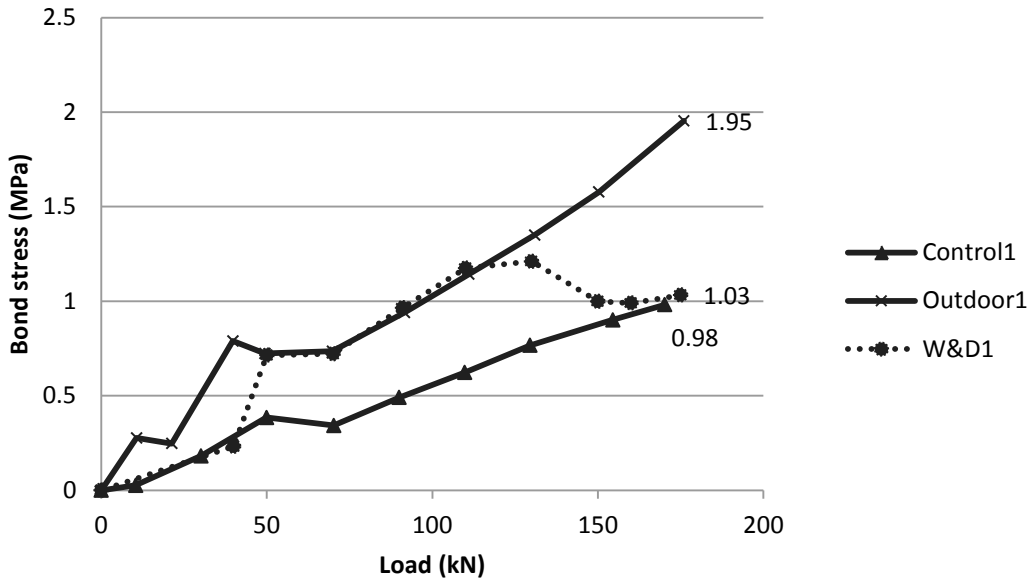

Figure 4-24 Bond in Control, Outdoor and W&D conditions

Strain measured using ESGs in immersion is not reliable, as most of the ESGs in this case did not work. An evaluation based on the results of these beams reveals that on application of the maximum strain of $0.72\varepsilon_u$,$0.65\varepsilon_u$, $0.53\varepsilon_u$ in FRP bars in Outdoor1, Control1, and W&D1 specimens, respectively, the relative maximum bond stress reached 1.95, 1.03, 0.98 MPa, respectively. The bond stresses in the Outdoor and W&D specimens can be greater than those in the Control specimen because of the presence of moisture. A similar observation was made in the pullout tests conducted by Bank et al. (1998). Bond strength study for the GFRP(Φ19) according to RILEM shows 0.7 to 6.6 MPa for the slip of 0.01 and 0.2 mm respectively which for this test set up specification lower band of bond (0.7 MPa) seems more close to our experiment (Benmokrane et al., 1996). The bond stress in W&D1 has a turning point which can be explained as degradation of aggregates under cyclic flow of alkaline solution in the pores.

5. Microstructural Examination of FRP Reinforcement

5.1. Introduction

Since it has been shown that alkali exposure can influence FRP, this chapter investigates the effects of external alkali exposure on microstructure and internal alkali content. Reinforcements from the control, immersion and cyclic immersion tests were examined (Outdoor conditions were not studied in this portion of the research). A scanning electron microscope (SEM) was used to perform a visual examination and assess the alkali concentration, as described in Chapter 3. For the visual observations, it was found that coating the samples with palladium (30%) and gold (70%) was necessary to obtain images with acceptable quality. The results are presented in the following sections:

- Visual examination of FRP reinforcements;
- Alkali concentration of bare bars; and
- Alkali concentration of embedded bars
    - Effect of the interface
    - Effect of compaction on alkali concentration

5.2. Mechanical property

The glass FRP bars used here were manufactured by a Canadian company Pultrall Inc. They were sand coated to enhance the bond. The bars were made of continuous E glass fibers impregnated in a vinylester resin using the pultrusion process. The mass fraction of glass is 81.5% and was determined by thermogravimetric analysis according to ASTM E-1131 standard (ASTM International, 2003b). Their relative density according to ASTM D 792 standard is 1.99 (ASTM International, 2013). The mechanical and physical properties of 12.7 mm diameter GFRP bars, as provided by the manufacturer, are summarized in Table 1.

5.3. Visual Observations

The visual microscopic observations revealed significant damage after 14 months of immersion in alkaline solution. The micrographs in Figure 5-1 were taken near the exposed edge of the FRP reinforcement and show that the damage is most prevalent at the interface between the fibers and the resin in the immersion-embedded FRP sample. Damage occurs in the glass fiber, and as noted in the literature review, this is the component most susceptible to alkali attack. All fibers are in the immersed sample are visibly damaged. The Control-embedded and W&D-embedded bars do not show severe damage; outdoor specimens were not investigated. Robert et al. (2009) found similar results from comparing visual study of conditioned GFRP bar aged in moist concrete at 50°C for 240 days and control condition specimen.

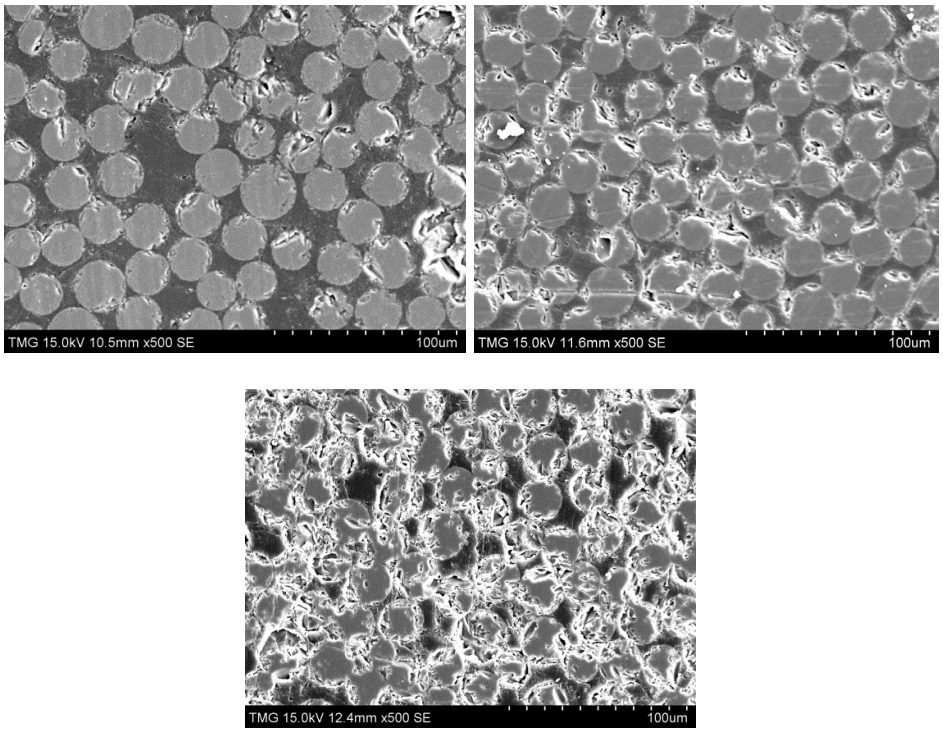

Figure 5-1 Micrographs of FRP (x500 magnification) Control-embedded (Top-Left), W&D-embedded (Top-Right), Immersion-embedded (Bottom)

Prior to quantitative analysis, elemental mapping was performed on one immersed bare bar to visually assess penetration of alkalis. This type of scanning requires several hours to conduct, so only one bar was assessed using this method. The image shown in Figure 5-2 was a portion of the rebar at the outer edge (edge at the left side of the image). As is displayed in the Figure 5-2 to 5-4, penetration of sodium and potassium is evident up to almost 1 mm from the edge of the bar while calcium and silicon are found throughout the composite. Calcium was found primarily in the resin, while the glass fibers were the main source of silicon.

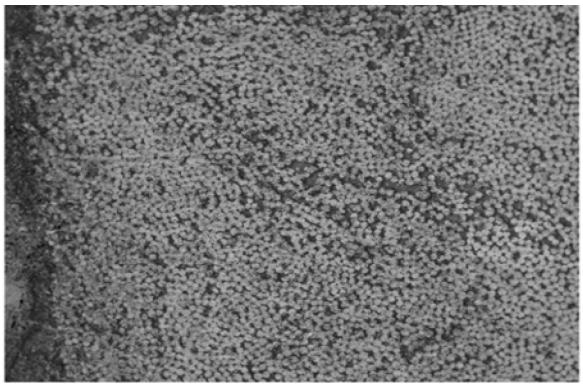

Figure 5-2 Fiber structure

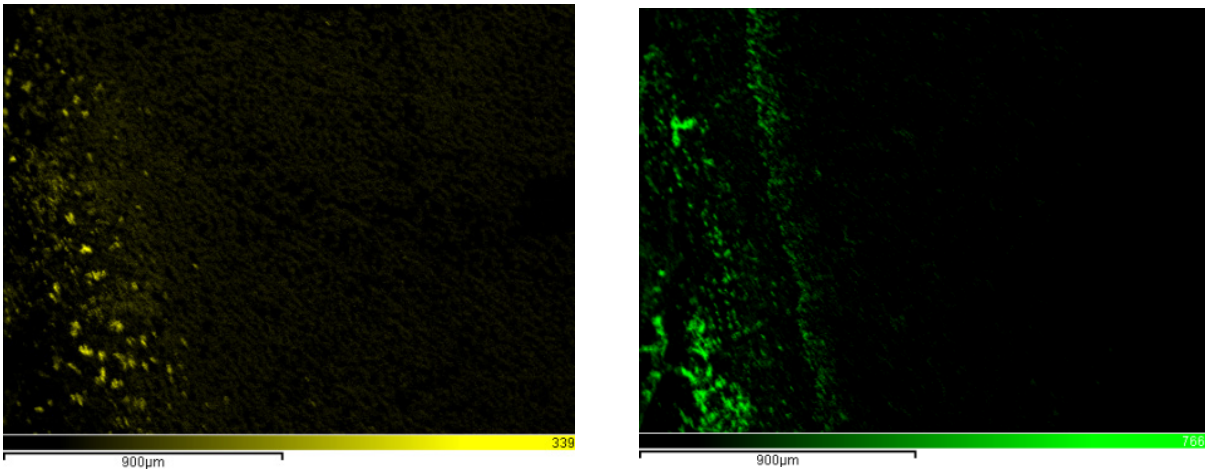

Figure 5-3 Left- Sodium (Na) Right- Potassium (K)

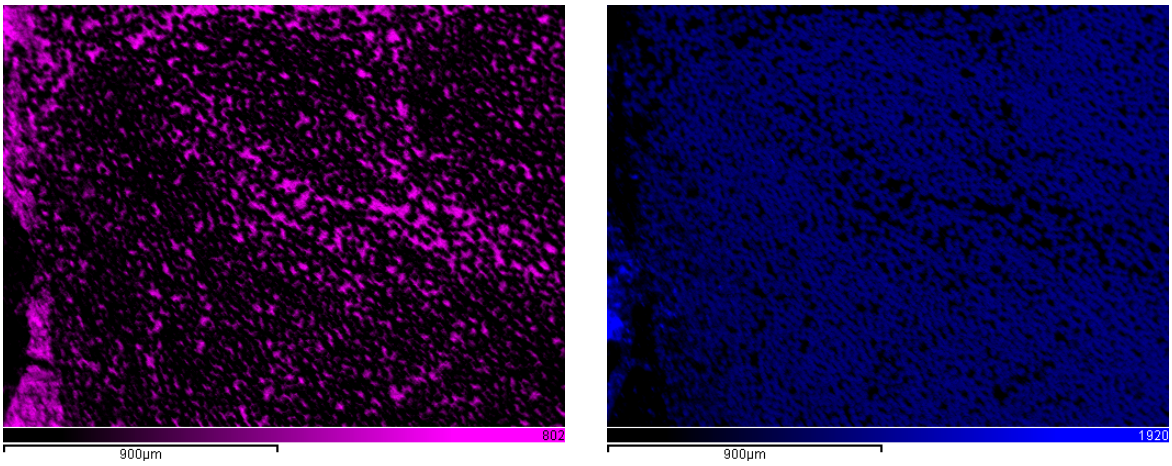

Figure 5-4 Elemental map at edge of immersed FRP bare bar (Left: Ca, Right: Si)

5.4. EDX Analysis

5.4.1. Bare Bar

Elemental analysis was carried out approximately every 1.3 mm along the diameter of the 19 mm FRP bar by a square spectrum. Each spectrum encompassed an area of approximately 0.2 mm^2. In analyzing the FRP rebar, two perpendicular directions were scanned and analyzed and the average percentage of weight per spectrum for sodium and potassium is presented. Since radial diffusion occurs, it is expected that the results from the two directions would be similar. The presence of Na and K in the Control sample is minimal, as seen in Figure 5-5. In comparison, the concentrations of Na and K in both the Imm and the W&D samples are noticeably higher (Figure 5-6 and 5-7). In the continuously-immersed sample (i.e. Imm), the penetration of K is much less than that of Na (about one-third). This trend can be explained by the heavier atomic weight of K (39.098 amu) versus that of Na (22.990 amu). Under such conditions, the diffusion of molecules through the FRP is slower for molecules with heavier atomic weight.

In the immersion condition, the penetration of Na and K shows a convex trend which implies diffusion of ions towards the center of the reinforcement (Figure 5-6). With W&D conditioning, this trend is not remarkable and shows more uniform penetration; however, penetration is still observed. The W&D conditioning imposed cyclic immersion of 3 days followed by 4 days of drying, so discontinuity in aqueous flow makes for a lower concentration of alkali. It can be observed that the penetration of alkali in the immersion condition is approximately four times higher than that with the W&D conditioning.

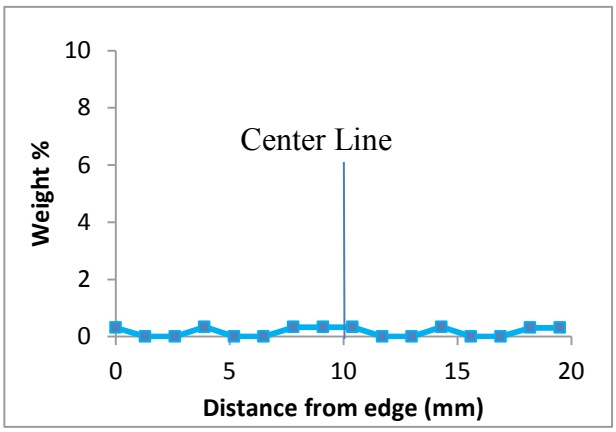

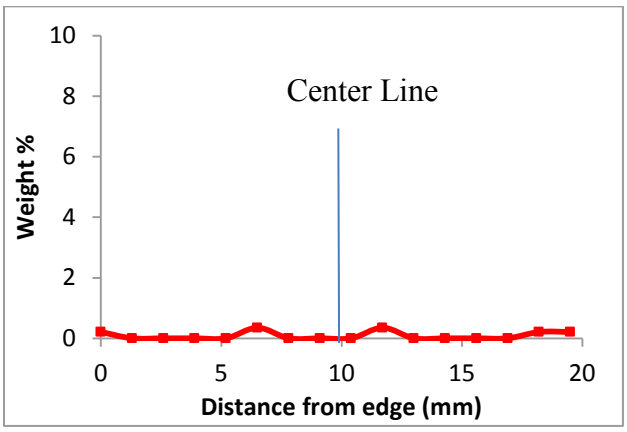

Figure 5-5 Concentration of Na (left) and K (right) in the bare bar (Control)

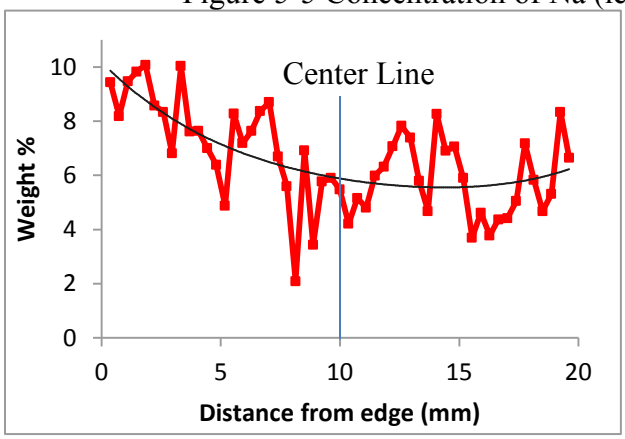

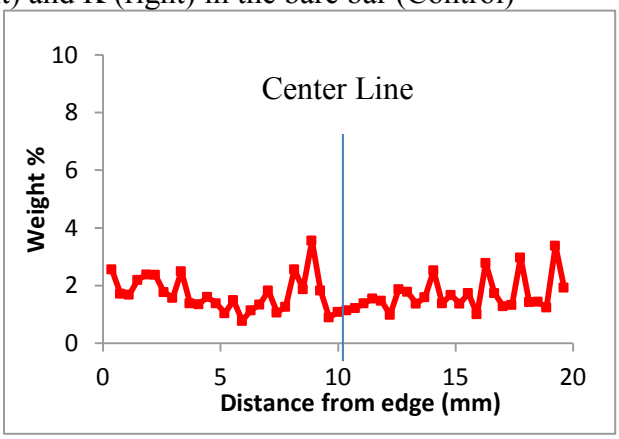

Figure 5-6 Concentration of Na(left) and K(right) in the immersion (Imm) bare bar

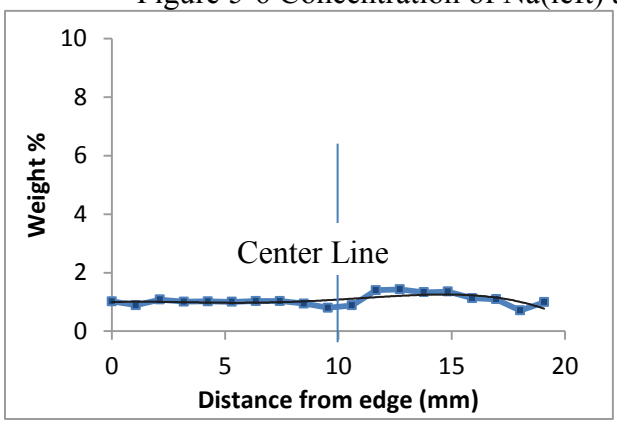

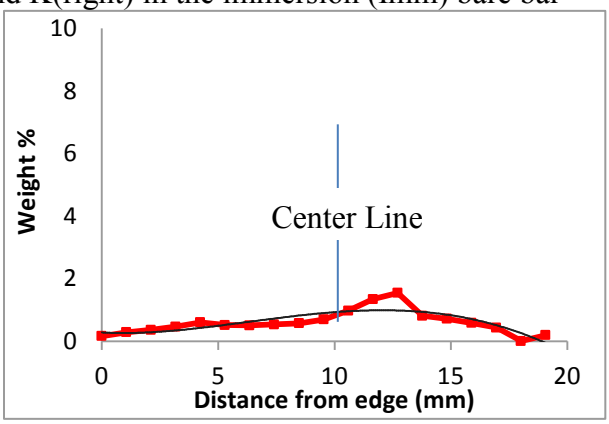

Figure 5-7 Concentration of Na (left) and K (right) in the cyclic immersion (W&D) bare bar

5.4.2. Embedded FRP

5.4.2.1. *Alkali Concentration of Embedded FRP in Concrete*

The most severe exposure condition was the continuously immersed case, and so a comparison of alkali concentration in a bare bar and in an embedded bar that were each continually immersed is shown in Figure 5-8 and Figure 5-9. In this investigation, W&D-conditioned and Control-embedded reinforcements did not show any sodium and potassium penetration. As previously mentioned, the elemental concentration in two perpendicular directions were averaged. It was observed that sodium concentrations were significantly higher in the bare bar than in the Imm-embedded bar. However, for potassium concentration, the differences in concentration for these two cases are not nearly as noteworthy. For both elements, concentrations in the embedded bar are still far higher than the fractions of weight percent seen in the unexposed (Control) samples.

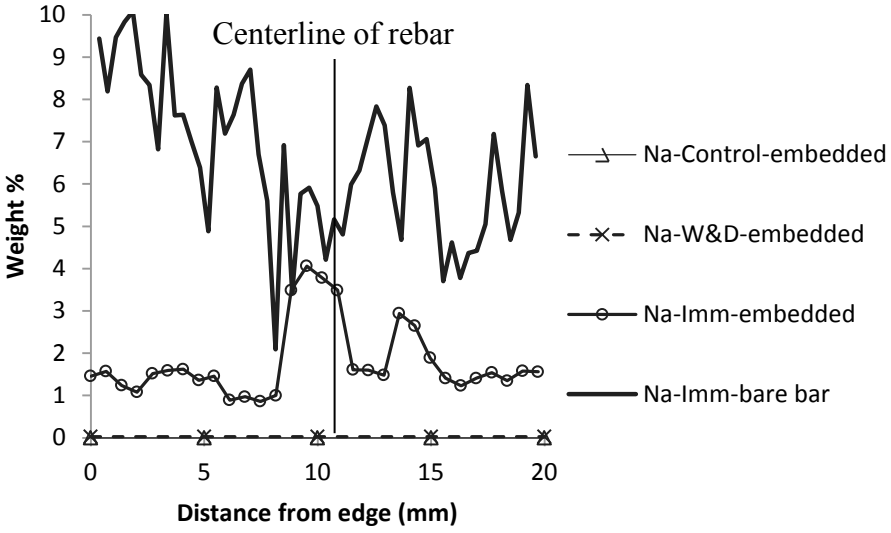

Figure 5-8 Concentration of sodium in continuously immersed bars

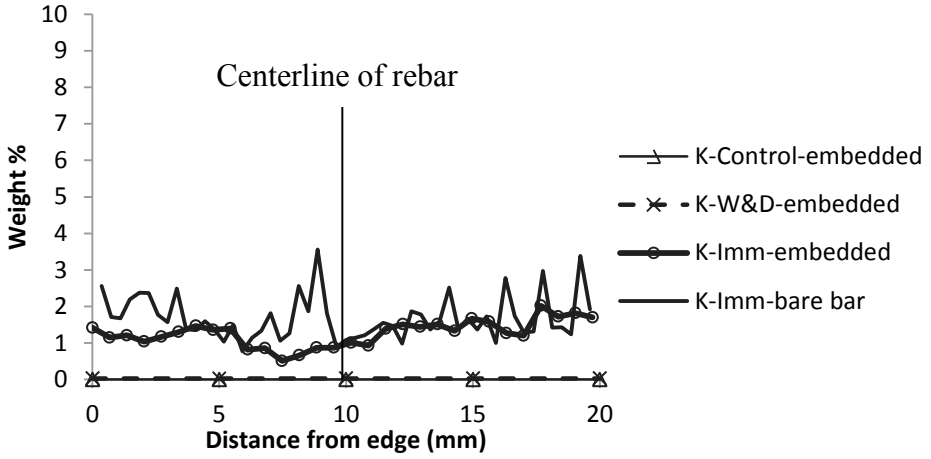

Figure 5-9 Concentration of potassium in continuously immersed (Imm) bars

It should be noted that the Immersion condition is too aggressive as compared to a real field condition. However the field condition is variable, and the Immersion and Control conditions would serve and two boundary conditions for the purpose evaluating the effect of weathering. The wet and dry (W&D) and outdoor (Outdoor) conditions would simulate the field condition better. However, the outdoor specimen is not loaded, while, in reality, the field structures are loaded. In that case, the weathering effect in a field structure (loaded) is expected to be more severe than what was found in the cases of W&D and Outdoor conditions, but milder than that in Immersion condition.

5.4.2.2. *Embedded FRP/Concrete Interface*

Investigation of the alkali concentration specifically at the FRP and concrete interface is worthwhile as it affects the debonding and degradation of the bond, as observed by Micelli and Nanni (2004). .Based on an accelerated test using high temperature (80 °C), Bank et al. (1997)

concluded that FRP is an inappropriate material for reinforcing concrete, and they also observed significant degradation of the polymer resin in the surface region of FRP. An average of four to six spectrums at each distance were used to determine the alkali concentration on the reinforcement embedded under the Control and Imm conditions. Each group of spectrums on the FRP and on the adjacent concrete are indicated by straight dotted lines (Figure 5-10 and Figure 5-11). The first set of spectrums is within the FRP rebar; the second in the interface (that contains the surface sand layer of the FRP) and the third set in the cement paste surrounding the rebar. Comparing the total alkali levels in Figure 5-12 shows that alkalinity drops at the interface in both conditions, but more significantly in the immersion case. The drop in alkalinity is not as significant in the Control specimen as in the Imm-conditioned beam as the concentration of alkali and hydrostatic pressure is much less in the Control case. The effect of swelling of FRP is another internal pressure which can neutralize hydrostatic pressure of alkalis at the interface and makes it denser by compressing the granular materials, paste and water which lead to a decrease in the alkalinity. The reason for the low concentrations may be aqueous flow with vibration of the formwork during placement which led to bleeding or poor compaction under the reinforcement. The issue of compaction voids near the interface is treated in the next section. As distance increases from the interface alkalinity increases. In one of the samples from the immersed condition, the total alkali concentrations are higher both in the FRP and in the cement paste. It may be that this specimen was taken closer to the surface of the beam.

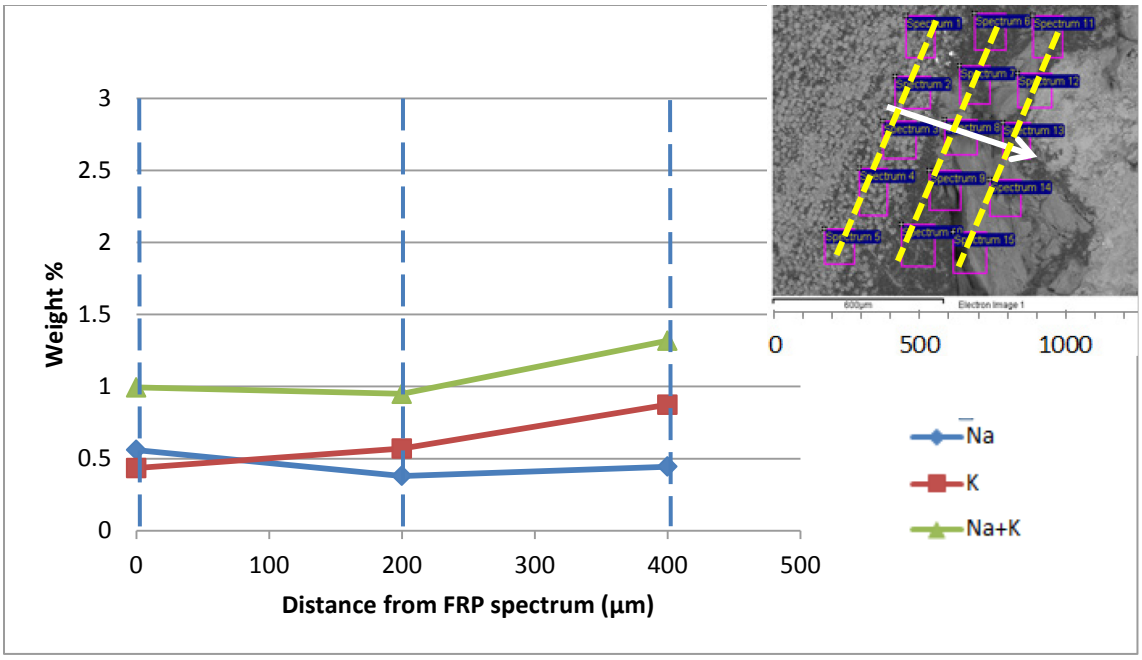

a) Control-a

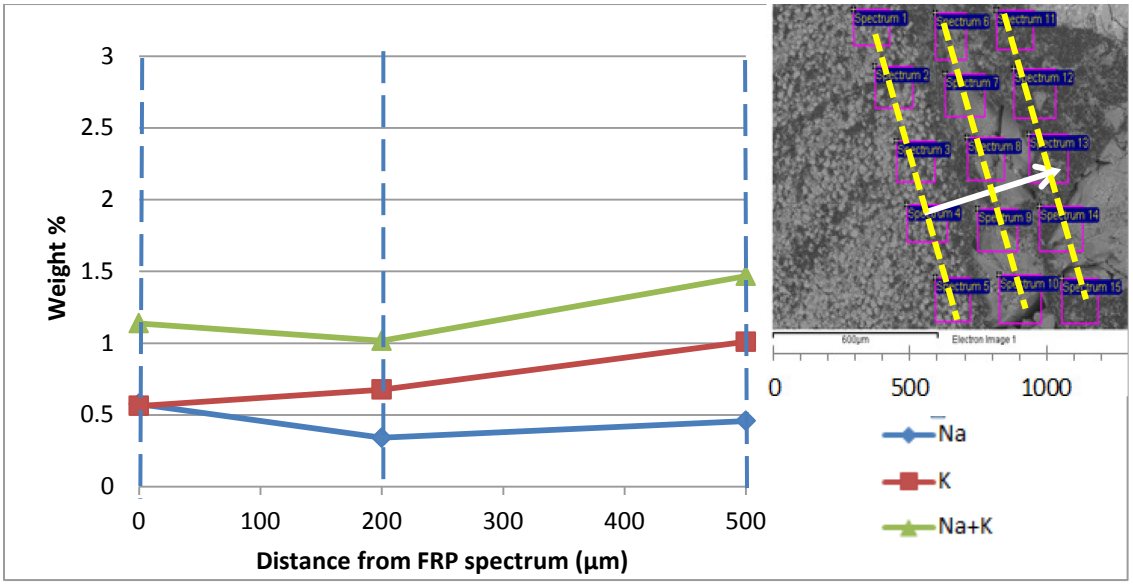

b) Control-b

Figure 5-10 (a, b) Two examples of alkali concentration at an interface – Control beam

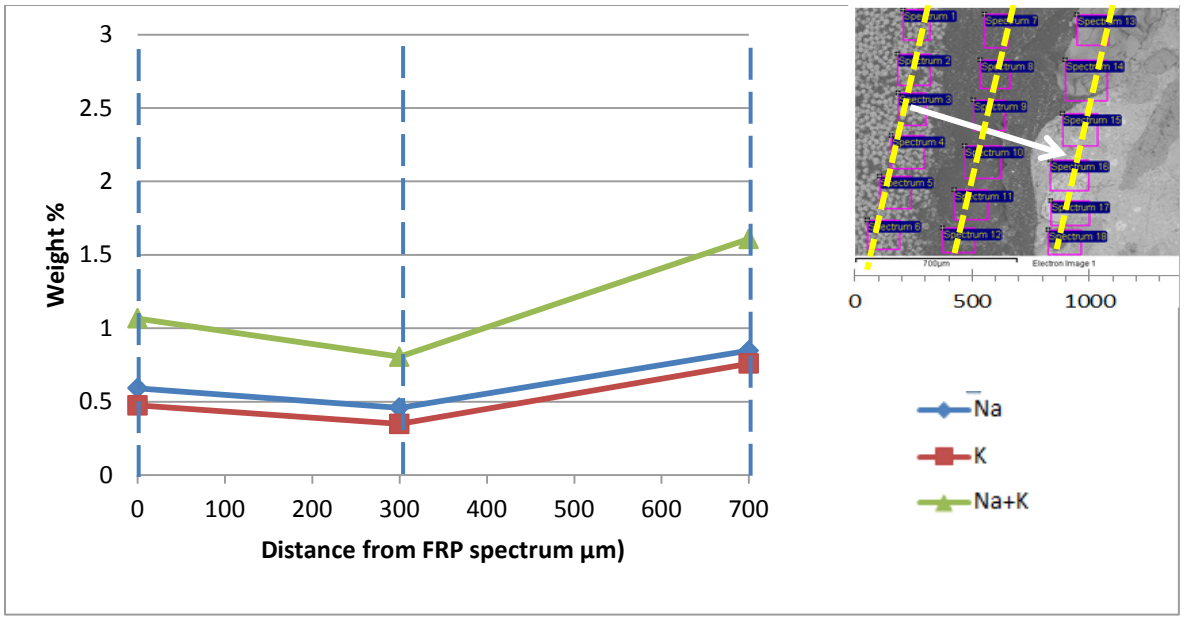

a) Imm-a

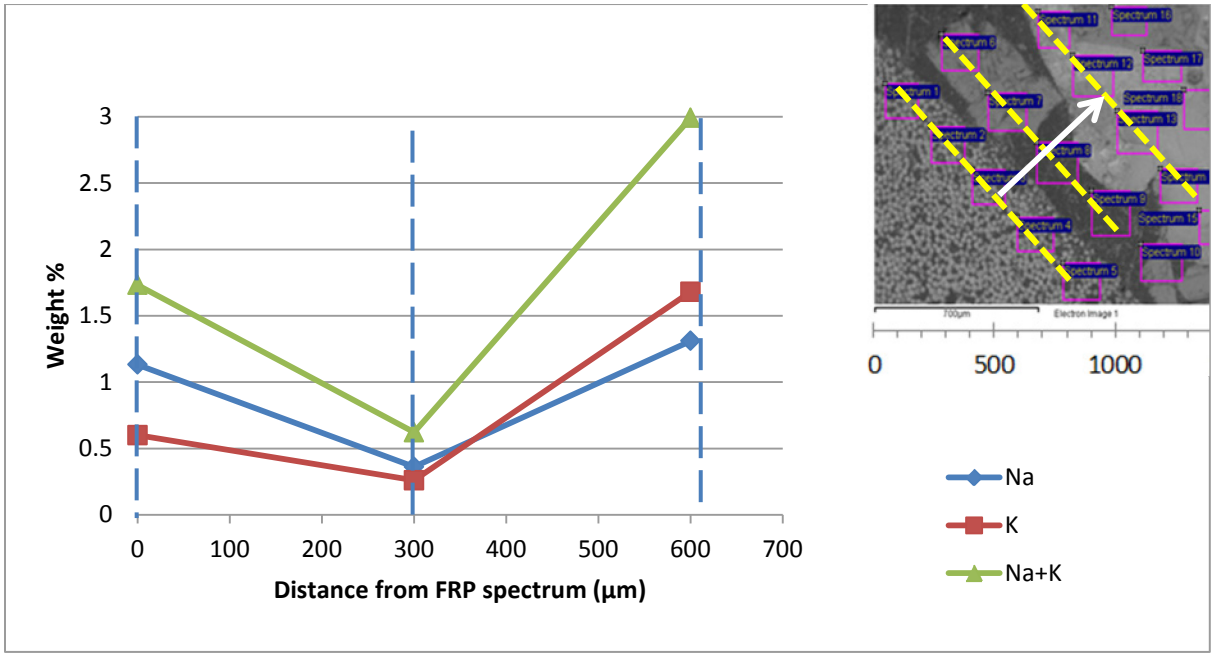

b) Imm-b

Figure 5-11 (a, b) Two examples of alkali concentration at an interface – Immersed beam

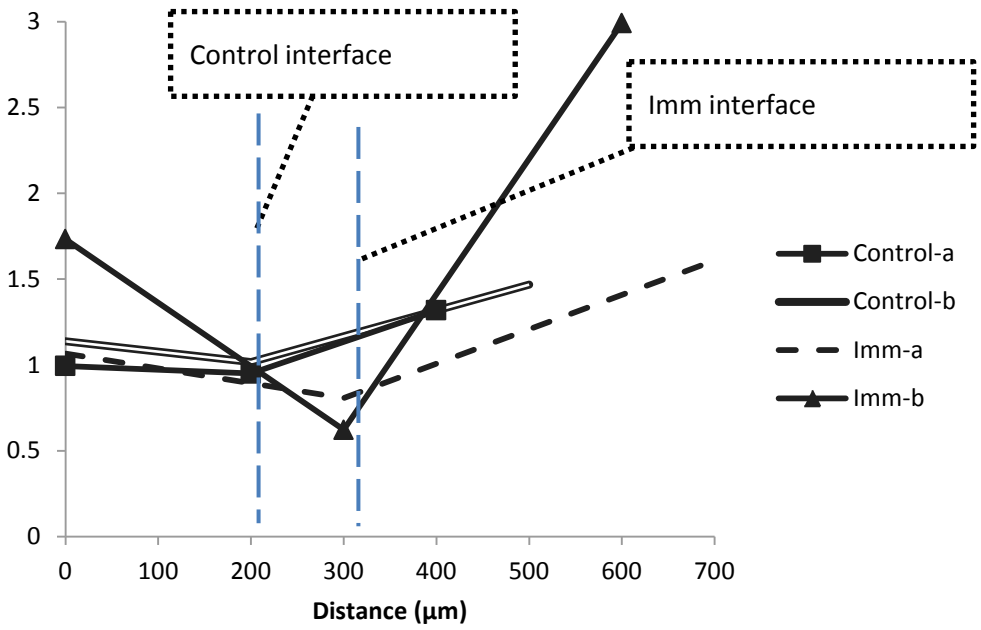

Figure 5-12 Total alkali at an interface in Imm and Control beams

5.4.2.3. *Effect of the Compaction at an FRP Interface on Alkali Concentration*

Certain concrete voids are due to poor compaction or to the accumulation of bleed water. These voids can range between 1 and 10% of the volume of the concrete and allow for a rich flow of the alkaline interstitial solution (Neville, 1996). In reinforced concrete, bleed water can accumulate below the reinforcement. Air can also get entrapped due to poor compaction (Ehsani, Saadatmanesh, & Tao, 1993).

Three different Control specimens were investigated (well-compacted, normally-compacted, and poorly-compacted) for alkali content at the interface. Three sets of points were measured at regular distances from the FRP interface; the first point generally included measurements within the sand coating layer. For every distance, three equal spectrums were selected and their average

weight percentage of each element was determined. The selected specimens represent a range of different compaction levels at the interface, as shown in Figure 5-13 to Figure 5-15. It can be seen that the concentrations of sodium and potassium are low within the sand layer, and are similar irrespective of compaction. Further from the interface, the concentrations increase depending on the compaction. For a well-compacted sample (Figure 5-13), the concentration of K increases significantly, while Na increases only marginally. In normally-compacted and poorly-compacted samples, the sodium increases to a greater extent. Figure 5-16 shows the total alkali content for the three specimens. Comparing the results, it can be clearly seen that compaction influences the alkali concentration. As the compaction improves, more alkalis are found in the area directly adjacent to the reinforcement. The greater the presence of compaction voids around the FRP, the lower the alkalinity; in Figure 5-15 this subject is most evident. In this research, consolidation of specimens occurred via vibration by placing a vibration table below the formwork (Figure 3-5). It is possible that the vibration was either insufficient for compaction, or excessive, causing bleeding. However, care was taken during the placement to vibrate to an extent where entrapped air bubbles ceased to be visible but no bleed water was formed. Total alkali content in the cement paste is variable at distances greater than 2 mm from FRP; approximately 12 % (by weight) in two cases, and somewhat lower in the remaining case. The variability of the weight percentage of alkalis located far from the FRP edge may relate to the analysis direction towards the surface of the beam or towards the center line of the beam. The silica sand on the FRP surface does not likely absorb alkalis. Elemental analysis was carried out on dry samples; it is expected that as the solution dried, the salts were either removed from the porous interface during the polishing process or perhaps transferred onto adjacent solid surfaces.

In reality, these voids may be filled with highly alkaline solutions in direct contact with the FRP reinforcement. For the Control samples investigated, no significant differences in alkali concentration within the FRP were observed. It is possible that the same phenomenon would not be observed in the immersed samples.

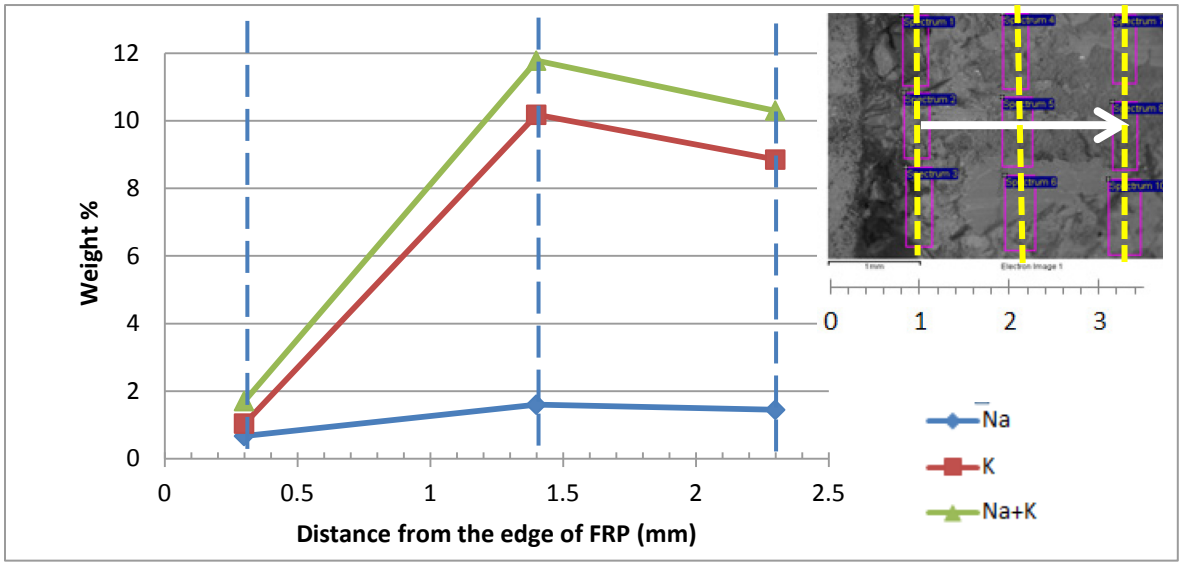

Figure 5-13 Concentration of alkalis at a well-compacted interface for Control beam

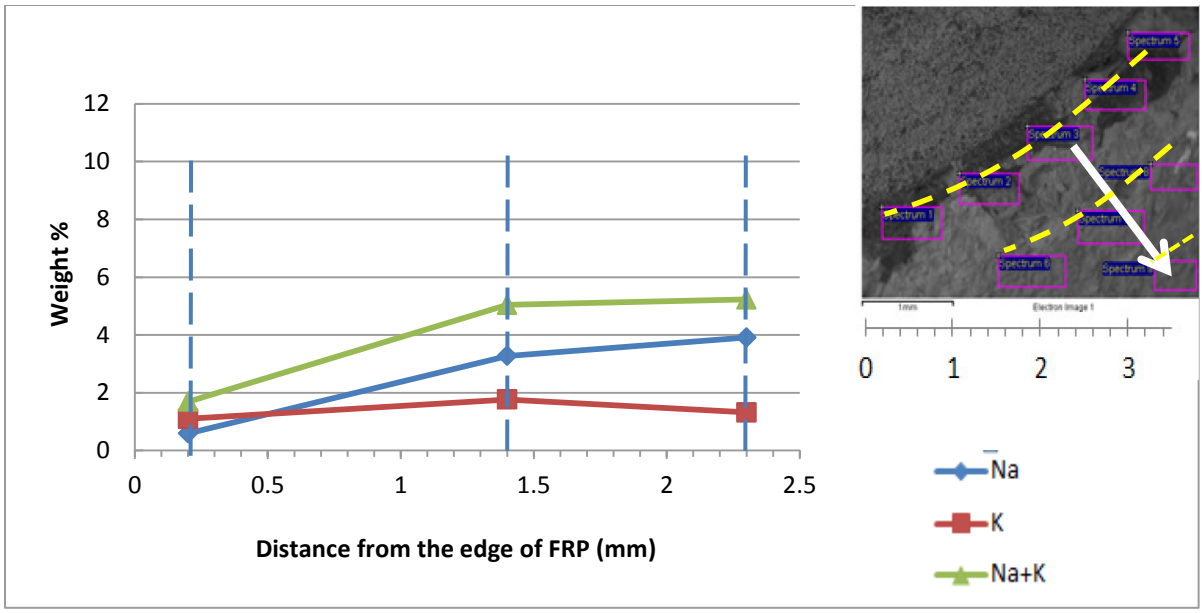

Figure 5-14 Concentration of alkalis at a normally-compacted interface for Control beam

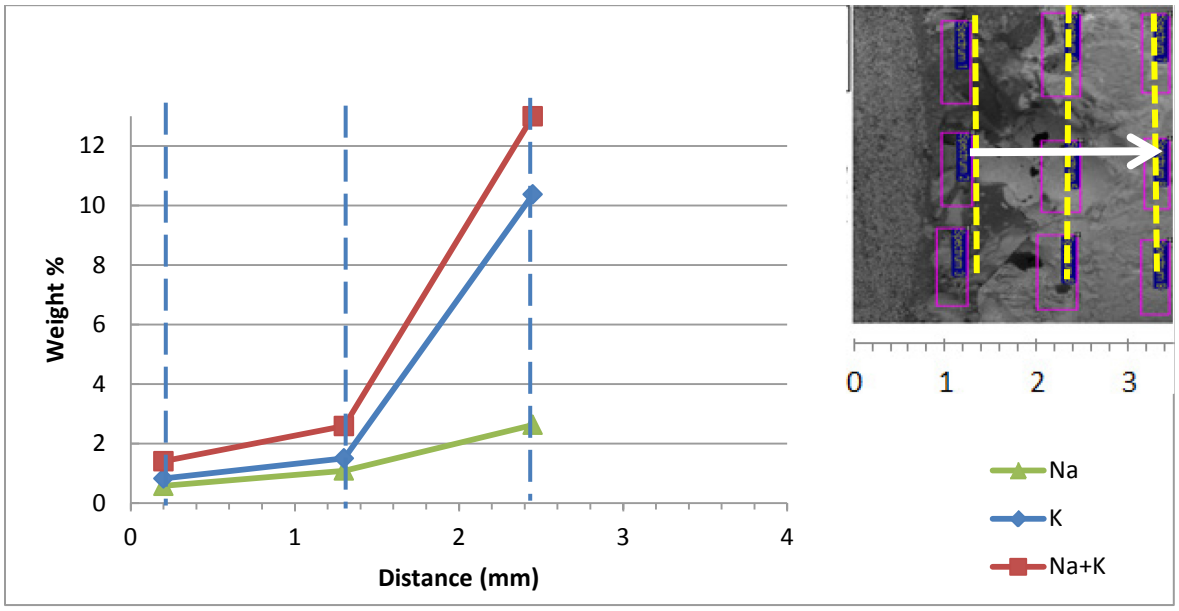

Figure 5-15 Concentration of alkalis at a poorly-compacted interface for Control beam

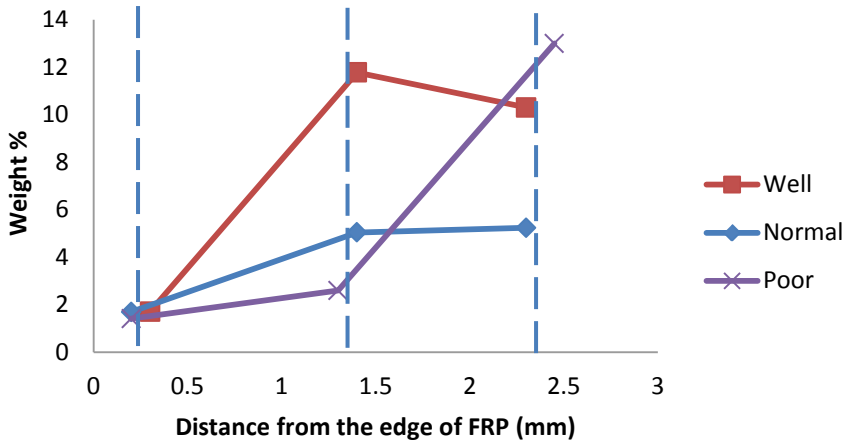

Figure 5-16 Alkali concentration for various degrees of compaction

5.5. Summary

Visual observations showed that continuous immersion in alkaline solution with pH close to that of a concrete pore solution had a noticeable effect on FRPs. Total alkali concentrations measured on both bare and embedded bars showed moderate to significant increases over the Control (unexposed) bare bar. While the bare bar in the immersed condition presented the highest concentrations, embedded bars from the immersed condition showed concentrations three to ten times that of the control bar and in the Control-embedded and W&D-embedded no alkalinity was detected (Figure 5-17). It was found that 25 mm cover was sufficient to protect the rebars for W&D condition from alkali penetration. The Canadian code (CSA S806-12) suggests adding high amounts calcium as one of the alkaline materials in testing. However, as calcium is one of the components of FRP, it is not suitable for analysis by SEM (Figure 5-4). The bars and beams were exposed to the solutions at room temperature for 14 months. Although the exposure may

seem severe in the case of beams, it must be pointed out that most research to date has focussed on the reinforcement of small pull-out samples exposed to both high temperature (typically 60°C) and alkalis, both unrealistic in practice. The research presented here utilizes a solution that may be found in concrete in practice. As well, saturation of concrete in the field is typically very high a few centimeters below the surface (at the level of the reinforcement), so the cyclic and continuous immersions do not necessarily present unrealistic situations.

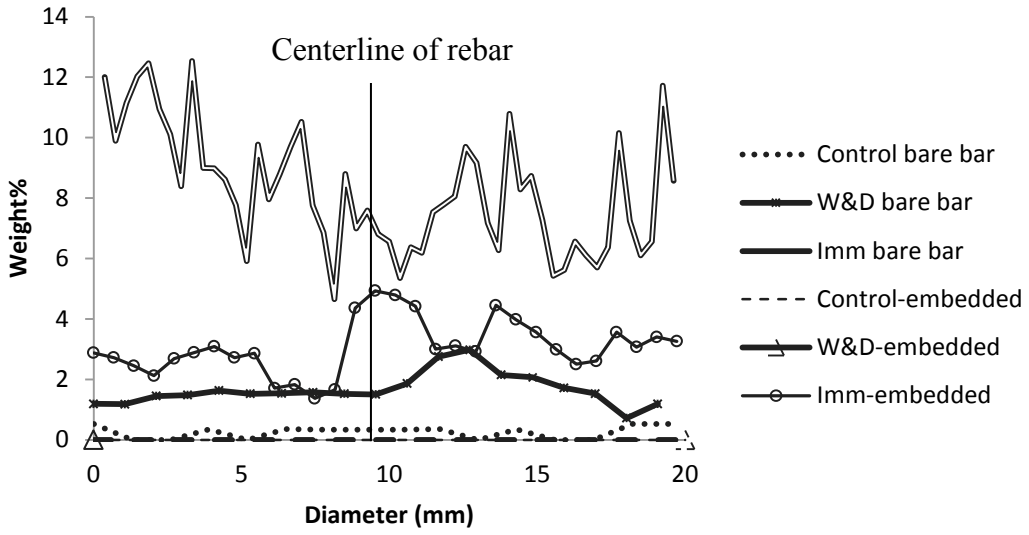

Figure 5-17 Total alkalis in FRP reinforcement

Investigations at the interface of the FRP led to some interesting findings. It was observed that alkali concentrations within the sand surface were generally low. However, as the sand is non-absorptive and the pore water is removed during SEM preparation, it is expected that the interface would contain high pH solution in practice. As well, compaction played a role in alkali concentration approximately 1 mm from the FRP itself (not including the sand coating).

Increasing compaction led to higher alkali concentrations near the interface. This seems to indicate that when an FRP is exposed to either pore solution or directly to cement paste, penetration of alkalis will be observed.

6. Finite Element Model

6.1. Introduction

The development of a numerical model for FRP-reinforced concrete beams with FOS-mounted supplemental bars (FOS-S) attached to main rebars at mid-span (FOS-M) is described in this chapter. The model is developed to study the behaviour of the above system in a beam undergoing flexural deformation under four-point loading. This numerical model will be correlated with the results of the experimental tests conducted on the Control specimen as a part of the present study and that of Torkan (2010). The objective is to calibrate the key parameters in the numerical model such that the model can be utilized for a parametric study to assess the performance of the FOS-S system embedded in FRP-reinforced concrete beams. The performance of the FOS-S system will be governed by the strain captured by an FOS-M as defined by the ratio of strain observed in the supplemental bar to the strain in the main rebar. When the supplemental bar has an appropriate length and is properly bonded to the main rebar and to the concrete, it should capture a strain very close the strain in the main bar.

6.2. Experimental Setup

Figure 6-1 shows the details of the beams specimens used here. Two different sizes of simply-supported beams from the author's experiments and from Torkan (2010) were studied. All the

beam specimens were of normal density concrete tested after the concrete had achieved its design strength. The rollers were inserted at the two ends of the spreader beam to ensure that the concentrated loads are transferred to the beam without moment. The beam samples were instrumented for measuring the vertical deflections at the mid-point of each sample by using two sets of potentiometers. The concrete surface was carefully inspected for cracks as they developed. Testing was terminated when crushing of the concrete occurred and crack width became excessively widened with the loading. The load displacement curves, ultimate load and force-strain were recorded for each specimen. The first experiment (Beam A) as reported in Torkan (2010), contained two beam specimens with (width× height ×length) equal to 250 mm×320 mm×3000 mm (clear span 2400 mm). For Beam A, the diameter of the main rebar is 13 mm and that of the supplemental bar is 6 mm. It is important to note that the diameter chosen for the supplemental bar should be as small as possible, such that the interference caused by the supplemental bar in that section is minimized, thereby allowing the best possible strain capture by the supplemental bar with respect to the main rebar.

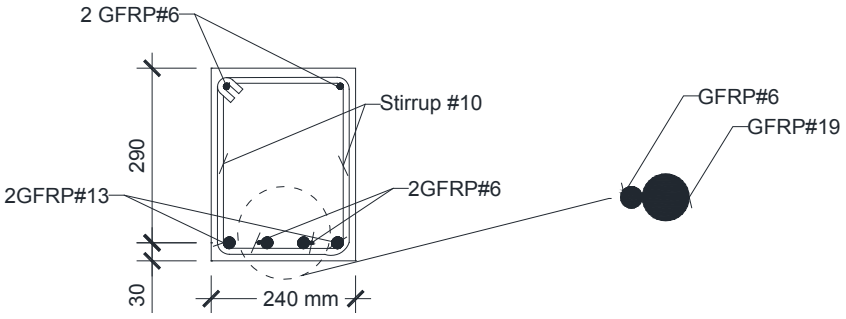

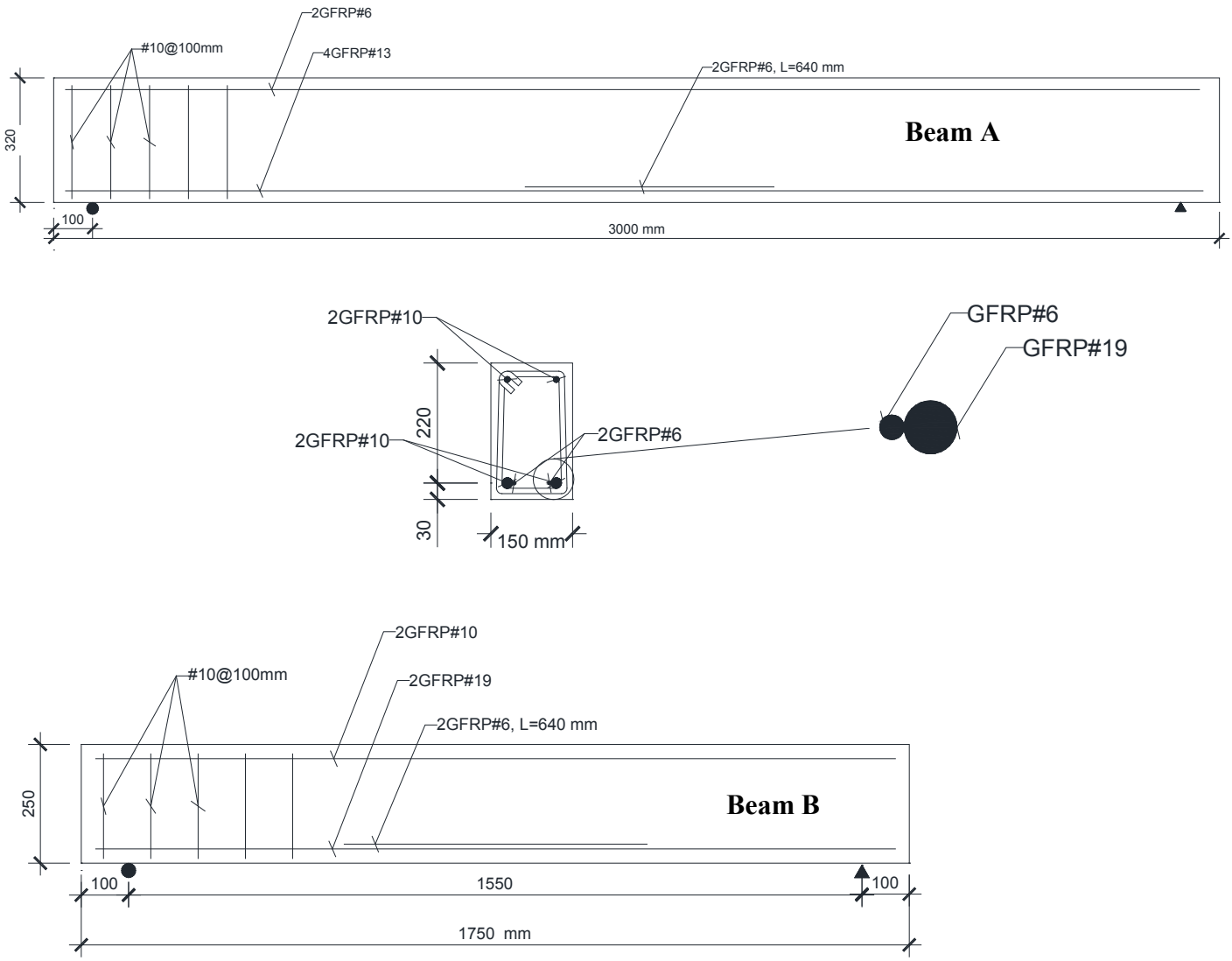

Figure 6-1 Specimen size and reinforcement details of Beam A (Torkan, 2010) & Beam B (current study)

The second sets of beams (Beam B) which are tested in the present study are smaller (150 mm×240 mm×1750 mm) with clear span of 1650 mm. The diameters of the main and supplementary bars are 19 mm and 6 mm, respectively. Both beam types have sufficient shear reinforcement to prevent any shear failure.

6.3. Material Properties and Modeling

For the finite element model developed here, the material characteristics of concrete and of the FRP bars used in the construction of the beam specimens were determined via test and manufacturer's specification (Table 3-1 and Table 4-1). Some mechanical properties from literature were used as detailed in the following sections.

6.3.1. Compressive Behavior of Concrete

All specimens for Beam B were constructed using the same batch of concrete, designed to have a compressive strength of 35 MPa at 28 days. On the other hand, the specimens for Beam A were designed to have a compressive strength of 30 MPa. Concrete cylinders of size 102 × 203 mm were tested in accordance with ASTM C39 to confirm the actual concrete strength, which was 30 MPa for Beam A, 46 MPa for Beam B at 28 days. The concrete cylinders from the same batches of concrete mix as in Beam A and Beam B were also tested at the time when the corresponding beams were tested; and there was no appreciable change in the strength. For modelling purposes, the concrete in compression is considered to be an elasto-plastic and strain-softening material. Its uniaxial compressive stress-strain curve is shown in Figure 6-2. The properties shown in Table 6-1 are used in Equation 6-1 (ISIS, 2007).

Table 6-1 Material properties for Beam B

f_c' (MPa)	n	k	ε_0
From experiment	ISIS, 2007	ISIS, 2007	ISIS, 2007
46	3.51	1.41	2.186e-3

Equation 6-1 $$f_c = f_c' \left[\frac{n\left(\frac{\varepsilon_c}{\varepsilon_0}\right)}{n-1+\left(\frac{\varepsilon_c}{\varepsilon_0}\right)^{nk}}\right]$$

where f_c' is the cylinder compressive strength of concrete in MPa; ε_0 is the strain at which the maximum compressive stress is attained, which is taken from ISIS (2007) as 2.186e-3; and ε_{cu} is the strain at which the concrete reaches crushing, which is taken as 0.003 (ACI-318, 2011).The true strain and stress were calculated using the following definitions:

Equation 6-2 $$\sigma = \sigma_{nom}(1 + \varepsilon_{nom})$$

Equation 6-3 $$\varepsilon = \ln(1 + \varepsilon_{nom})$$

where σ is the true stress, ε is the true strain, σ_{nom} is the nominal stress, and ε_{nom} is the nominal strain.

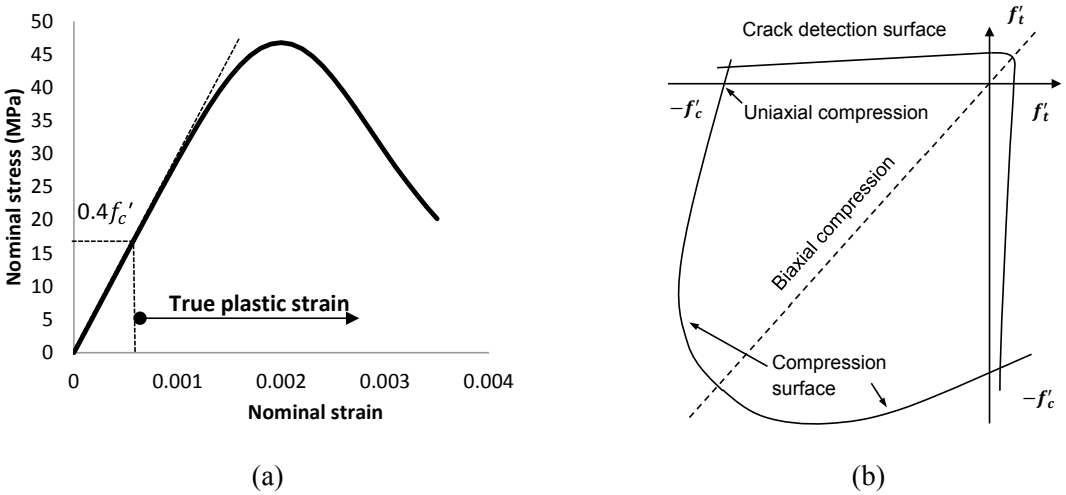

(a) (b)

Figure 6-2 Concrete material model: (a) uni-axial compressive stress-strain; (b) concrete failure surface in plane stress (ABAQUS Analysis User's Manual, 2009)

The Poisson's ratio γ_c of concrete under uniaxial compressive stress ranges from about 0.15–0.22, with a representative value of 0.19 or 0.20 (ASCE, 1982). In this study, the Poisson's ratio of concrete is assumed to be γ_c= 0.20.

6.3.2. Tensile Behaviour of Concrete

The bi-axial stress-strain relationship of concrete both in compression and tension is shown in Figure 6-2. For the model with concrete damage plasticity (CDP), three different tension stiffening formulas have been applied as given in Equations 6-4 to 6-6**.**

Equation 6-4 $f_r = 0.6\lambda\sqrt{f_c'}$ MPa (ACI, 2011a)

Equation 6-5 $f_r = 0.4\sqrt{f_c'}$ MPa (CSA-S6, 2011)

Equation 6-6 $f_r = 0.1f'_c$ MPa (Hassoun & Al-Manaseer, 2012)

f'_c compressive strength of concrete

f_r concrete modulus of rupture

λ concrete density

6.3.3. Modulus of Elasticity of Concrete

The value of the initial modulus of elasticity of concrete, E_c, is related to its compressive strength f'_c and can be calculated using one of the following expressions:

For normal strength concrete (f'_c < 42 MPa)

Equation 6-7 $E_c = 4500\sqrt{f'_c}$ MPa (CSA, 2004)

Equation 6-8 $E_c = 0.043\omega_c^{1.5}\sqrt{f'_c}$ (MPa) or $Ec = 4700\sqrt{f'_c}$ MPa (ACI, 2011)

For concrete strength in the range of $21 < f'_c < 93$ MPa

Equation 6-9 $E_c = 3320\sqrt{f'_c} + 6900$ MPa (ACI, 2011)

6.3.4. Tensile Behavior of FRP Bars

FRP is assumed to behave as an elastic brittle material under tension. The stress-strain relationship for FRP under tension is linear up to its failure. The tensile strength is dependent on the bar diameter. Smaller diameter bars are more efficient (ISIS, 2007). In this model, design tensile strengths of 784, 708, and 656 MPa were used for the bars with diameters of 6, 13, and 19 mm, respectively, based on the manufacturer's specifications (Table 3-1).

6.4. Constitutive Model

The concrete-damaged plasticity model is based on the assumption of scalar (isotropic) damage and is designed for applications in which the concrete is subjected to arbitrary loading conditions, including cyclic loading. The model takes into consideration the degradation of the elastic stiffness induced by plastic straining both under tension and under compression. It also accounts for the stiffness recovery effects under cyclic loading. It is thus suitable to all types of concrete structures. The "Riks" solution procedure (ABAQUS, 2009) and small-time increment are utilized to avoid any instability error. In this model, uniaxial stress-strain material data (Table 6-1) has been used for defining the material properties of concrete. The behavior of FRP is assumed to be elastic and the fracture stress is introduced to the model. The compressive behaviour of concrete is modeled as elasto-plastic; and to define the shape of the failure surface of concrete, the ultimate stress and strain values in uniaxial and biaxial stress states are specified using the failure ratios (ABAQUS, 2009). Based on the suggestion provided in the ABAQUS user's manual, the ratio of the ultimate bi-axial compressive stress to the uniaxial compressive ultimate stress is taken as 1.16. As well, the absolute value of the ratio of uniaxial tensile stress to the uniaxial compressive stress at failure is taken as 0.1.

6.5. Development of the Finite Element Model

The finite element program ABAQUS was used in the present study to perform a failure analysis of the rectangular reinforced concrete beams under four-point bending. One of the following two types of plasticity models can be used in the system: concrete smeared crack (CSC) and concrete damage plasticity (CDP); CDP showed a better result for this model**.** A three-dimensional finite element model with the following characteristics was used.

- Concrete was modelled using the 8-node solid element with reduced-integration (C3D8R);
- FRP bars were modelled using three-dimensional truss elements (T3D2);
- Since the geometry of the beams, loading and boundary conditions were symmetrical, only half of the beam was modeled at the first stage (Figure 6-3);
- Perfect bonds were assumed to exist between the concrete and the top FRP rebars;
- Non-linear axial translational connector elements were used for the bottom FRP rebars and the adjacent concrete to model the bond/slip relationship between the rebar and concrete;

- Non-linear axial translational connector element were used for supplemental FRP rebars; and
- Coupling constraints in all directions were used for the supplemental FRP rebars to the main rebar.

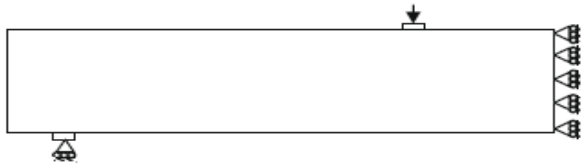

Figure 6-3 Boundary conditions used in the numerical work

6.6. Reinforcement

With this modeling approach, the concrete behavior is considered independently of the rebar. The effects associated with the rebar/concrete interface, such as bond slip and dowel action, were modeled approximately by introducing some “tension stiffening” into the concrete modeling to

simulate load transfer across the cracks through the rebar. In this model, an embedded constraint was applied for the top reinforcement. The nodes of the embedded element (FRP) were laid within the host elements (concrete) such that the translational degrees of freedom at the node are eliminated and the node becomes an "embedded node." For the tensile reinforcement, spring elements are used to simulate the behavior of the interface of the rebar and the concrete.

6.7. Spring Element

Two different force-deflection curves were defined for the connection of FRP to concrete and for connection of the main FRP rebar to the supplemental rebar by using spring elements. In this model, the stiffness of the connection of the supplemental rebar to the main rebar was assumed to be linear for simplification. An axial translational spring connector was applied for this type of spring connector Figure 6-4. In order to have compatible displacements in the other two directions, a coupling constraint was utilized for all the nodes on the main rebar adjacent to concrete and on the supplemental rebar adjacent to the main rebar (Figure 6-5a). A comparison of bond strength in pullout tests showed a wide variation in the results (Davalos et al., 2008). In the beam bending tests, the concrete surrounding the reinforcing bar is under tension, causing cracking at low stresses and hence reducing bond strength despite the confinement provided by the stirrups. The force versus slip relations obtained from similar available tests (Lin & Zhang, 2013) was utilized to calibrate the numerical models developed here. Bond stress distribution is not uniform in the bar and the shear span of the beam has higher stiffness in the spring connection of FRP to adjacent concrete in comparison to the constant moment span of the beam Figure 6-4a). To account for this, the stiffness for the shear span is considered to be almost ten times that of the constant moment span. The properties of the connecting springs between the

supplemental rebar and the main rebar is adjustable based on the results from the experimental study. In this study the strain observed in the supplemental bar is very close to that in the main bar when the connection coupling constraint is applied in the Y and Z directions (Figure 6-5b).

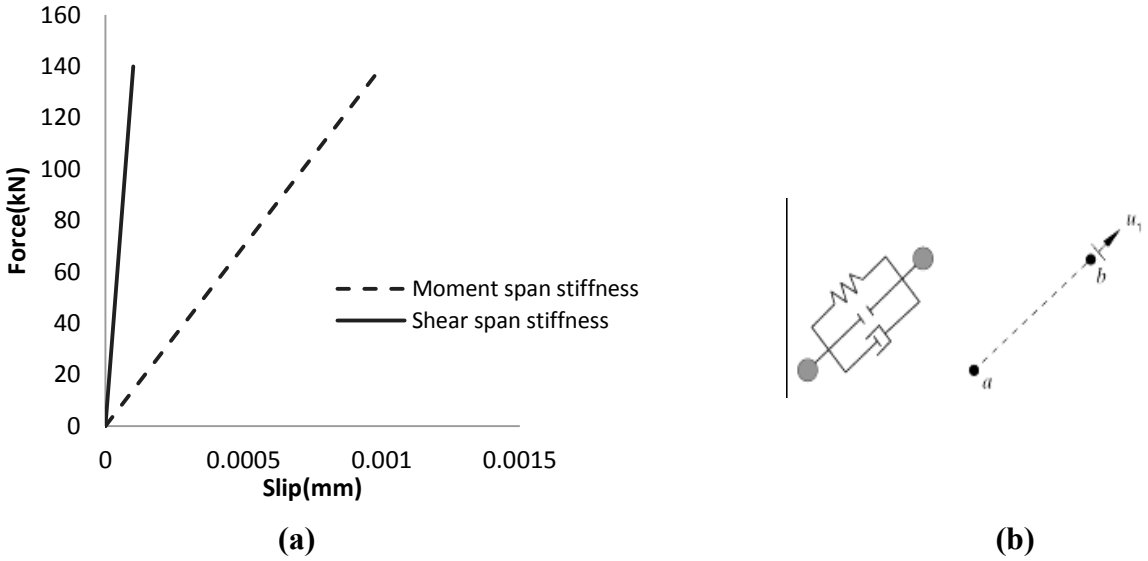

(a) **(b)**

Figure 6-4 Stiffness modeling for the springs: (a) spring stiffness in moment and shear span of the beam; (b) axial translation connector

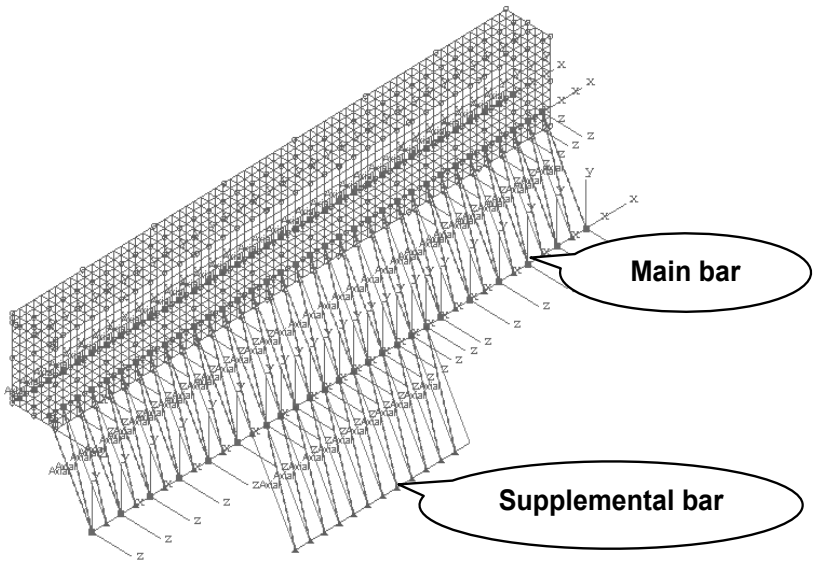

(a)

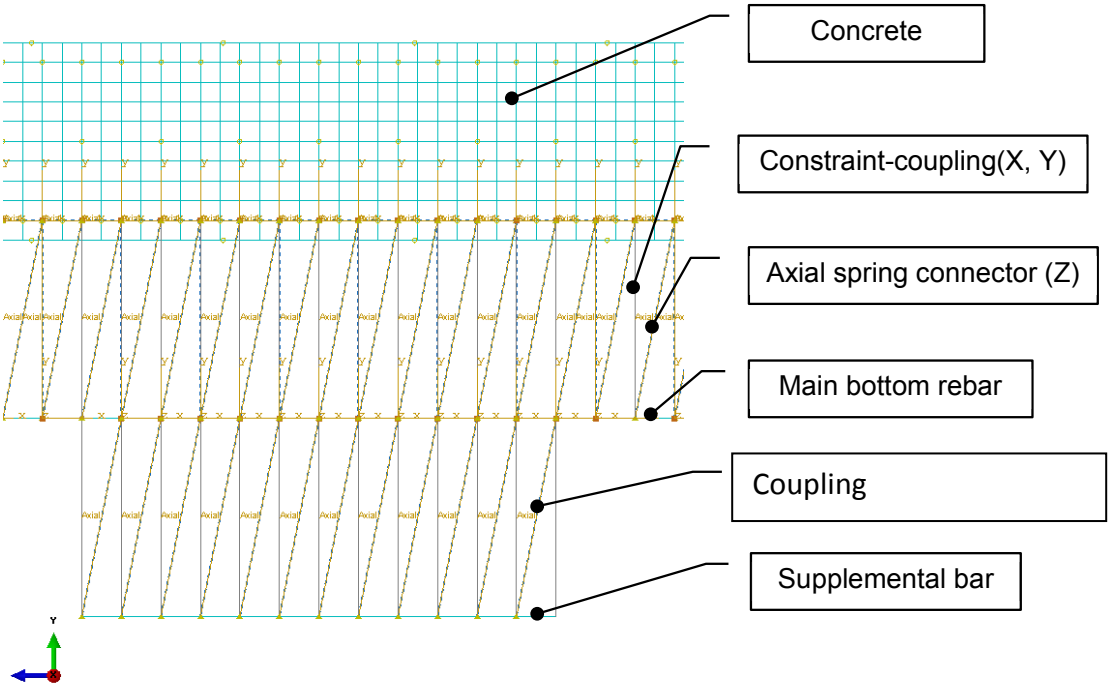

(b)

Figure 6-5 Details of the spring connections: (a) 3D view; (b) 2D view

6.8. Sensitivity Study on the finite element model (Beam B)

Sensitivity studies were carried out on reinforced and unreinforced beams in order to determine a suitable finite element model for the analysis. The load-deflection curves generated using three different meshes involving a total of 840 (Mesh 50), 1620 (Mesh 40), 4020 (Mesh 30), and 6720 (Mesh 25) elements were compared (Figure 6-6) with the experimental results. Based on the results from the above comparison, it is observed that a total of 4020 elements (Mesh 30), including truss elements for the rebars, yields the closest match with the experimental results; that mesh was therefore chosen for the working model of the beams for further study. The size and the number of the FRP elements were defined as the wire elements (Trusses) having equal-sized elements to their adjacent concrete elements so the concrete and truss nodes would coincide with each other and thereby reduce the convergence errors. Figure 6-7 shows a comparison of the unit-less theoretical deflection and the actual deflection in the two beams (A and B) considered here. The load-deflection curve for both the beams follow the same trend as the theoretical curve. The variation of the strain in the supplemental rebar with the applied force is shown in Figure 6-3.. This figure shows the strain in the supplemental rebar according to the experimental data, and from the application of coupling constraints between main and supplemental rebars. The maximum strain measured in an FRP at the loading point (Table 4-3) is about 65% of the ultimate load, which is well below the fracture strain. The beam failed by the crushing of the concrete in compression, and no slip or debonding was observed in the FRP rebars. The numerical model produced similar results.

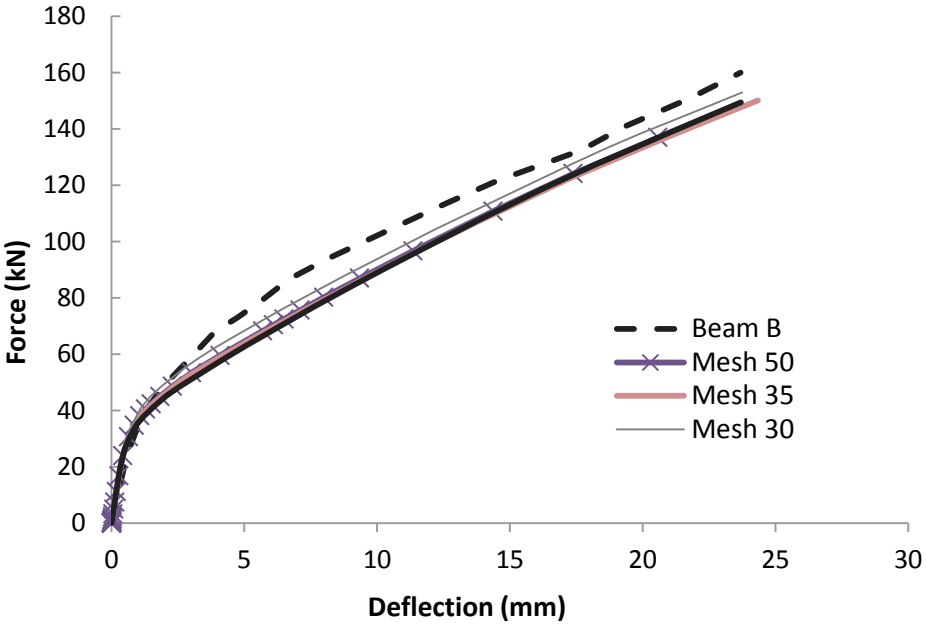

Figure 6-6 Mesh sensitivity analysis – behaviour at mid-span (Beam B)

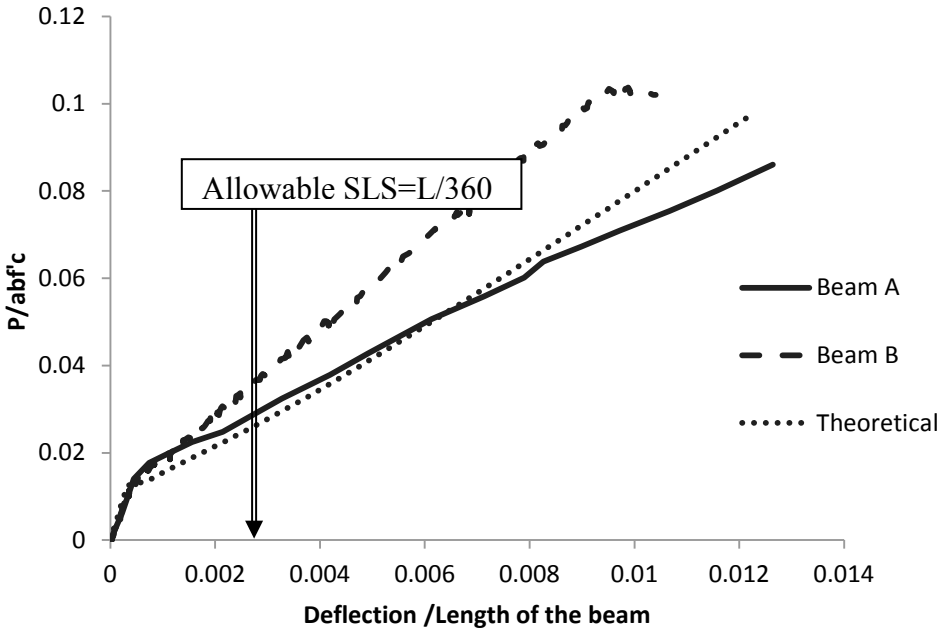

Figure 6-7 Comparison of two beams at mid-span by unit-less P/ab f'_c and Δ /L

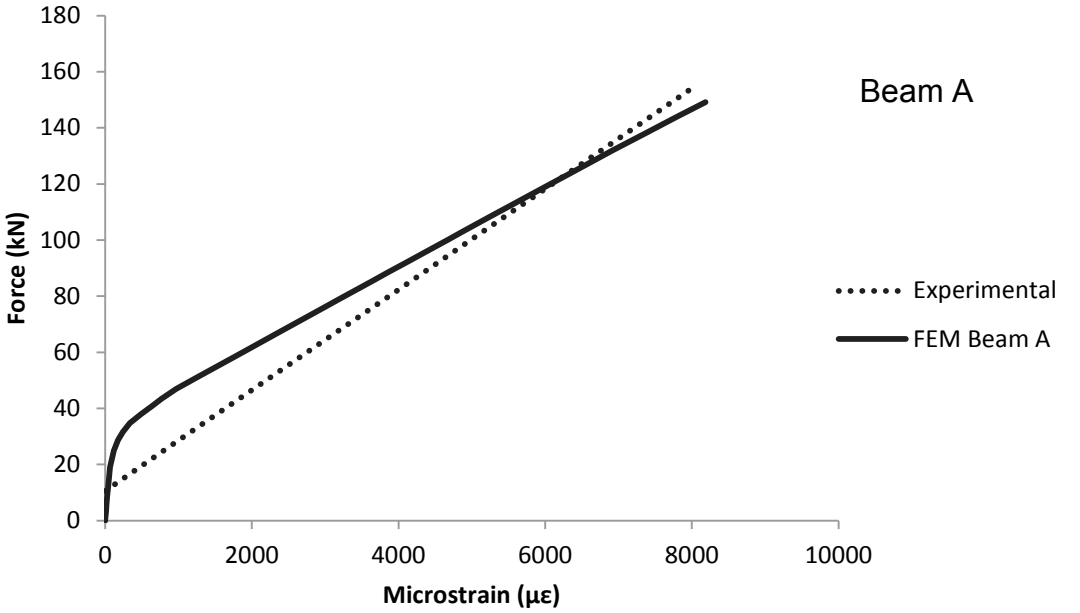

(a)

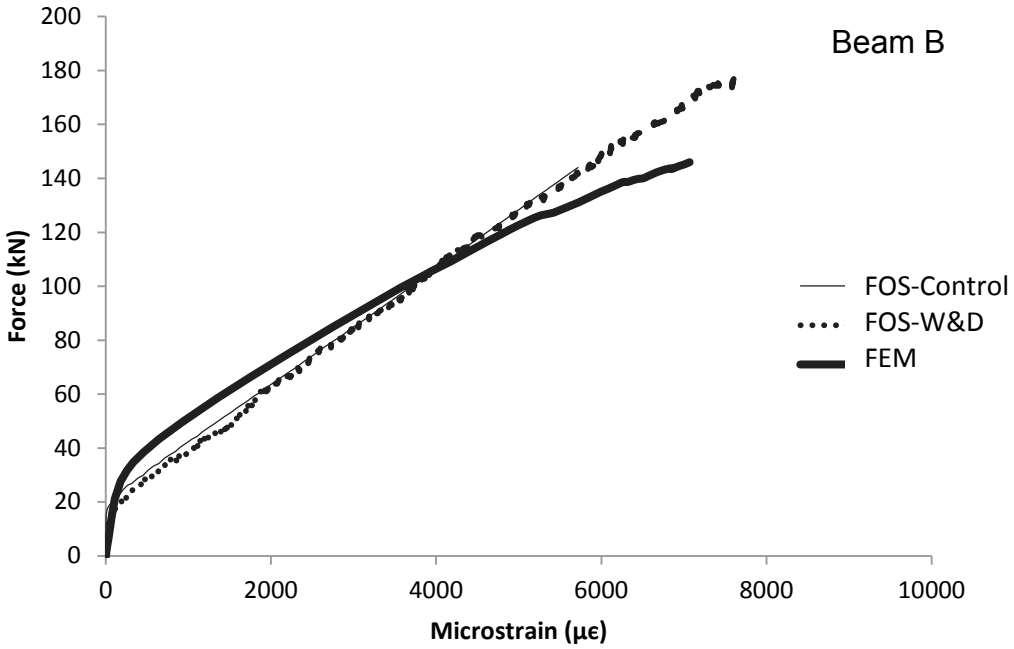

(b)

Figure 6-8 Comparison of results from the experimental and numerical studies: (a) FOS-S in Beam A; (b) FOS-S in Beam B

The developed finite element model, calibrated with the experimental studies of the flexural behavior of FRP-reinforced concrete beams, was used for conducting a parametric study to understand the effect of the key factors, such as the compressive strength of concrete and the tension stiffening effect on the bonds between supplemental bars and the main rebar and with surrounding concrete.

6.8.1. Effect of the compressive strength of concrete on the performance of FOS-S in Beam B

Torkan (2010) conducted a series of tension tests on a number of specimens involving various main rebar and supplemental bar diameters, encased in concrete cylinders. Each specimen contained one supplemental bar which was attached to the main bar by bonding with epoxy and wrapping with Carbon FRP sheets at both ends of the supplemental bar and then encasing the system into a 70 cm concrete cylinder (the main bar projected from both ends). The length of the supplemental bar was twice the development length as determined using CSA S806-12 which is 620 mm for the supplemental bar size of 6. Both ends of the main bar were then pulled apart in a tension test to determine the strain in the main and supplemental bars. The fraction of strain observed in the supplemental bar with respect to the main rebar defines the strain captured by the supplemental bar or by its bond behaviour. The strain captured by the model for the supplemental bars in the tested beams shows results similar to the tension test reported in (Torkan, 2010) in term of similarity of strain in main and supplemental bar. The numerical model of the beams as developed here was calibrated with the experimental tests. The bar sizes and compressive strength of concrete were varied to determine the strain capture in the supplemental bar with respect to the main rebar. Here, the length of the supplemental bar was

maintained at twice the development length ($2L_d$), as recommended in Torkan (2010). The supplemental bar was bonded to the main bar using epoxy and Carbon FRP wraps (CW) at both ends to attain the maximum strain capture.

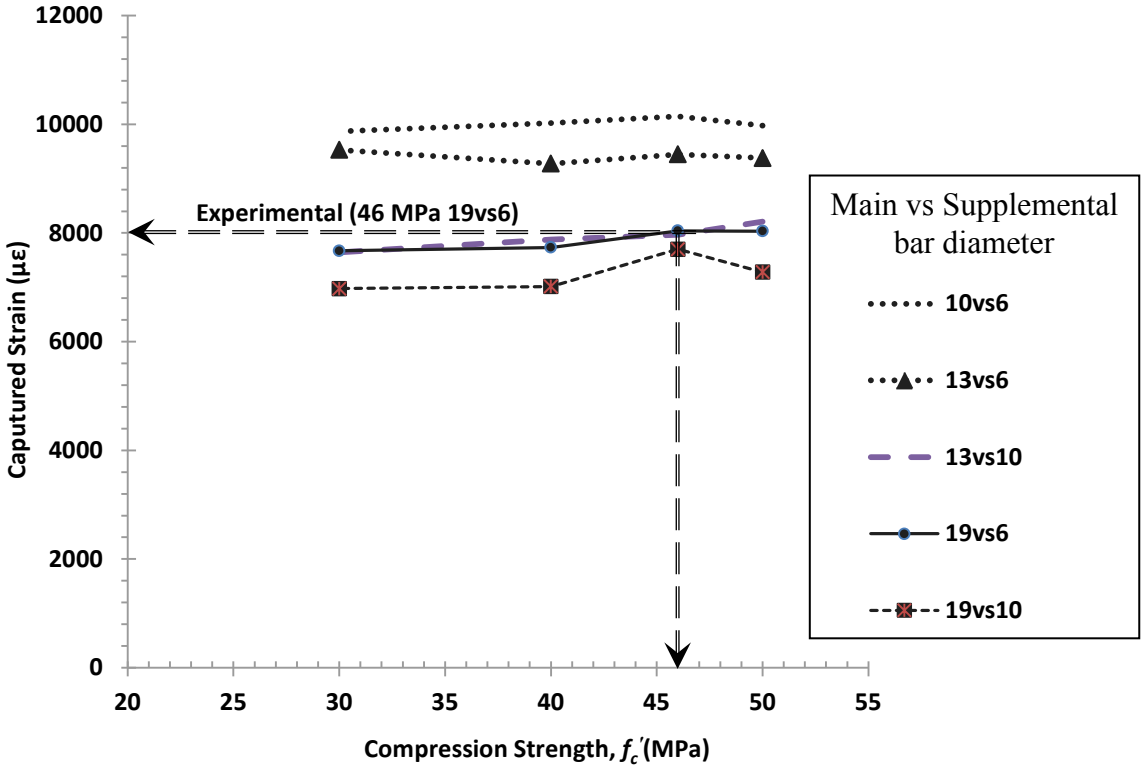

Figure 6-9 Compression strength versus captured strain for varying diameters of main and supplemental bars (Beam B)

Figure 6-9 shows the effect of compressive strength on measured strain for different bar diameters. In the figure, the notation 19vs6 indicates the size of the main bar versus the supplemental bar, in millimeters. It is observed that a change in the concrete compressive strength has no significant effect on the captured strain. It is observed that 19vs6, 19vs10 and 13vs10 mm bars produce the strain captured by the supplemental bar, which are closest to the

experimental results. The other diameters, 13vs6 and 10vs6 mm, show higher strain because of the higher equivalent area of rebar sections, which agree with diameter sensitivity.

6.8.2. Effect of Tension Stiffening on the Rebar Strain

Different upper and lower ranges of tensile strength of concrete (T_y) were used to derive the strain in FRP rebars for an evaluation of their sensitivity. The tensile strength of concrete as defined by in Equations 6-4 to 6-6 was used in the numerical model to determine the strain in the rebar. Figure 6-10 shows the variation of the rebar strain with respect to different values of tensile strength in concrete for a set of different concrete compressive strengths. Each curve in Figure 6-10 is defined using different points which correspond to the tensile strength of concrete calculated using the three different expressions given by Equations 6-4 to 6-6. From Figures 6-9 and 6-10, it is observed that using the peak strain response as obtained in the experimental study (i.e., 8000 με), the numerical model gives similar response with the application of different tension stiffening formulae and concrete strength in the range of 25-50 MPa.

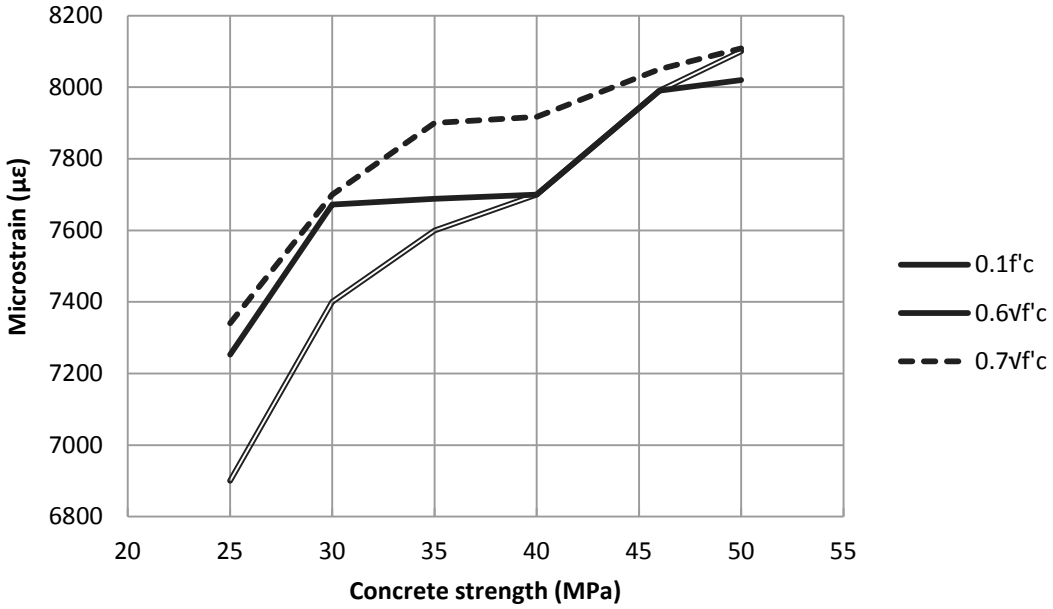

Figure 6-10 Concrete tensile strength effect in captured strain (Beam B)

6.9. Strain in the Compression Zone

The top part of a beam between the two concentrated loads had a stress distribution in the concrete beam as shown in Figure 6-11. The maximum compressive stress in the top rebar reached 261MPa, while it was constrained entirely by the adjacent concrete. FRP has negligible compressive strength and no buckling could occur because of confinement in concrete. When the concrete in the region between the load points crushed, the FRP bars in compression got partially detached from the concrete and the effect of confinement was reduced. In that case, the compressive block of concrete moved upwards and the FRP bars in that region would experience bending or buckling (Figure 6-11 and Figure 6-13). The ESG strain in the top rebars is shown in Figure 6-14, which it indicates that after an initial phase of compression, the top rebars

experience tensile stress in all samples in which the readings from the ESGs on these bars were available. The modes of failure for FRP bars under compression may include transverse tensile failure, fiber micro-buckling, or shear failure followed by micro-buckling of the fibers. Failure of the compression rebars is also influenced by the type of resin, the fiber-volume fraction, and the ambient condition. The compressive stress of 261 MPa is measured for the top FRP bar which is almost 36% of the ultimate tensile strength of FRP.

For further investigation, two of the failed beams from Imm and W&D were re-loaded and the results are shown in Figure 6-15. As submerging the beams in alkaline solution did not reach the top cover of the beam these ESG sensors were still reliable. In that case, there was no connection between the compression area of the concrete block on the top and the top rebar, so that the whole top rebar is under compression as expected in flexural beam behavior.

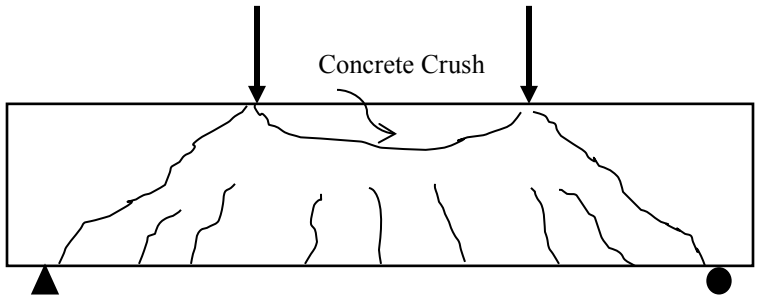

Figure 6-11 Compression crush area

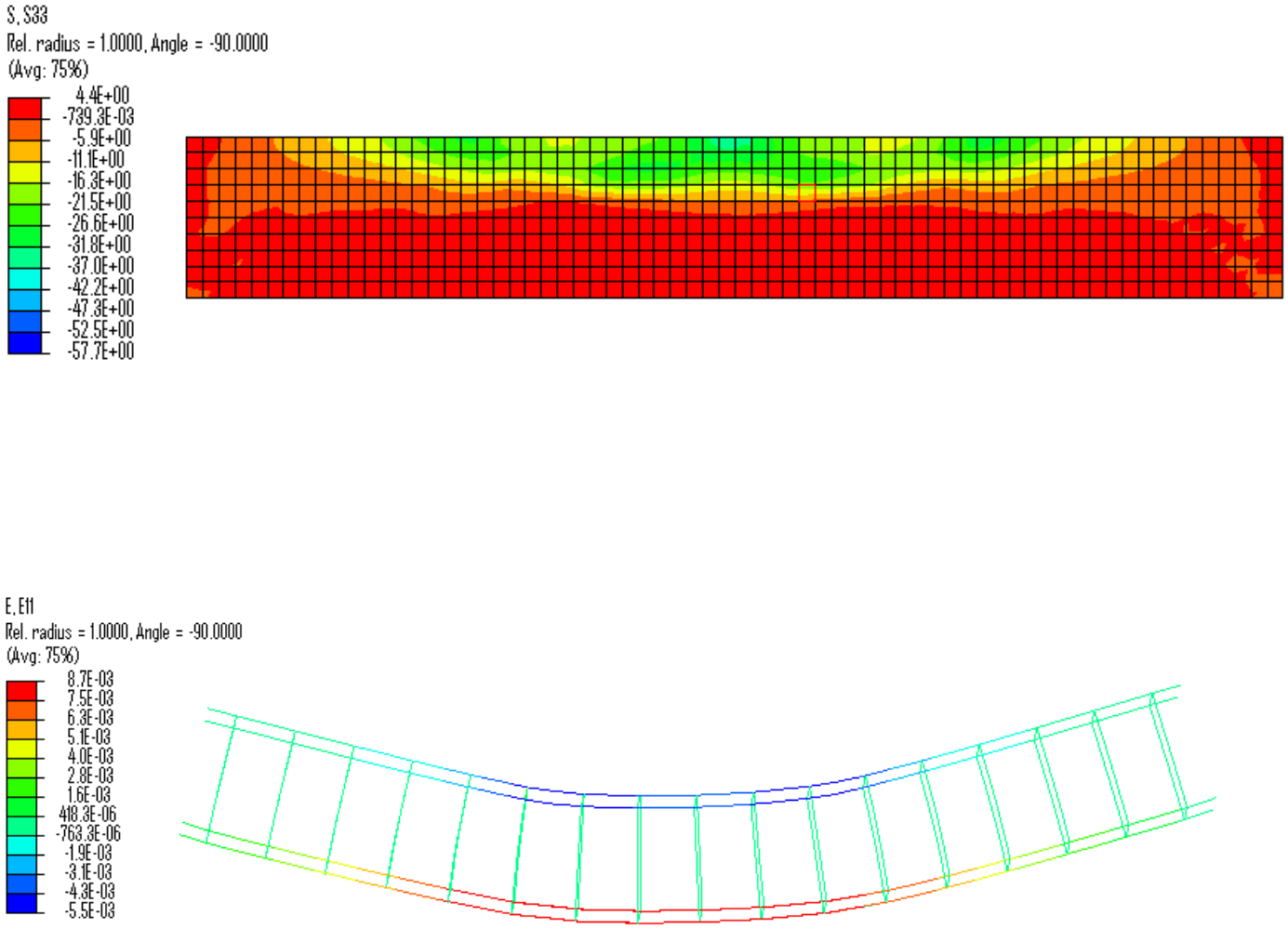

Figure 6-12 Stresses in concrete (top) and FRP (bottom)

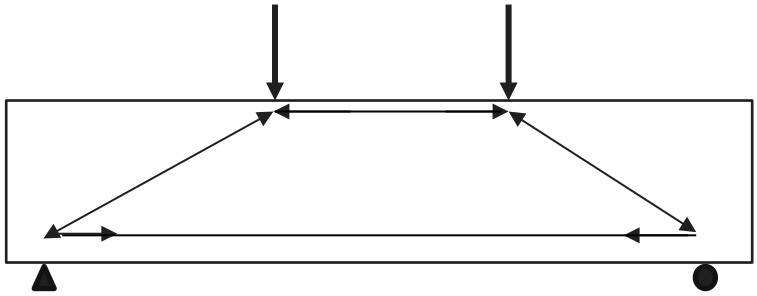

a) Deep beam Strut-Tie model (STM)

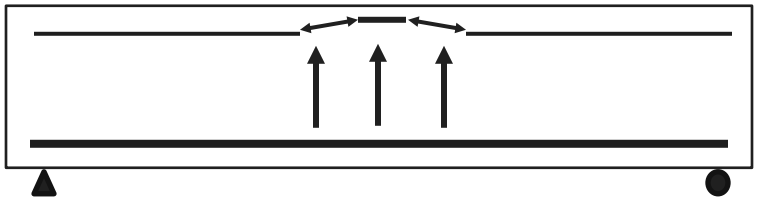

b) Ultimate stress stage

Figure 6-13 Compressive block reaction

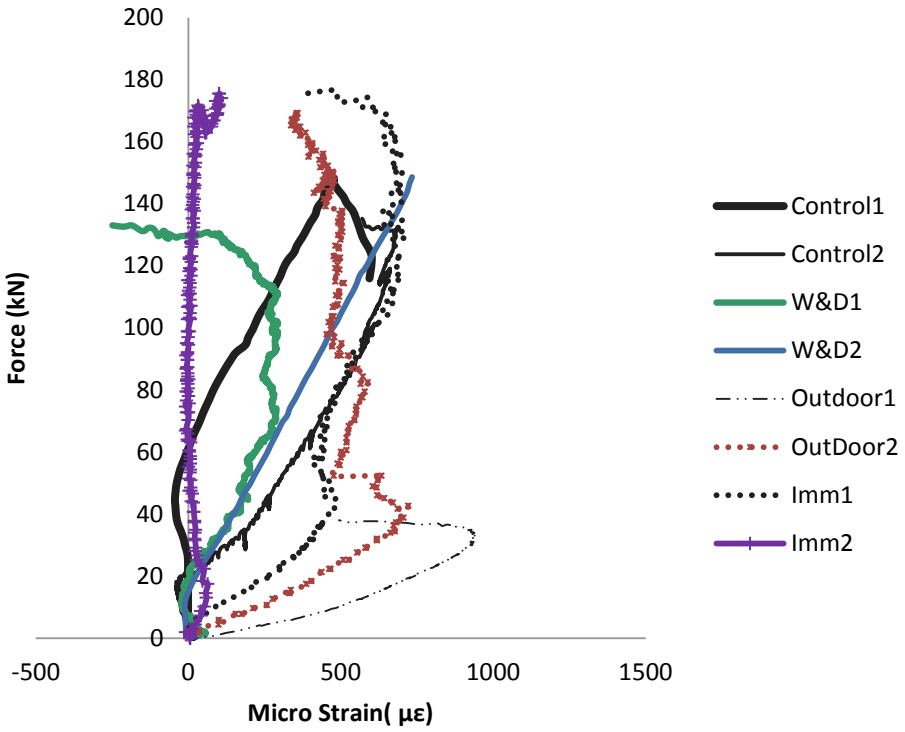

Figure 6-14 Strain at top rebar under compression in all conditions

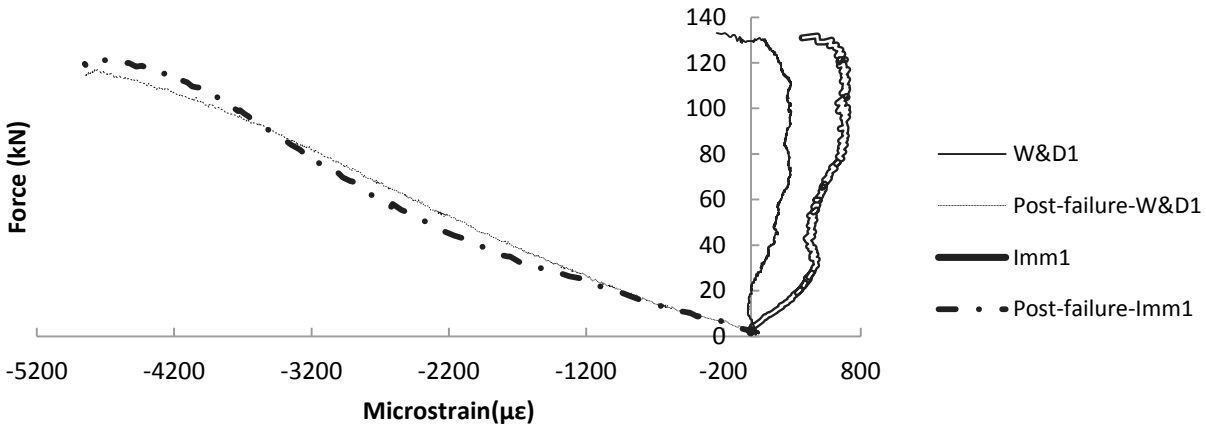

Figure 6-15 Top rebar under W&D and Imm condition (Post-failure)

6.10. Discussion

Finite element modeling of FRP-reinforced concrete beams under static loads is presented in this chapter. The nonlinear behavior of beams has been studied with respect to two different experimental studies. The software package ABAQUS was employed in the analysis. The load-deflection curves, load-strain, and ultimate strength values were obtained from the finite element analysis. The results were compared to the corresponding results obtained from the experimental studies. In addition, the finite element method provides extensive information on the behavior of these beams up to failure.

Application of the finite element analysis provide a detailed picture of the complete behavior of a beam from its elastic properties to the cracking of concrete and its plastic behavior up to ultimate load. Deflection of the mid-span point and failure load and strain of FRP bars are discussed here. It is observed that the finite element predictions for beam deflection and FRP strains are in close agreement with the corresponding experimental results. Based on experimental tests, the supplemental rebar and main rebar are provided with appropriate constraints to simulate the strain capture by FOS-Ss comparable to that observed in the experimental tests.

Correct modeling, especially in concrete, is essential for ensuring the accuracy and numerical prediction of the behaviour of the types of beams studied here. The friction between the FRP bars and the concrete, as well as the tension stiffening are sensitive factors which should be considered in analysis.

7. Fatigue and Post-Fatigue Test Results

7.1. Introduction

Structures such as bridges are subjected to cyclic loads due to moving vehicles. Simulation of the actual behaviour of such structures may be quite difficult due to the complex nature of the load cycles. It is time consuming and difficult to model an accurate prototype for comparative purposes. However, researchers often simplify load cycles in order to capture the fundamental behaviour of a structure under fatigue. Fatigue loading may be of variable magnitude and frequency. A simplified model application of constant magnitude and pattern can be helpful to define the ultimate load capacity at critical loading. This chapter presents the results of the experimental study on FRP-RC beams subjected to cyclic loading with constant amplitude. The performance of the FOS and ESG sensors under such loading and various environmental conditions was studied and presented here along with the analysis of the behaviour of the FRP-RC beam specimens, their serviceability limit states, and ultimate capacities.

The loading setup (Figure 3-13) and cyclic loading protocol (Figure 3-16) for fatigue tests have been described in Chapter 3. The loading was such that the stress in FRP bars was tension-tension; and it was sinusoidal loading with 2 Hz frequency. The minimum stress, σ_{min}, as defined in

Equation 7-1 represents the effect of superimposed loads on a bridge (pavement, installation etc.), and the maximum stress, σ_{max} is close to 80-90 percent of the ultimate capacity.

Equation 7-1 $$\sigma_{mean} = \frac{\sigma_{min}+\sigma_{max}}{2}$$

The data from the actuator and the strain from the data acquisition system (Strain Smart 5000) were acquired at 2 Hz. The response quantities (i.e., strain, deflection, etc.) for one complete loading-unloading cycle were recorded in order to check the crack width and the change in deflection at every 50,000 or 100,000 cycles up to 1 million cycles, which is discussed later in this chapter

7.2. Flexural Toughness and Capacity

Fracture energy (flexural toughness) is an important parameter influencing the structural strength and ductility. In FRP-RC, flexural toughness is a convenient parameter for comparing the absorbed energy and resistance to fracture; but there are some uncertainties about the manner in which it should be measured, interpreted and used (Lianrong et al, 1994). The factors include the rate of loading, size and geometry of the specimen, loading configuration, stiffness of the machine, and the method of interpretation. The flexural stiffness can be expressed either by dimensionless indices as described in ASTM-C1018 (ASTM International, 2003a) which considers the effect of geometry, or by JSCE-SF4 (JSCE, 1984) which considers the absolute value of toughness as independent of geometric effect. In the standard test method for determining the flexural toughness in ASTM C1018-03, the area under the load-deflection curve

up to a specified deflection criterion is divided by the area up to the deflection at which first crack is deemed to have occurred. As defining the deflection of the first crack is difficult and controversial, this method was removed from the standard in 2006 due to lack of interest and accuracy. However, in the present work, the following modifications were considered to calculate the flexural toughness as a ratio of the dissipated energy at the serviceability limit to that at the ultimate load level. This could be used for comparing the effect of different conditions on reliability and disaster prevention in severe loading, creep, earthquake, and stress relaxation when the structure passes the allowable deflection limit in such a conditions. In this calculation, the crack size and numbers are not calculated. The serviceability limit and ultimate load caring capacity are used as the determinant factors such that the specimens under fatigue which are already cracked, this definition will still be applicable.

Equation 7-2 $$I = I_{ult}/I_{all}$$

where, I is the flexural toughness index, I_{ult} is the area under the force-deflection up to the ultimate load, A_{ult} (area enclosed by OBC in Figure 7-1), and I_{all} is the area under force-deflection up to the allowable deflection, A_{all} (area enclosed by OAD in Figure 7-1) for serviceability (Figure 7-1).

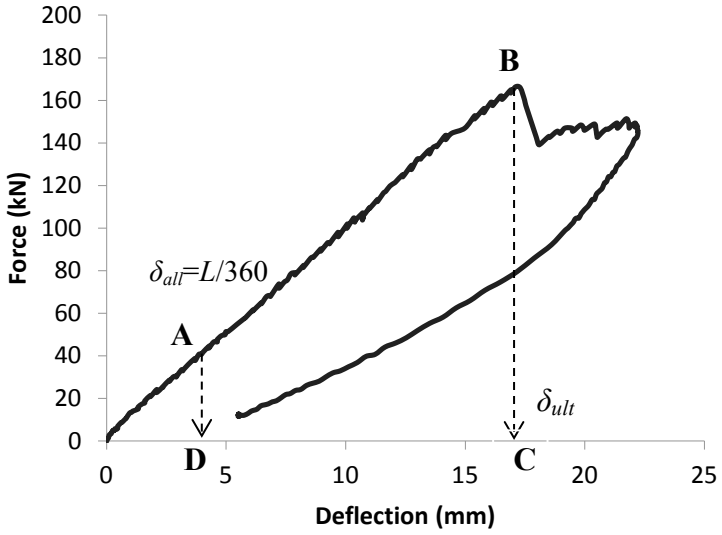

Figure 7-1 Calculation of flexural toughness

Table 7-1 Flexural toughness index

Condition	***I***	P_{ult} **(kN)**	Δ_{ult} **(mm)**
Control1	8.61	181	15.78
Outdoor1	15.92	176	19.41
Outdoor2	14.45	168	19.73
W&D1	18.94	178	19.00
W&D2	12.1	166	16.90
Imm1	9.12	176	17.00
Imm2	18.45	175	21.43
Controlf	13.17	177	20.70
Immf	13.93	209	18.14
W&Df	17.31	151	18.73
Outdoorf	15.42	192	17.00

It is observed that in spite of the highest ultimate load capacity for Control1, the toughness index is found to be the lowest (I=8.61). This conclusion is also valid for Controlf with the maximum deflection at the ultimate load (among the specimens undergone fatigue load cycles), while producing the minimum toughness index (I=13.17). It can be concluded that the control condition has the least toughness index based on the present assumptions. Imm1 and Imm2 specimens show widely different values of the toughness index (9.12 and 18.45, respectively), perhaps due to their different failure modes. The immersion specimen, Immf subjected to fatigue load cycles, shows a low value of the toughness index (13.93), as well. The variation in the toughness index for W&D1 and W&D2 is also noticeable, while the Outdoor specimens have similar values of the toughness index for static and fatigue samples. From Table 7-1, the weathering conditions appear to improve the toughness index and energy absorption capacity, but in the cases of alkaline exposure, the degree of improvement shows a higher variability. While all the specimens were identical in size, materials and reinforcement details, there is potential variability in materials properties, reinforcement placements, exact location of supports and loading, weathering conditions etc. Since only a limited number of specimens were tested, it is difficult to quantify the effect of the variability in different parameters and its influence to the results. However, the effect of the variability is clearly observed in the results such as the ultimate capacity, deflection and flexural toughness (Tables 7-1). Similar variability is also observed in the other parameters such as the crack width and failure modes as discussed later.

Table 7-2 shows a comparison of the nominal flexural strength of each specimen with experimentally-obtained ultimate strength. The calculation of the nominal strength depends on the value of f_c'. As mentioned earlier, the results of the cylinder tests show that the value of f_c' changes with each condition, and so the flexural strength has been recalculated using the specific value of the concrete strength.

Table 7-2 Flexural strength of the tested beams (theoretical and experimental)

	Beam ID	$f_c^{'}$ (MPa)	$\mathbf{M}_{Nominal}$ (kN.m)	$\mathbf{M}_{exp}$(kN. m)	$\frac{\mathbf{M}_{exp}}{\mathbf{M}_{Nominal}}$
Immersion	Imm1	47	52.8	48.1	91%
	Imm2	55	56.9	46.7	82%
	Immf	55	56.9	55	97%
W&D	W&D1	49	53.9	46.7	87%
	W&D2	55	56.9	44.5	78%
	W&Df	55	56.9	39	68%
Outdoor	Outdoor1	46	52.2	46.7	89%
	Outdoor2	46	52.2	45.6	87%
	Outdoorf	46	52.2	49.7	95%
Control	Control1	46	52.2	49.7	95%
	Controlf	46	52.2	46.2	89%

For flexural failure induced by crushing of concrete without rupture of FRP, the strain at the top fiber is equal to 0.0035 in concrete, and α, β are as defined for a balanced section (Canadian Standards Association, 2011). The nominal moment will therefore be derived from the following equations:

Equation 7-2 $$f_{frp} = 0.5E_{frp}\epsilon_{cu}\left[\left(1+\frac{4\alpha\beta f_c'}{\rho_{frp}E_{frp}\epsilon_{cu}}\right)^{0.5}-1\right]$$

Equation 7-3 $$\rho_{frp} = \frac{A_{frp}}{bd}$$

Equation 7-4 $$T = A_{frp}f_{frp}$$

Equation 7-5 $$M_n = T(d-\frac{\beta c}{2})$$

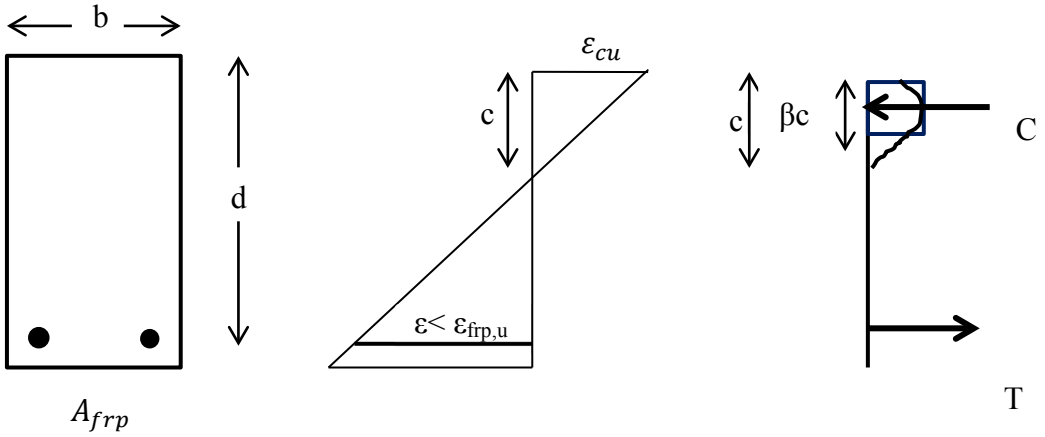

Figure 7-2 Strain and stress distribution at the ultimate test (concrete crushing)

Table 7-3 Actual flexural strength from fatigue tests, as a percentage of the nominal strength (λ)

Condition	$\mathbf{M_{exp}/M_{Nominal}}$	$\boldsymbol{M_{exp}/M_r}$
Controlf	88%	200%
W&Df	69%	169%
Outdoorf	95%	212%
Immf	97%	238%

In Table 7-3, the maximum degradation is observed to be in the case of W&Df (69%), which had a balanced failure mode with concrete crushing followed by the fracture of the FRP tensile reinforcements. The degree of degradation is more due to the conditioning (alkaline

environment) of the specimen than to fatigue. Fatigue degradation in the Immf and Outdoorf beams is almost negligible. It can be seen that the cracks due to cyclic loading do not go through the compressive block of the beam (Figure 7-3) with the level of loading, as mentioned above. As long as the interlocking friction and the bond between the aggregates and the cementious materials exist, the core of the compressive block resists the load and the beam will survive fatigue load cycles. The only matter of concern in these cases is the increase in the magnitude of the deflection under fatigue, which may pass the serviceability limit.

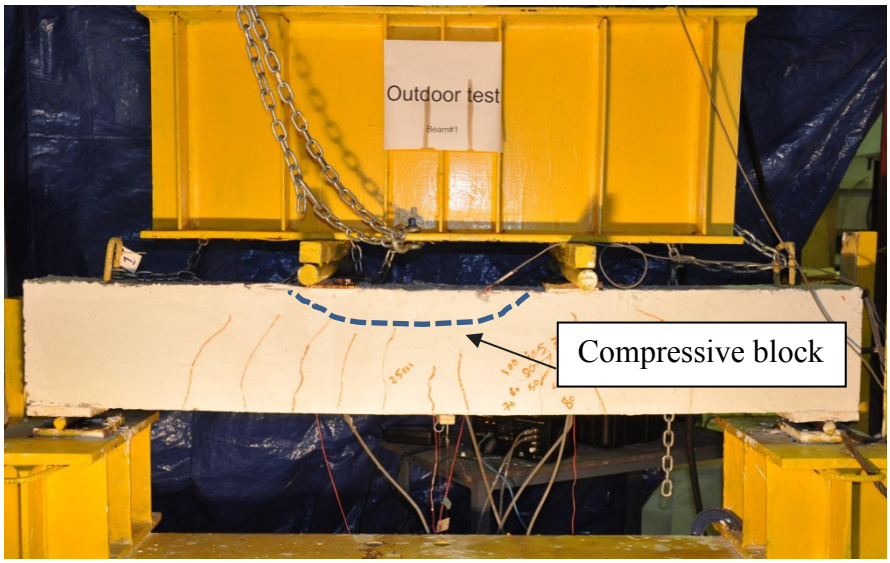

Figure 7-3 Compressive block

7.3. Deflection

The maximum deflection (δ_{exp}) corresponding to the failure load is measured and compared with that computed using the deflection limit suggested in ISIS (2007) which is denoted here by δ_{code}, as explained in Appendix A where the effective moment of inertia, I_e given by Equation (B10)

can be applied. Table 7-4 shows the displacement ratios ($\delta_{exp}/\delta_{code}$) for all the specimens. The experimental displacement in the specimen with the W&D condition was found to deviate the most from the allowable maximum displacement, δ_{code} as compared that in the Control specimen.

Table 7-4 Ratios of the experimental to alloawable displacements ($\delta_{exp}/\ \delta_{code}$)

Condition	$\boldsymbol{\delta_{exp}/\ \delta_{code}}$
Immf	92%
W&Df	158%
Outdoorf	96%
Controlf	109%

Figure 7-4 to Figure 7-7 show the force-deflection curves for post-fatigue static load tests. In these figures, the solid-line indicates the load-deflection relation after one million cycles of fatigue loading. The dashed lines in Figure 7-4 to Figure 7-7 indicate the force-deflection curves of first cycle loading under a load corresponding to σ_{mean} as given by Eq. 7-1. In all conditions, the ascending parts of these two curves are parallel to each other. This behavior shows a robust load carrying capacity of FRP-RC beams in all conditions under fatigue, up to the ultimate loading capacity.

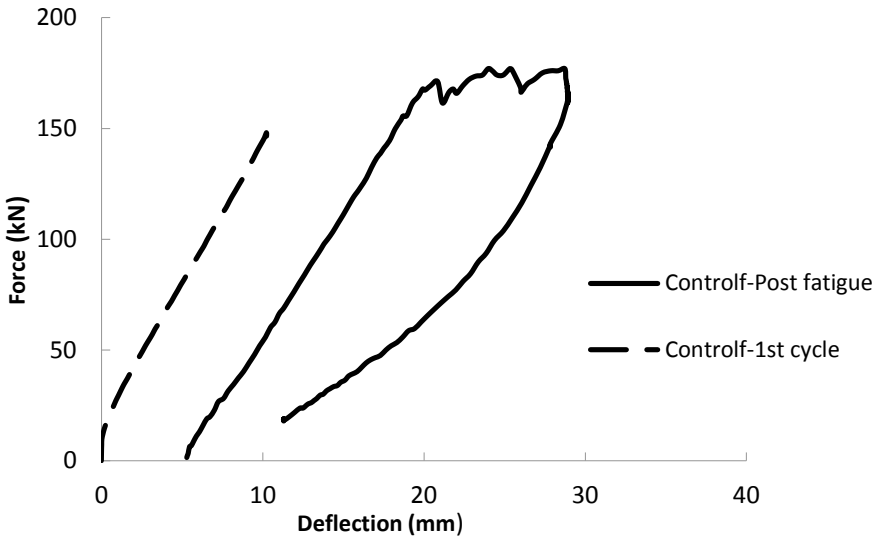

Figure 7-4 Effect of fatigue in Control condition

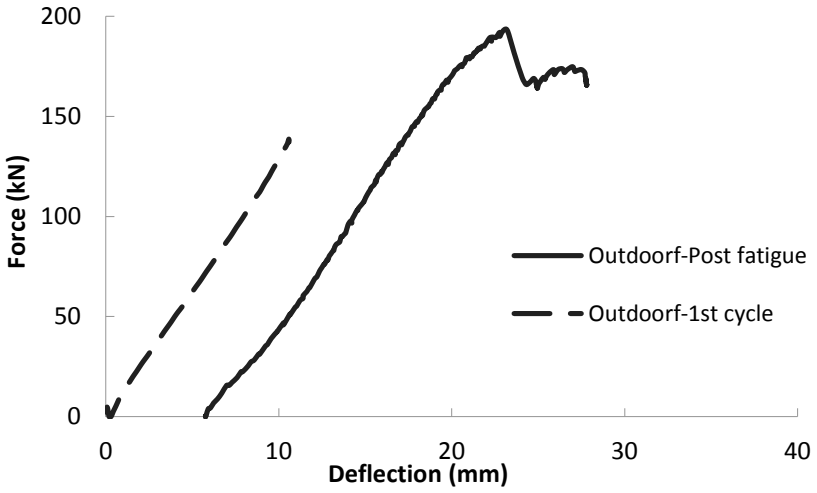

Figure 7-5 Effect of fatigue under outdoor conditions

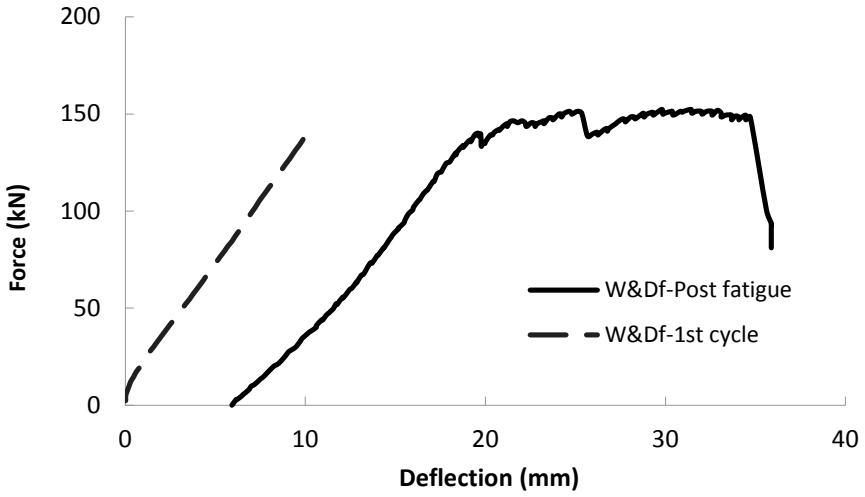

Figure 7-6 Effect of fatigue under W&D conditions

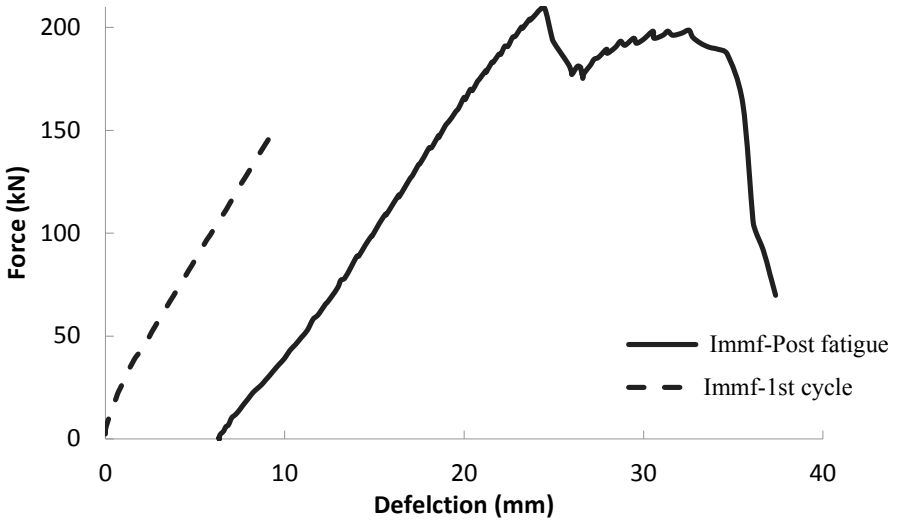

Figure 7-7 Effect of fatigue after Immersion conditions

7.4. FOS Strain Analysis

7.4.1. Overall Behavior

Figure 7-8 to Figure 7-11 show the strain recorded using the FOS sensors in the main and supplemental bars. The figures show a good agreement of the strains in the main bars (identified in the legend with suffix "-M") and in the supplemental bars (identified in the legend with suffix "-S") in Control, Outdoor and W&D specimens before applying the fatigue laod cycles and after one million load cycles. The range of the strain values and slope at every cycle follows the same pattern as observed in the case of static loads for Control and Outdoor conditions (Figure 7-8 and 7-9). The strain response of the main and supplemental bar in the W&Df specimen are shown in Figure 7-10. In this case, two different types of FOS were used to compare the behavior of FOSs under that conditioning: FOS-S1, the sensor mounted on the proposed supplemental bar of the design length as used in all other specimens; and FOS-S2, a commercially available sensor-mounted FRP bar of a fixed length of 400 mm and with a groove where the sensor is mounted. However, in the case of Immersion, the performance of the sensors was found to be the worst (Figure 7-11), as none of the sensors worked properly. The alkaline environment had adversely affected the FOS sensors. The high level of pH and penetration of the alkaline solution affected the epoxy or even the fiber itself. The results show that both sensors performed very well in fatigue loading in case of the specimen with W&D condition.

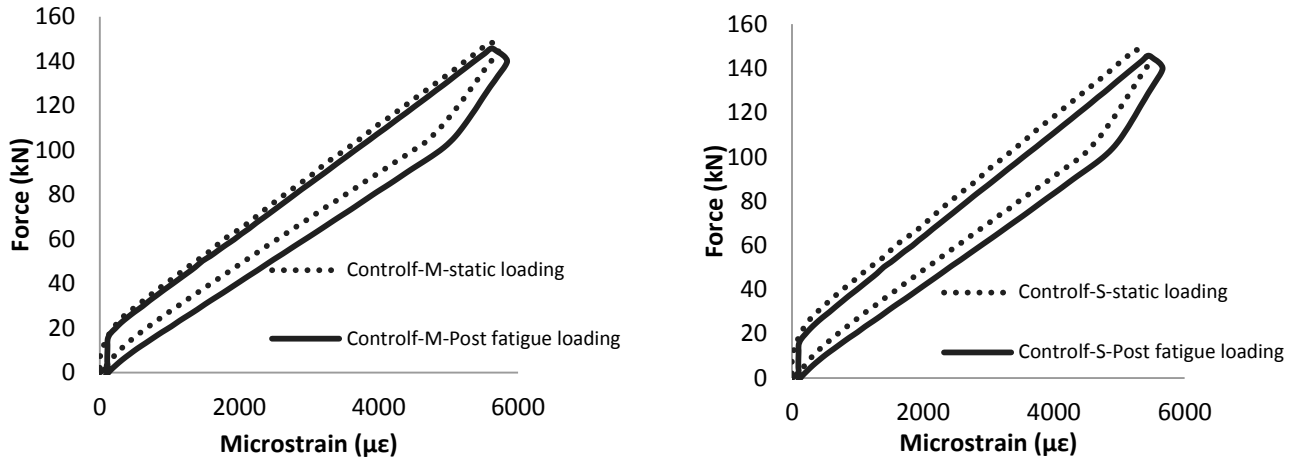

Figure 7-8 FOS readings in the Controlf

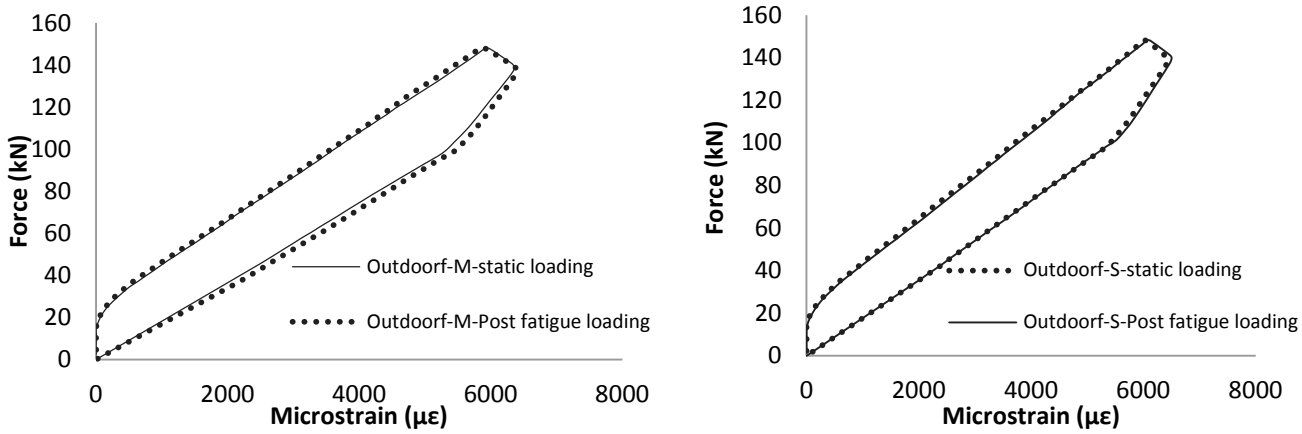

Figure 7-9 FOS readings in the Outdoorf

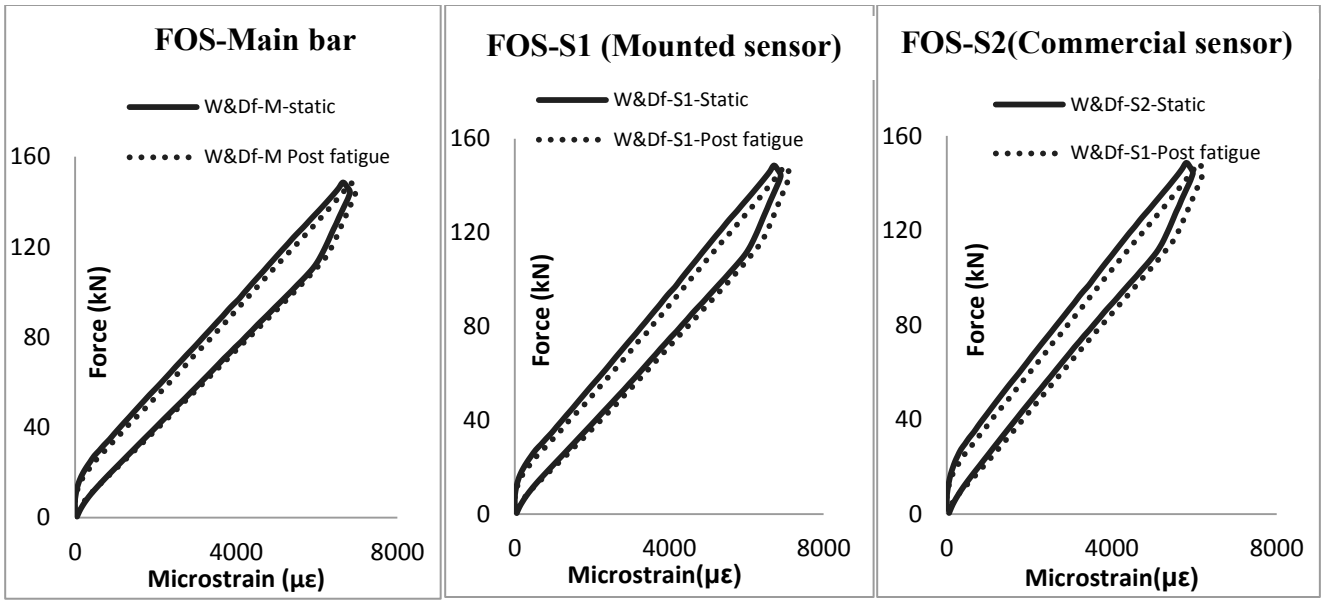

Figure 7-10 FOS readings in the W&Df specimen

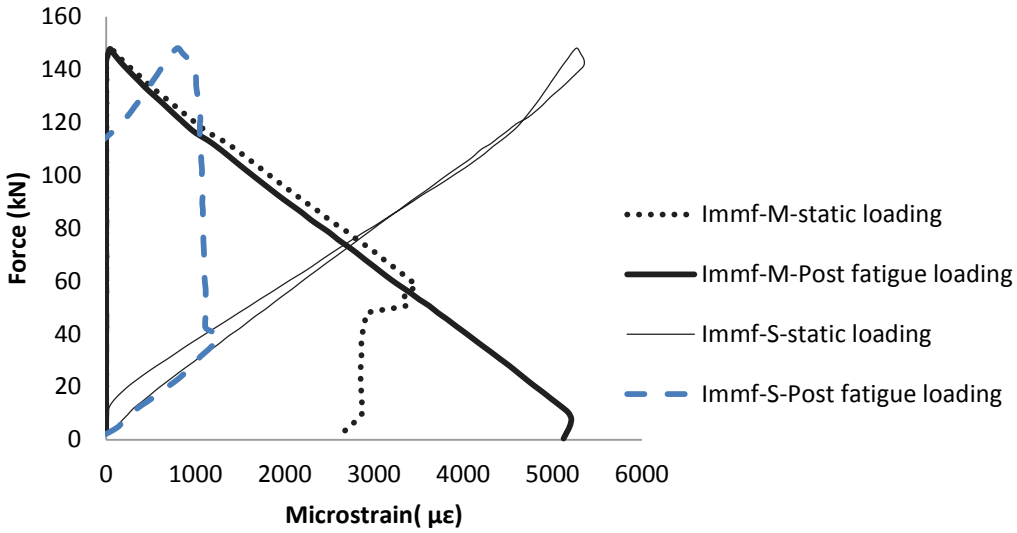

Figure 7-11 FOS readings in the Immf

7.4.2. Detailed Analysis of the Experimental Results

Figure 7-12 to Figure 7-15 show the force-strain performance of the beams subjected to different conditioning. It should be noted that for the Outdoor conditioned specimens, the lead wires of some of the sensors were damaged during handling during transportation of the specimens to their outdoor location. With the immersion specimens, the FOS sensors did not work properly due to the penetration of the alkaline solution. The problem was diagnosed by a fiber optic sensor expert as damage to internal connections, attributable to the penetration of alkaline solution which affected the bonding mechanism of the FOS to the rebar. The SEM results from Chapter 5 show the diffusion of alkaline solution inside the FRP bars and near the sensor locations. Load cells used in the fatigue and static tests are of different type and accuracy; consequently, there is some difference in the slope of the F-ε curve at the low loading rate. In the cases of W&D2 (Figure 7-14), the strain reading abruptly jumped as a result of an improper installation of the sensor, as shown in Figure 4-15.

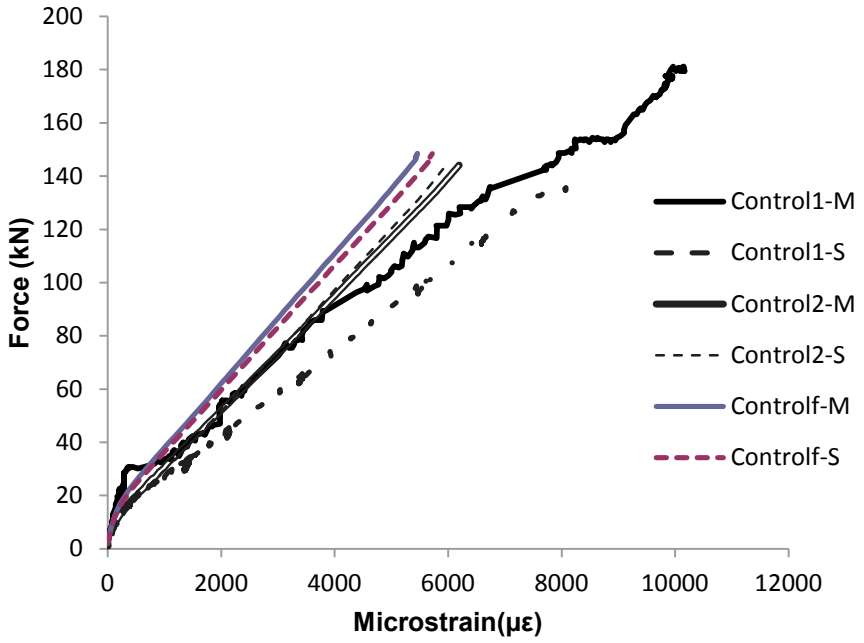

Figure 7-12 Initial Force-strain relations for the FOS in Control specimens in static and fatigue tests

Figure 7-12 shows the applied load vs. strain in the FRP reinforcing bars (bottom) the Control specimens. The initial cycle of loading in the Control specimen used for the fatigue test was used in Fig 7-12 to compare with the results of the Control specimen used in static test. The results shown in the figure indicates that the post-cracking slope of the load-strain curve increases with the magnitude of the fatigue load as compared to the static loading condition. In other words, the strain measured at the same level of load is decreased as a result of fatigue and the magnitude of the fatigue load. This degradation of the beams as indicated by the increase in strain can be explained by the fracture concrete and aggregate leading to debonding of the FRP bars from concrete. In Figure 7-13, the specimens with the Outdoor condition show a similar trend. For the

W&D condition (Figure 7-14), the effect of fatigue on the load-strain behaviour is not clear and the main-bar sensor in the static loading case stopped working after the initial stage of loading as mentioned earlier.

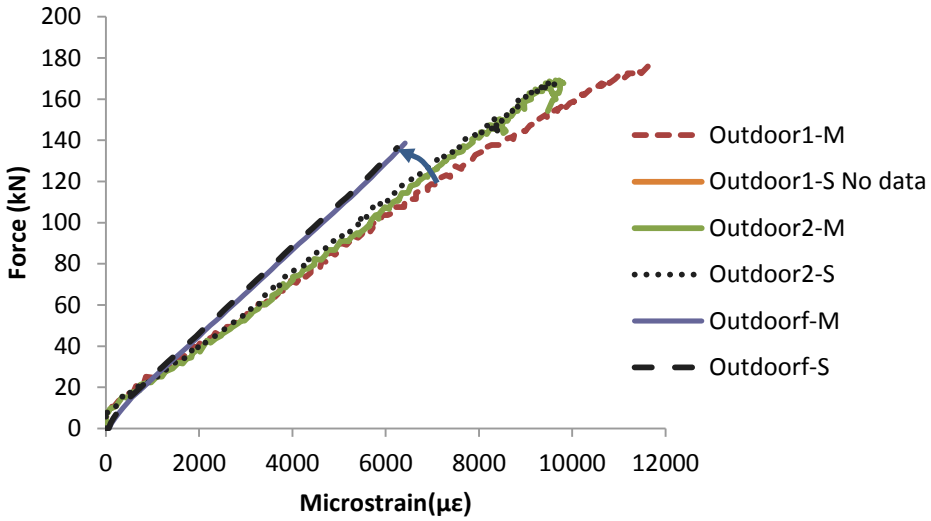

Figure 7-13 Initial Force-strain relations for the FOS in Outdoor specimens in static and fatigue tests

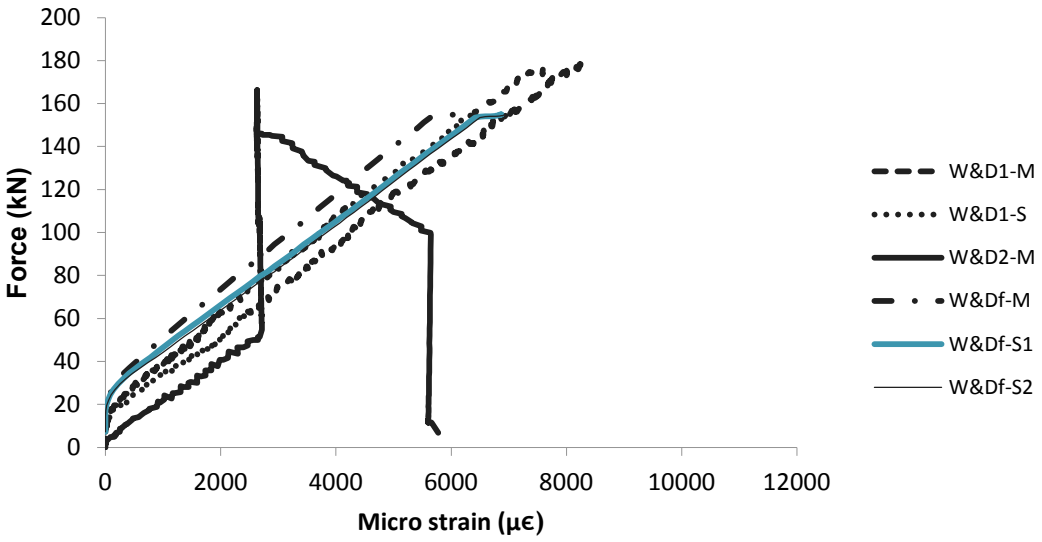

Figure 7-14 Initial Force-strain relations for the FOS in W&D specimens in static and fatigue tests

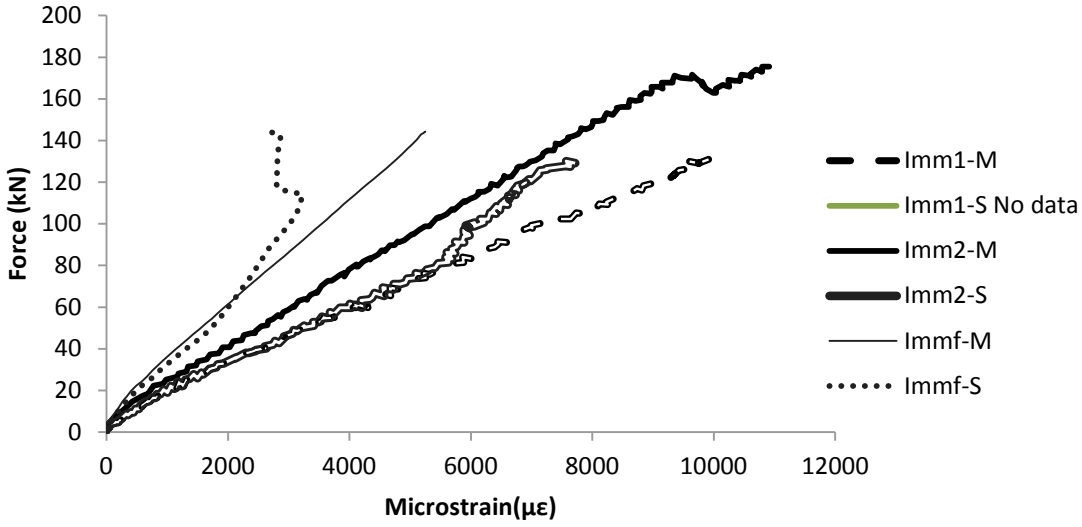

Figure 7-15 Force-strain relations for the FOS in Immersion specimens in static and fatigue tests

As shown in Figure 7-15, one of the supplemental-bar sensors (Imm1-S) did not work at all, and the other supplemental bar (Imm2-S) malfunctioned after 6000με because of the likely detachment of the sensor from the FRP bar. The sensors on the main and supplemental bars in case of specimen used for the fatigue load test (i.e., Immf-S and Immf-M) also showed unreliable results.

Structural degradation under fatigue as identified by the change in the strain was observed in the Immf and W&Df specimens (Table 7-5). The failure mode of the W&Df specimen was balanced failure with shear compression, which was not similar to the other conditions. The measured strain values in all conditions except that of the W&Df was found to be more than the theoretical values, which implies that a there was a good bond strength even in the cases of fatigue. The ratio of $\varepsilon_{exp}/\varepsilon_{Theo}$ for the strain in the main rebar is found to be the maximum (119%) in the case of Controlf specimen, which is used for normalizing the corresponding strain ratios in the other specimens. The strain response of the main and supplemental bars in Outdoorf specimen is very similar to that in Controlf specimen.

Table 7-5 The ultimate strain captured by FOS-M at mid-span under fatigue loads

Conditioning	f_c' (MPa)	ε_{exp}	ε_{Theo}	$\varepsilon_{exp}/\varepsilon_{Theo}$	Normalized
Immf	55	0.01	0.0093	107%	0.90
W&Df	55	0.008	0.0093	86%	0.72
Outdoorf	46	0.01	0.0084	119%	1
Controlf	46	0.01	0.0084	119%	1

The observed performance of the sensors under fatigue and the adverse environmental conditions are summarized in Table 7-6:

Table 7-6 Sensors function in fatigue and conditioning

	Controlf	W&Df	Outdoorf	Immf
FOS-M	✓	✓	✓	✓
FOS-S	✓	✓	✓	×
ESG	✓	4/6*	✓	5/6**

* Four out of six sensors are intact ** Five out of six sensors are intact

7.5. Post-fatigue Static Load Capacity

In order to find out effect of weathering and fatigue on load caring capacity of the beams, the post-fatigue specimens were tested under monotonically increasing static loading until failure. The post-fatigue residual capacities of these specimens were then compared to the static load capacities of the corresponding identical specimens which were not subjected to fatigue loading prior to the static load tests (Chapter 4). Figure 7-16 shows the force-deflection relations of the four specimens (i.e., Controlf, Outdoorf, W&Df and Immf) statically tested after one million cycles of fatigue loading. In general, fatigue and degradation of the material under alkaline solution and weathering exposure would likely cause debonding and internal damage to the interlocking resistance of the concrete aggregate. Outdoorf specimen showed the highest flexural strength, while it also showed higher deformability than that observed in Controlf, similar to that observed in the other two conditioned specimens (i.e., W&Df and Immf).

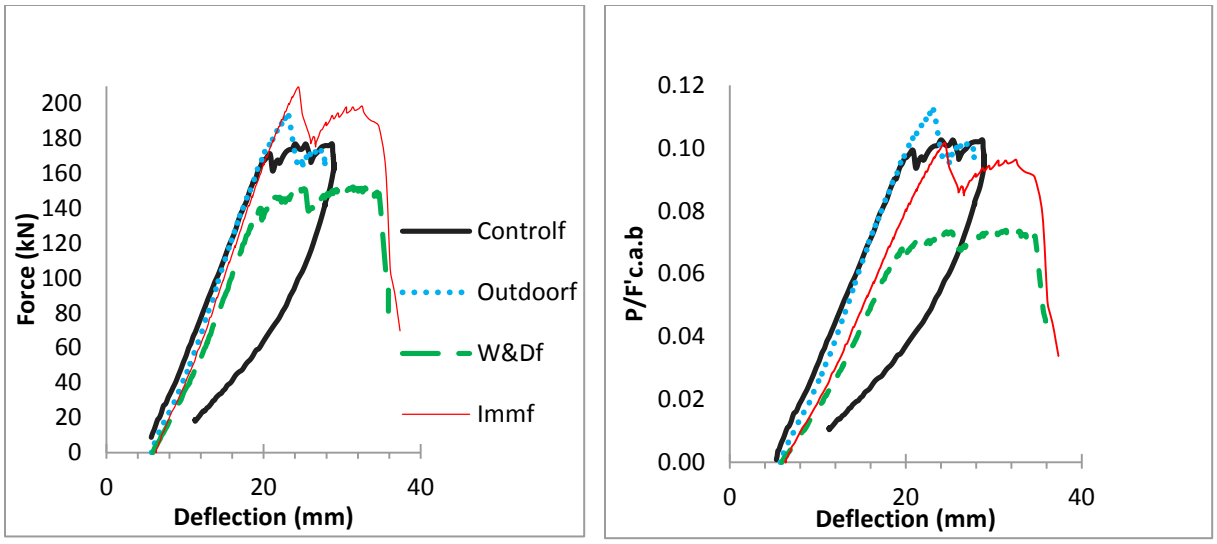

Figure 7-16 Force-deflection curve for the beams in static tests after 1 million fatigue load cycles: Left Load vs. deflection; Right – non-dimensional load vs. deflection

Figures 7-17 to 7-20 show the load-deflection curves of the individual post-fatigue specimens together with Control1 and the corresponding identical specimens that were not subjected to fatigue loading. In terms of the flexural resistance as observed in Figure 7-17 to 7-20, the cyclic loading does not show any serious effect on the Control, Imm and Outdoor-conditioned beams. Only the W&Df specimen exhibited an appreciable degradation under fatigue load. Figure 7-19 shows the load vs. mid-span deflection of the beams in W&D conditioning. From experimental test it is observed that only W&Df shows the minimum flexural resistance as it fails in balanced failure mode followed by shear compression when subjected to static loading after the fatigue cycles and the other specimens had compression mode of failure.

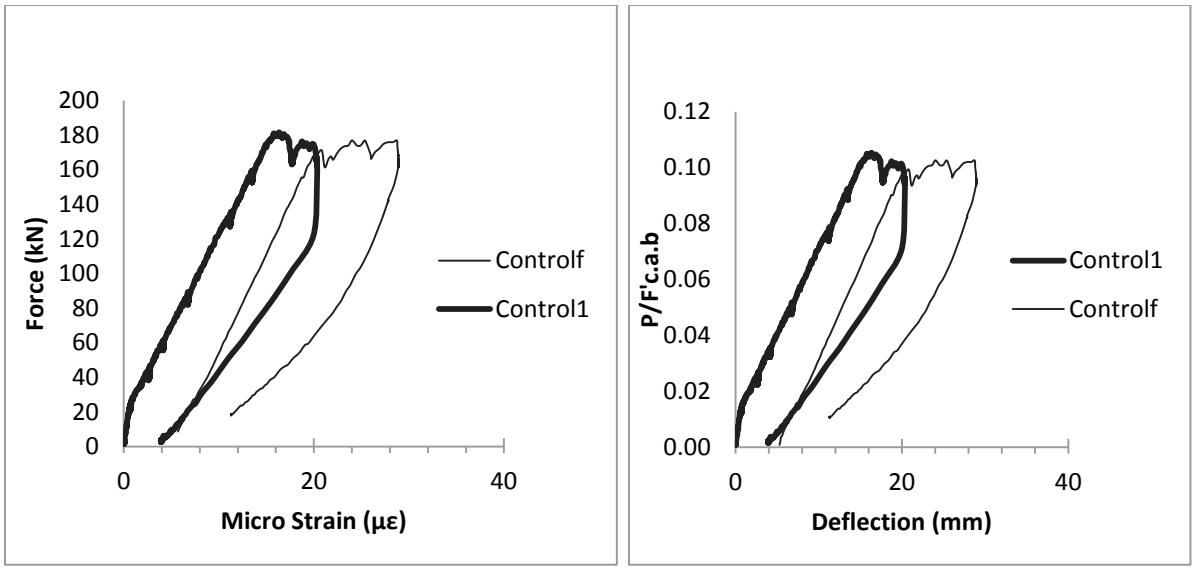

7-17 Load- deflections of the beams for Control specimens: Left - load vs. deflection; Right - non-dimensional load vs. deflection

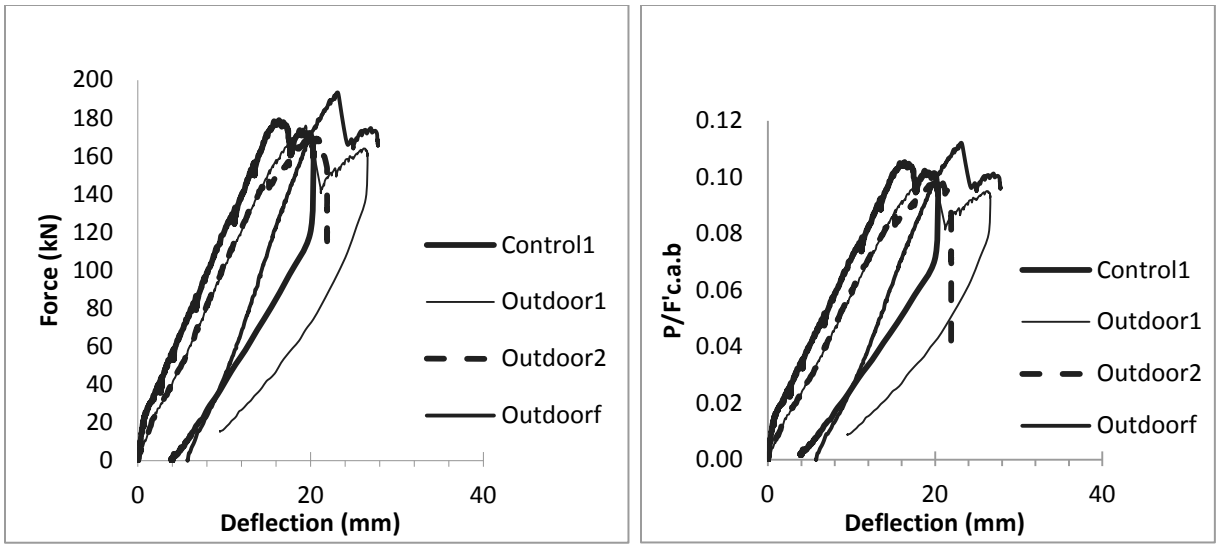

7-18 Load-deflection curves for beams under Outdoor conditions: Left – Load vs. deflection; Right – non-dimensional load vs. deflection

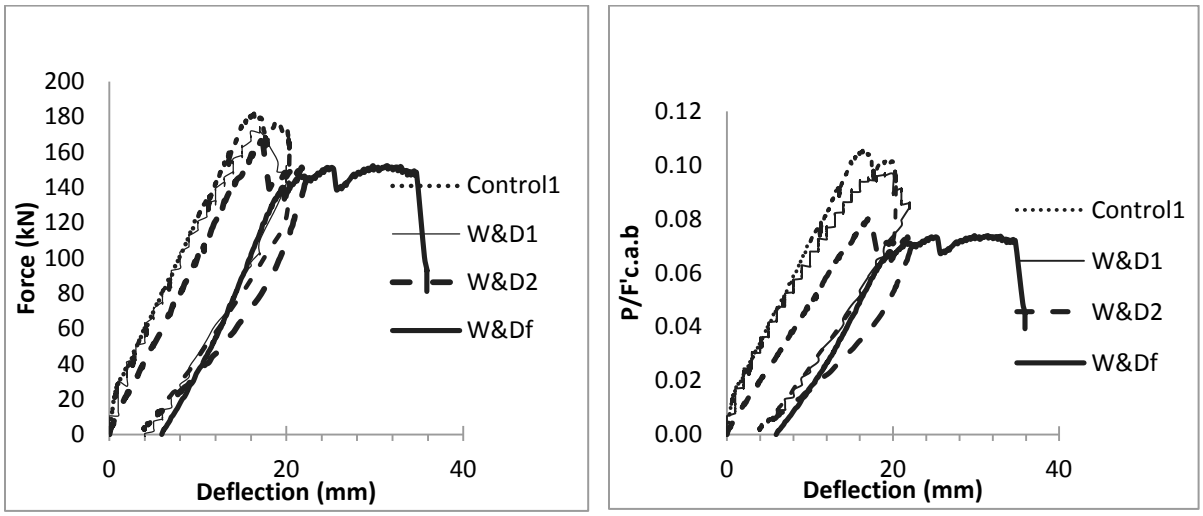

7-19 Load- deflections of the beams for beams under W&D conditions: Left - load vs. deflection; Right - non-dimensional load vs. deflection

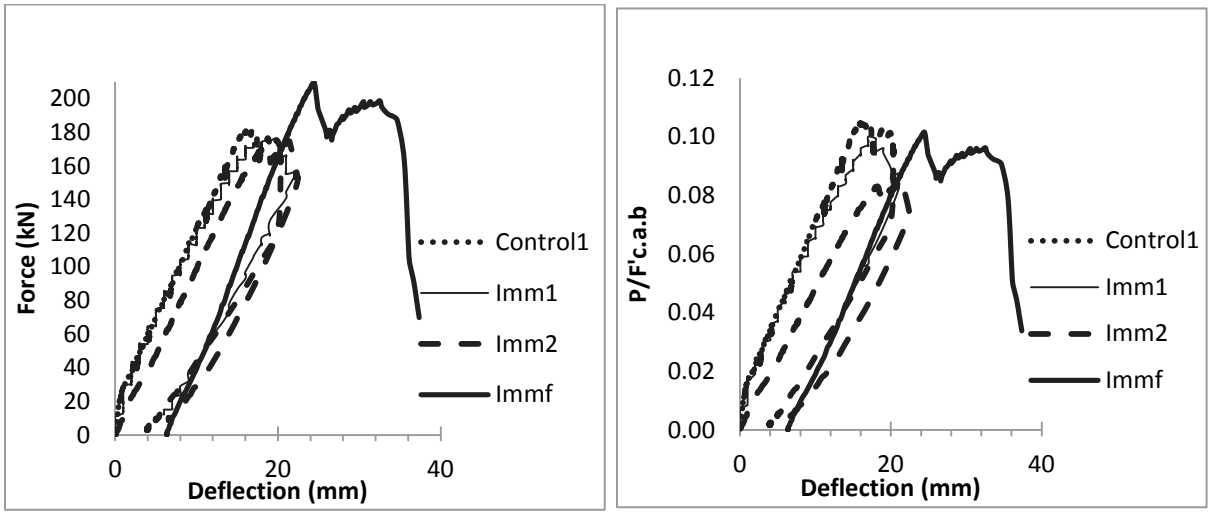

7-20 Load- deflections of the beams for beams under Immersion conditioning: Left - load vs. deflection; Right - non-dimensional load vs. deflection

7.6. Effect of Fatigue Loads on Deflection

Deflection in a beam or a girder is an important serviceability parameter. In all the conditions considered here, after about 600,000 cycles, the deflection exceeded the serviceability limit state (SLS), δ_s of L/360 as suggested in the ISIS (2007). For the specimens tested here in fatigue, the SLS for deflection, δ_s works out to be 4.58 mm as shown in Figure 7-21. The number of fatigue cycles corresponding to the SLS for deflection was found to be 650,000 in the case of Outdoor, 750,000 for immersion conditioning, 850,000 for the Control specimen, and more than one million under W&Df conditions (Figure 7-21). In this case, the W&Df specimen has the best performance in achieving the SLS for deflection (Figure 7-22). In Figure 7-22, the accumulated

degradation is derived from the summation of the measured deflection of the mid-point of the beam at every 50 or 100 thousands cycles during the entire loading regime.

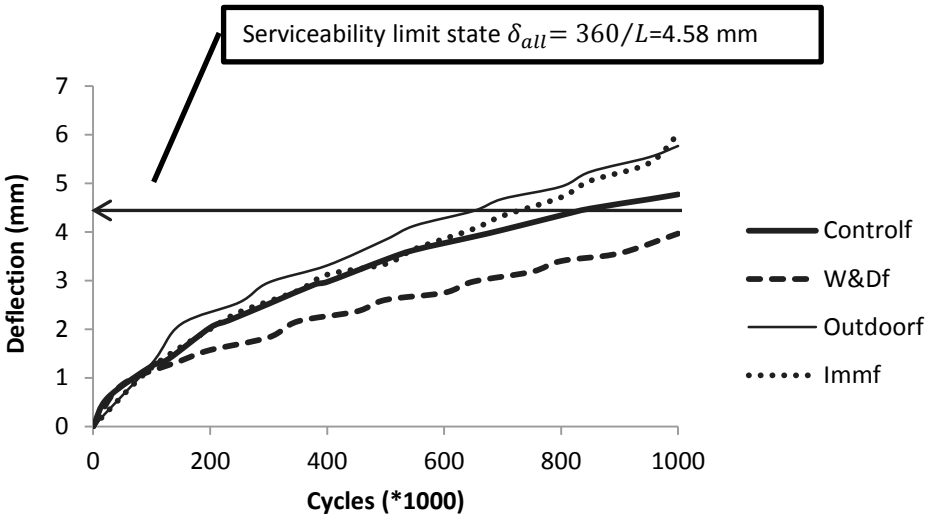

7-21 Deflection due to fatigue under all conditions

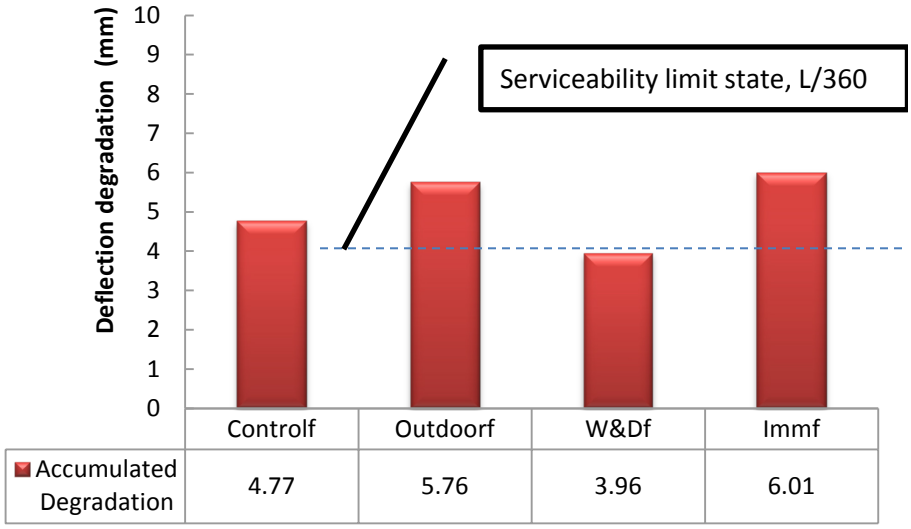

Figure 7-22 Comparison of accumulated degradation in different conditions

One of the methods which seem to be applicable for estimating the ultimate level of degradation due to fatigue load cycles is to find the stabilizing point on the deflection vs. the number of fatigue cycles curve (i.e. when the slope gets close to zero). In such a case, a beam reaches its ultimate level of degradation due to fatigue load cycles and may not degrade any further due to additional load cycles; but may fail abruptly if the load cycles are continued. Figure 7-19 shows the mid-span deflection of the beams against the fatigue cycles considering all specimens, and the best fit curve with the coefficient of determination R^2 of 0.82. More experimental work with higher number of cycles would be necessary to define more points closer to the stabilization point or the turning point on the deflection curve and thereby define a trend line with different characteristics to allow for the estimation of the rate of degradation as elaborated in Section 7-8. From Figure 7-19, the stabilization point can be found at 1.5 million cycles by considering the slope of the fitted curve (*dy/dx*) to be zero.

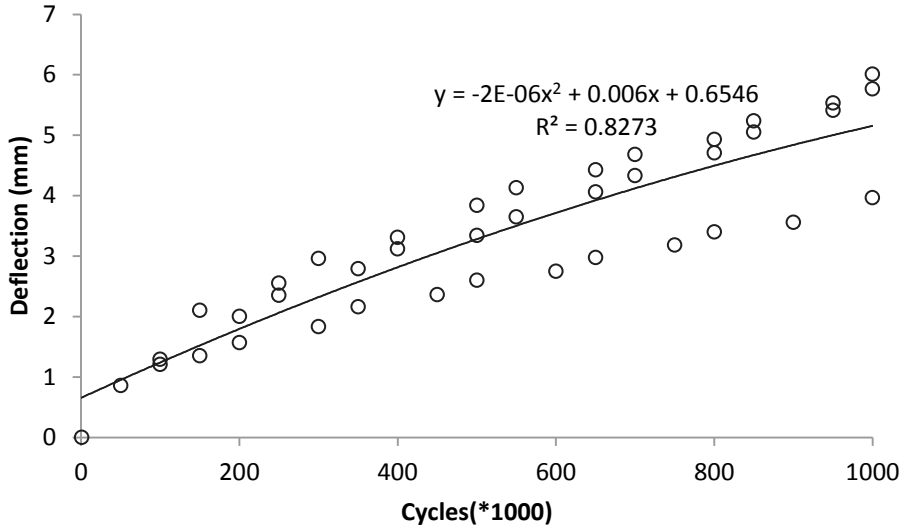

Figure 7-23 Fitted curve to relate the change in deflection due to fatigue cycles, considering all conditions

7.7. Deflection-Based Rate of Degradation Due to Fatigue

For each individual condition considered here, the trend line or the best-fit line for the degradation or the change in transverse deflection in a beam with a given number of fatigue cycles was derived and plotted on a semi-log scale as shown in Figures 7-24 to 7-28. The best-fit line or the trend lines for degradation against the number of fatigue cycles for all the specimens are compiled into one graph as shown in Figures 7-28. The magnitude of degradation is computed after every 50,000 cycles by calculating the difference in the maximum and minimum deflection recorded by the actuator from the early cycles and the last cycles. The degradation of the beam as reflected by an increase in the deflection under fatigue is displayed by D_i (mm) for every condition, and N is the number of cycles. The best fit-curves derived for the different cases are given by Eq. 7-6 and the values of the coefficients "a" and "b" were obtain for different cases are summarized in Table 7-7.

Equation 7-6 $$D_i = a[\ln(N)] + b$$

Table 7-7 The values of the coefficients a and b used in Eq. 7-6 for computing the deflection-based rate of degradation coefficient

Condition	Coefficients	
Controlf	-0.235	1.781
W&Df	-0.177	1.369
Outdoorf	-0.363	2.667
Immf	-0.332	2.476

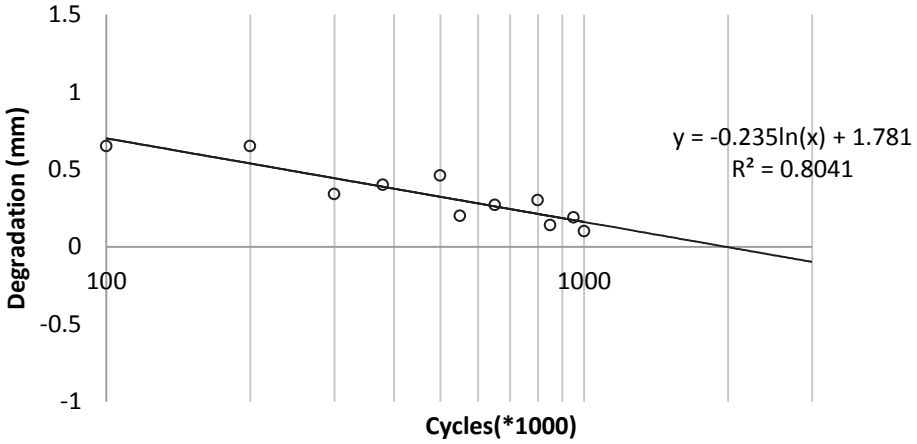

Figure 7-24 Degradation in the Controlf specimen

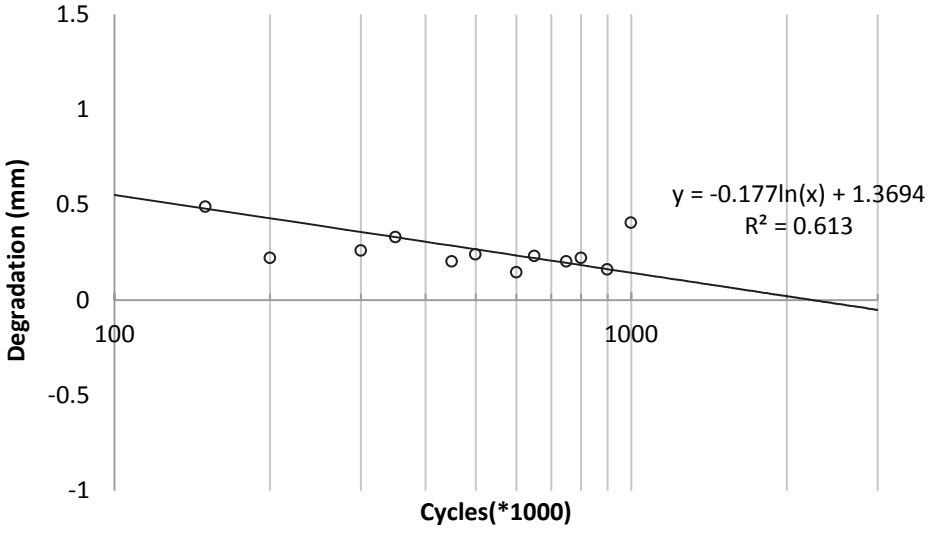

Figure 7-25 Degradation in the W&Df specimen

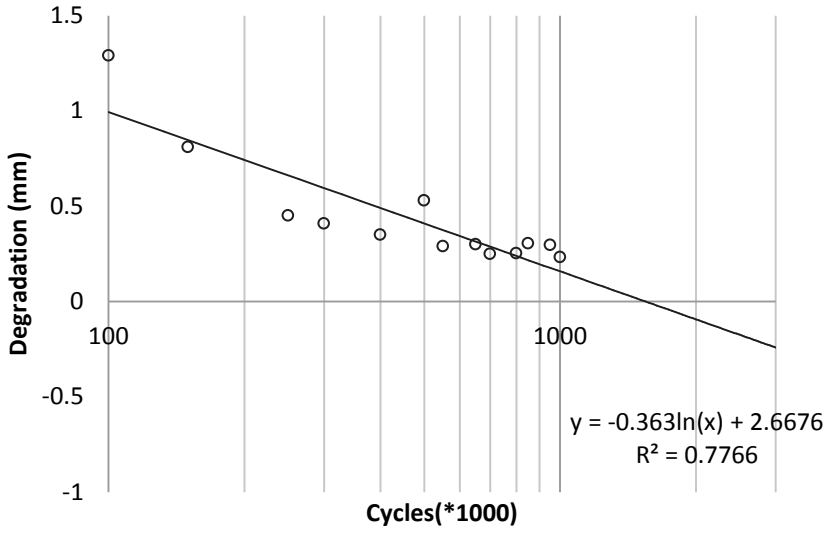

Figure 7-26 Degradation in the Outdoorf specimen

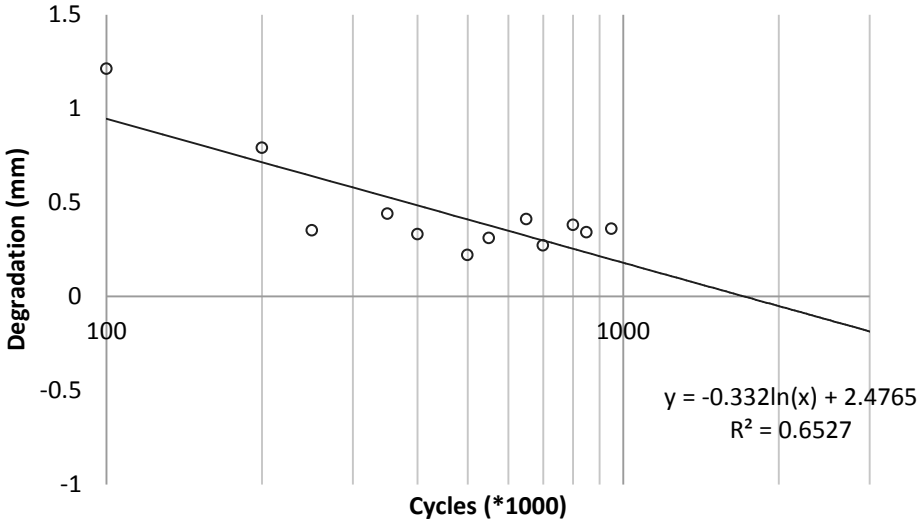

Figure 7-27 Degradation in the Immf speciemn

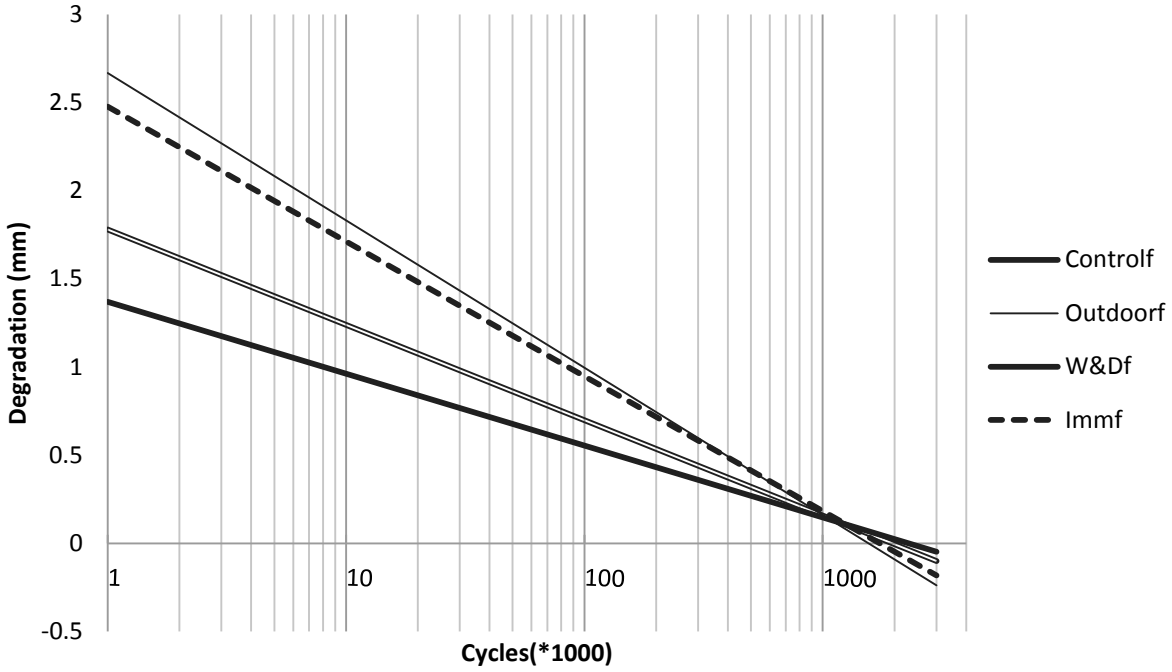

Figure 7-28 Trend lines for the degradation in different specimens

From Figure 7-24 to Figure 7-27, it can be observed that the rate of change in the deflection due to fatigue cycles decreases with the increasing number of cycles, and eventually becomes zero. The number of cycles at which the rate of change in the deflection becomes zero (turning point in deflection vs. number of cycles diagram) can be defined as the number of cycles at which the deflection in a beam stabilizes and the beam does not degrade any further due to cyclic loads. Before reaching this stage, the strength and stiffness of a beam continue to degrade due to the increase in crack width and length, the loss of the effect of aggregate interlock and resulting friction, and degradation of the bond strength between the rebar and concrete. The deflection stabilizes when the above-mentioned effects cannot advance any more. The maximum number of

cycles required for stabilizing the deflection, N_s is defined by the point where trend line for degradation of a specimen intersects with the horizontal axis (number of cycles line). From Figure 7-28, the value of N_s was determined to be 2.1 million cycles for W&Df condition, 1.7 million cycles in the case of Immf, 1.5 million cycles in the cases of Outdoorf and 1.8 million cycles in Controlf.

7.8. Bond Degradation

Bank et al. (1998) conducted a set of pullout tests to study the bond degradation due to conditioning by water immersion at 80°C. Their SEM results showed the degradation of FRP, and based on those results, they proposed a relationship between bond strength and material degradation. As discussed before, the strain measurement in Immf and W&Df is not reliable; and therefore, these data cannot be used for the calculation of the bond strength for these specimens. Table 7-8 shows that the magnitudes of the bond stress in Outdoorf condition doesn't change due to fatigue and its value is estimated as 0.96 MPa, which is close to the bond strength for Controlf specimen before fatigue (0.90MPa). The Controlf specimen shows degradation due to fatigue in the amount of 17% or so, which is considerable.

The following formula (Equation 7-7) is applied for the calculation of the relative bond strength in all conditions as considered in this study, using the strain in the rebars at the mid and quarter spans (left or right).

Equation 7-7 $$\tau = \frac{Ed(\varepsilon_2 - \varepsilon_1)}{4L}$$

where, τ is the shear stress MPa, E is the Modulus of elasticity of GFRP bars, D is the diameter of the GFRP bars, and L is the distance between the two measuring gauges, which is 400 mm.

ε_2, ε_1 = strain measured from the middle and the right or left gauge

Table 7-8 shows the bond strength calculated for beam specimens in different conditions. The shear stress in the control specimen in the post-fatigue test was found to be 17% less than that in the control specimen tested without subjecting it to any fatigue load. However, the fatigue loading does not appear to have any effect on the bond strength of the specimens subjected to Outdoor condition. It is notable that post-fatigue condition refers to the data recorded after one million cycles of fatigue loads.

Table 7-8 Summary of bond strength derived from the results of static and post-fatigue tests

Specimen	**Control**	**W&D**	**Imm**	**Outdoor**
Failure Mode	Compression	Compression	Compression	Compression
Static shear stress(τ_s)	0.90	N/A	N/A	0.96
Post-fatigue shear stress (τ_f)	0.73	N/A	N/A	0.96
Experimental captured strain	0.01 = 0.66 $\varepsilon_{u,frp}$	0.008 = 0.53 $\varepsilon_{u,frp}$	0.01= 0.66 $\varepsilon_{u,frp}$	0.01=0.66 $\varepsilon_{u,frp}$

7.9. Change in the Crack Width

The cracks in an FRP-reinforced beam are expected to be wider than those in an equivalent steel-reinforced beam. The following formulae are suggested in ACI 440.1R-06 and CSA-S806-12 for estimating the crack width in FRP-reinforced concrete flexural members:

Equation 7-8 $w = \frac{2.2}{E_f}\beta k_b f_{frp}\sqrt[3]{d_c A}$ (ACI 440.1R-06)

Equation 7-9 $w = \frac{2f_{frp}}{E_f}\beta k_b\sqrt{{d_c}^2 + (\frac{s}{2})^2}$ (CSA-S806-12)

where, *w* is the crack width at the tensile face of a beam in mm; E_f is the modulus of elasticity of FRP in MPa; β is the ratio of the distance from the neutral axis to the extreme tension fiber to the distance from the neutral axis to the center of the tensile reinforcement; k_b is the bond-dependent coefficient; f_{frp} is the stress in the tension FRP reinforcement at the location of the crack in MPa; d_c is the concrete cover measured from the centroid of tension reinforcement to the extreme tension surface in mm; A is the effective tension area of concrete surrounding the flexural tension reinforcement and with the same centroid as that reinforcement, divided by the number of rebars (mm^2); and s is the spacing of the longitudinal FRP bars in mm.

In the above formula (i.e., Eq. 7-8), $\beta = 1$, and k_b defines a degree of bond which is assumed to be equal to one for a bond strength similar to that of steel reinforcement; and for FRP, this value can be assumed to be 0.71, 1.00, or 1.83, based on different tests. Table 7-8 shows the width of the cracks and the corresponding values k_b calculated from different cases in the present experimental study:

Table 7-9 Theoretical calculation of k_b

Condition	Controlf	Outdoorf	W&Df	Immf
ω(Crack width)	0.88	0.94	0.97	0.99
ε_{frp}	0.01	0.01	0.008	0.01
k_b **(ACI 440.1R-06)**	0.78	0.83	1.07	0.88
k_b **(CSA 806-12)**	0.81	0.87	1.12	0.91

The values of k_b as reported in Table 7-8 were calculated after the application of one million cycles of loads, and the range of the values of k_b are observed to be between 0.78 and 1.12 for the two suggested formulae. These values are consistent with the values suggested in the (ACI 440.1R-06 2006) as summarized below.

- For k_b >1.0 bond behavior is inferior to steel
- For k_b<1.0 bond behavior is superior to steel

Based on the results presented in

Table 7-9, it can be noted that the bond in W&D conditions is inferior to that of steel, and in the other conditions, the bond behavior is superior to that of steel. It is also observed that the bond strength degrades with any conditioning, as reflected by the increase in the value of k_b.

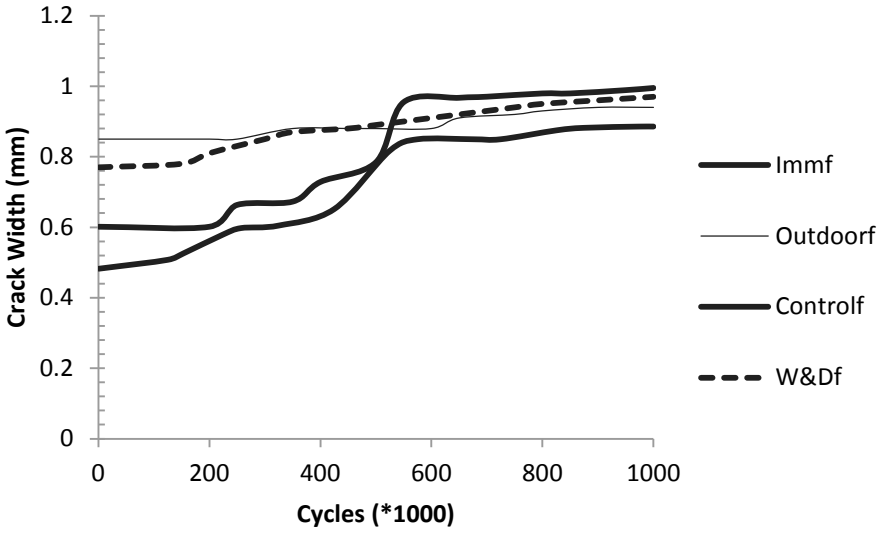

Figure 7-29 Crack width under fatigue after first cycle

Crack width at the mid span is measured by following the guidelines provided in CSA-S806-12. The crack width was measured after every 100,000 cycles, and it continued up to one million cycles for every condition. Figure 7-29 shows the crack-width with the increasing number of fatigue cycles. It is observed from the figure that the variation in the crack width follows a similar trend in all the cases, with some minor differences arising from the change in the load protocol (Figure 3-17). The crack width at the end of 1 million load cycles was found to be the maximum in the case of immersion conditions, and the minimum in the case of the control

specimen. The value of σ_{mean} ( ) in Immf specimen was found to be 0.75-0.85 F_u, which is much lower than that in the cases of Outdoorf and W&Df specimens. However, the crack width was found to be the maximum in the case of Immersion (Immf specimen). A similar value of the crack width was obtained in the case of W&Df and Immf specimens. It shows that a the variable stress state makes cracks wider than that under uniform stress variation. A wide and expanded crack mouth was more tangible during the fatigue test in the case of Outdoorf specimen.

Figure 7-30 shows the variation of the strain with crack width, which can be used for estimating the expected failure load based on the crack width measurement. In this case, the best fitted curve can be generated, or a similar curve for constant weathering conditioning can be chosen directly. The corresponding number of cycles and the residual capacity can then be estimated from the measured width of the cracks. The procedure explained above would require a neural network or statistical pattern-based approach for gathering and synthesizing the statistical data from of crack inspections. This method is not explored further in the present study.

7.10. Permissible Crack Width

Pursuant to the ISIS guideline (ISIS, 2007), if a structure is not occupied, the crack width does not need to be considered in the design. However, a strain limitation of 2000 με and in some cases up to 3000 με should be used to limit the crack width. In the recently revised Canadian code (CSA S806-12, CSA S807-10), the durability testing should be performed at 0.3% strain, while the limit of 0.2% strain should be considered for sustained loads. The beams were instrumented to measure the width of the flexural cracks at the mid-span and the shear cracks

near the supports after they appeared during the first cycle of loading. This allowed the measurement of the crack width parameter CMOD as the cracks widened.

Figure 7-30 shows the relationship between the measured strains with the crack width for all the specimens tested in fatigue. From the figure, it can be seen that the crack width in the case of Controlf specimen is 0.6 mm, and for Outdoorf, it is 0.4 mm at the level of 2000 με; while in the cases of Immf and W&Df specimens, the crack width is observed to be 0.2 mm. This indicates that the alkalinity helps to reduce the crack width by reducing the aggregate friction and interlocking as compared to the control condition. Outdoor conditioning (Outdoorf specimen) makes the crack width almost double that of the Immersion and W&D conditions.The crack width under the maximum strain is also associated with the Controlf specimen. The Outdoorf specimen has a very linear crack width behavior as observed during the test (very clear cracks under loading and broken crack edges which facilitated easier closing of the crack on unloading).

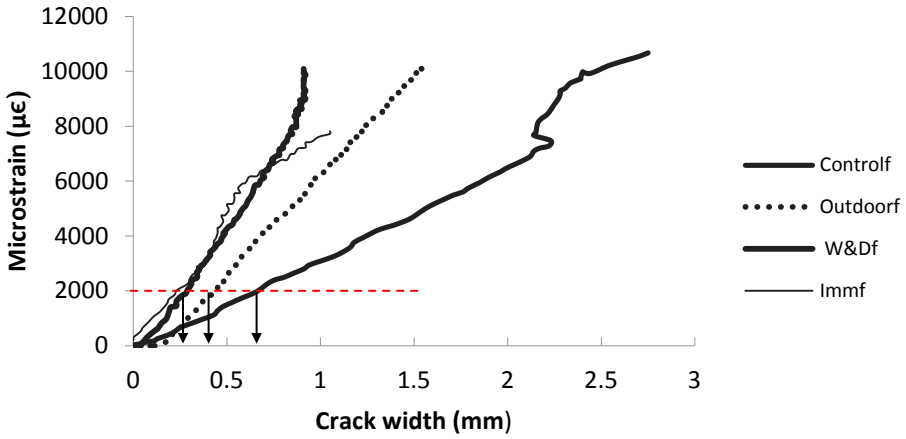

Figure 7-30 Crack width vs. strain in all conditions

7.11. Prediction of Deflection and Crack by Service Limit State (SLS) Control

By using Equation 7-6 , the deflection can be estimated for each condition. The values of the coefficients are shown in Table 7-7. The curves Fig. 7-31 showing the variation of the deflection and crack width with the number of fatigue cycles can be utilized for determining the number fatigue cycles corresponding to the deflection and crack width limits. As observed from the experimental results, the crack width in all conditions reached a constant amount of 0.9-1 mm. The serviceability limit states (SLS) for deflection (e.g. L/360) and crack width (e.g. 0.71 mm as specified in ACI 440.1R-06 can be used for determining the corresponding limiting value of the number of fatigue cycles. By assuming the maximum allowable crack width of 0.7 mm (ISIS, 2007), the number of cycles goes up to more than 420,000 cycles in the Controlf specimen, and the deflection of the beam is close to 13 mm (Figure 7-31).

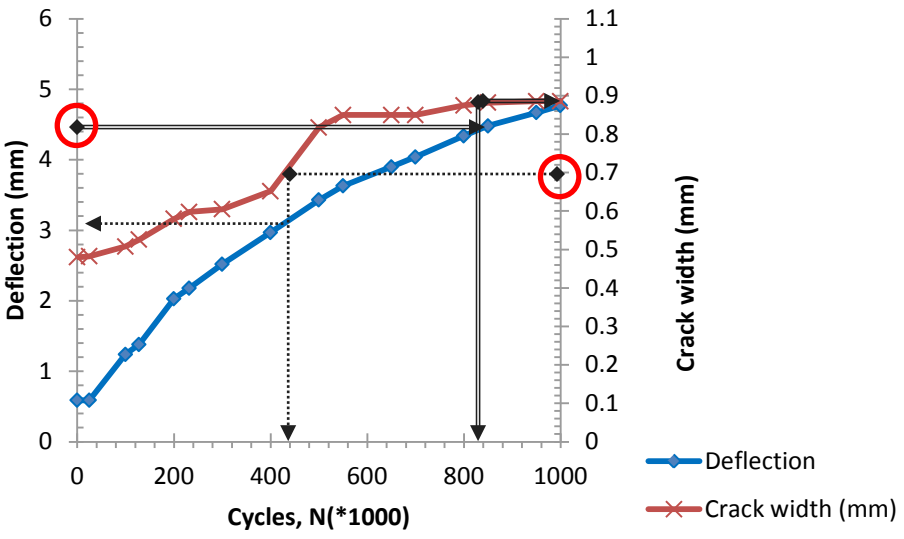

Figure 7-31 Prediction of deflection and crack width by SLS in Controlf condition

In the control condition, the maximum number of fatigue cycles corresponding to the allowable deflection (i.e., L/360) of 4.58 mm is found by extrapolation to be 800 thousands. In that case, Figure 7-31shows the corresponding crack width is 0.9 mm. Figure 7-32 to Figure 7-34 show the variation of deflection and crack width with the number of loading cycles at different conditions, and reveal how the limiting numbers of fatigue cycles corresponding to the SLSs are obtained. The results for all the specimens at different conditions has been summarized in

Table 7-10

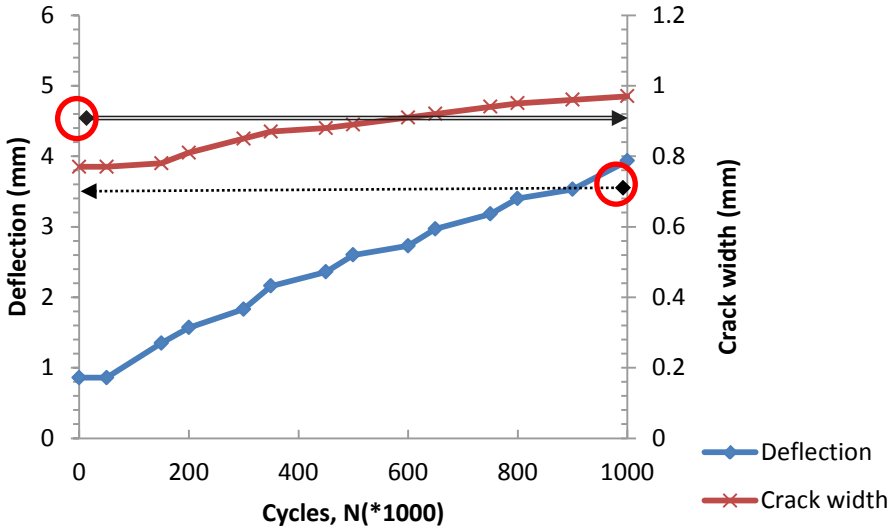

Figure 7-32 Prediction of deflection and crack width by SLS in W&Df condition

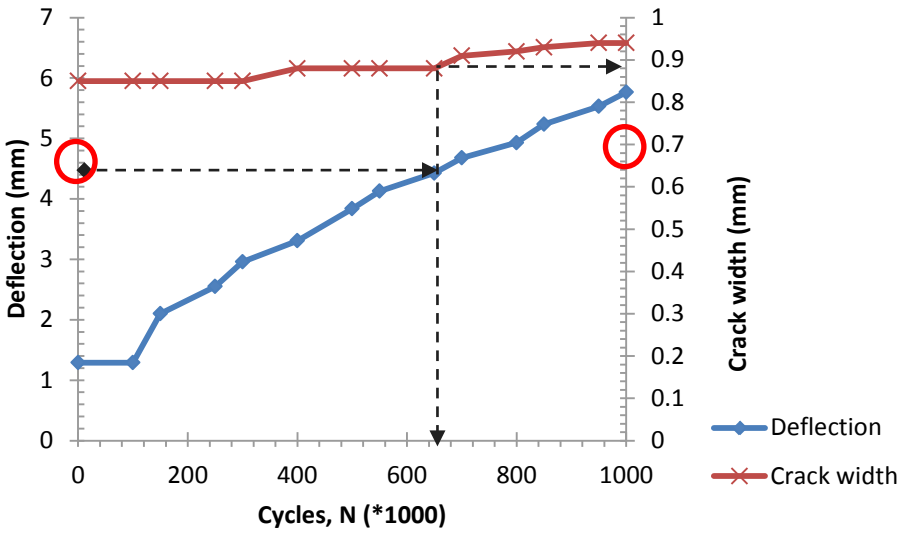

Figure 7-33 Prediction of crack width & deflection by SLS in Outdorf condition

In W&Df specimen, the deflection and crack width do not reach the SLS limit state and high life cycle is expected.

In Outdoorf specimen, a similar behavior is observed for crack serviceability control, but corresponding to the deflection SLS at 650,000 cycles, the crack width is calculated to be almost 0.9 mm which is more than allowable SLS.

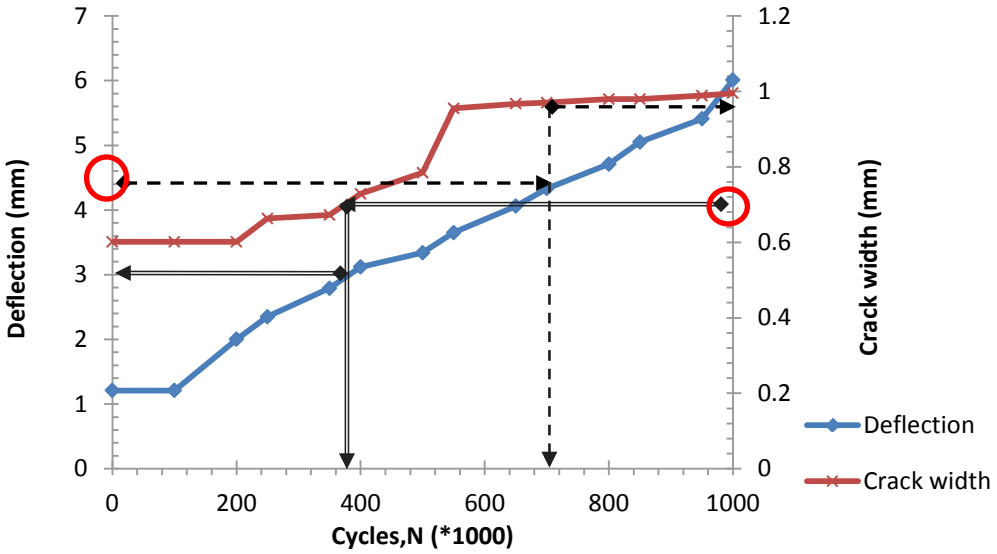

Figure 7-34 Prediction of crack width & deflection by SLS in Immf condition

The Immf specimen reached the crack width SLS in 400,000 cycles with a lower value of the deflection than the SLS. On the other hand, by considering the deflection SLS, the crack width reaches 0.95mm in 750,000 cycles.

Figure 7-35 shows the variation of the deflection and crack width with the number of fatigue cycles considering the experimental results for the three different conditions (W&D, Outdoor and Immersion). The reason for this selection is the similarity in the mean stress values and better simulation of the real case. It is assumed that the maximum crack width reaches a constant magnitude of almost 0.95 mm based on results from the experiment. The maximum number of cycles reached 250,000 cycles corresponding to the crack width and deflection SLS.

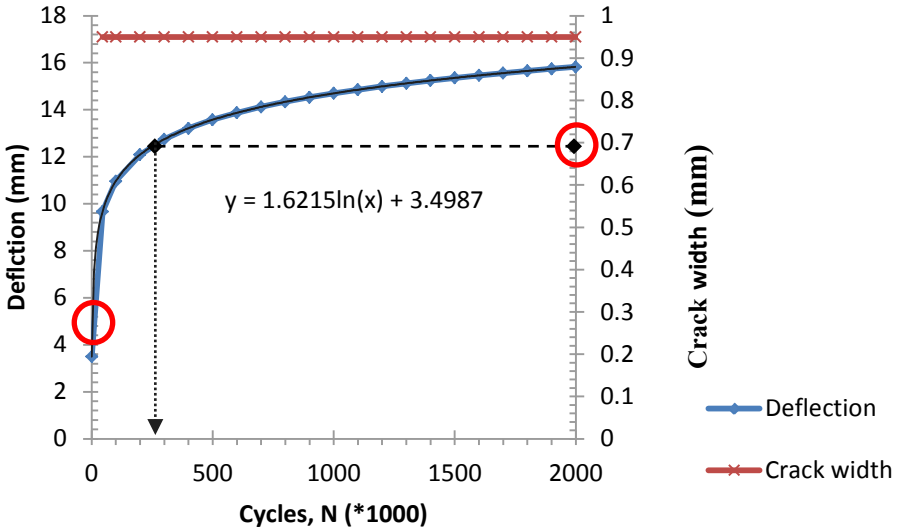

Figure 7-35 Prediction of the number of cycles by SLS as a combination of 3 conditions

7.12. Flexural Crack width and Deflection Service Limit State (SLS)

For the deflection Service Limit State (SLS), the deflection of 4.58 mm was obtained by L/360. The estimated number of fatigue cycles corresponding the deflection SLS for W&Df was found to be more than one million cycles. The minimum value of the corresponding number of cycles was found to be 650,000 for Outdoorf specimen; and 250,000 when all the conditioned specimens were taken together (i.e., W&Df, Outdoorf, and Immf specimens) and in that case, the corresponding crack width exceeded the limit of 0.7 mm.

For the crack width SLS, the maximum number of the cycles was estimated to be 440,000 and 400,000 cycles for Controlf and Immf specimens. The W&Df and Outdoorf conditions, pass the crack service limit state from the beginning for its higher target average load (σ_{ave}). The

maximum degradation in Immf and Controlf specimens were found to be similar (3 mm).Table 7-10 shows the number of fatigue load cycles and the crack width corresponding to the deflection SLS, while Table 7-11 shows the number of fatigue load cycles and deflection corresponding to the crack width SLS.

As it can be observed from Table 7-10 and Table 7-11, and Figure 3-17 the crack width SLS corresponds to a higher number of cycles than the deflection SLS. It can be concluded that the deflection SLS in FRP-RC beams is more appropriate in all the tested conditions, in which case, the crack width would reach maximum value of about 1.0 mm (Table 7-10). In that case, the structure still remains repairable and can have a longer service life. Prediction of crack width for all conditions after 500,000 cycles has been shown in Table 7-12.

Table 7-10 Prediction of the number of cycles by deflection control

	Condition	**Cycles(*1000)**	**Crack width(mm)**
Deflection SLS	Controlf	800	0.9
	W&Df	>1000	0.95
	Outdoorf	650	0.88
	Immf	750	0.95
	All conditions	250	0.95

Table 7-11 Prediction of the number of cycles by crack width control

	Condition	Cycles(*1000)	Degradation (mm)
Crack width SLS	Controlf	440	3
	W&Df	Passing the limit of 0.7 mm	
	Outdoorf	Passing the limit of 0.7 mm	
	Immf	400	3
	All conditions	Passing the limit of 0.7 mm	

Table 7-12 Flexural crack width formula in all conditions

Condition	Crack width	R^2(coefficient of variation)
Controlf	$\omega = 0.1784N^{0.4766}$	0.99
Outdoorf	$\omega = 0.114N^{0.5664}$	0.99
W&Df	$\omega = 0.0599N^{0.6021}$	0.97
Immf	$\omega = 0.0236N^{0.7963}$	0.98

7.13. Shear Crack

The width of the shear cracks (at the shear spans) under fatigue load cycles were measured in a similar way as the flexural cracks and the Crack Mouth Opening Displacement (CMOD) of the most tangible crack was measured at every 50 or 100 thousands cycles (Figure 7-36). CMOD has been defined earlier in Chapter 2. The maximum CMOD from Figure 7-37 corresponds to Outdoorf and Controlf. In Immf and W&Df specimens, the minimum value of CMOD is

detected in fatigue while these two cases showed the maximum change in the flexural CMOD under fatigue load. The rate of change in the CMOD in all conditions after 600,000 cycles is similar to that for flexural CMOD (Figure 7-38 to Figure 7-41). The greatest jump in shear CMOD corresponds to Outdoorf specimen which could be due to the freeze-thaw effect on the shear strength, bond and mechanical properties of the aggregates. The freeze-thaw effect on the exposed surface of the beams was evident from visual inspection. The degradation rate in shear and flexural CMOD in both Controlf and W&Df specimens are found to be close to each other. The comparison of the shear and flexural cracks in all the specimens are shown in Figures 7-38 to 7-41.

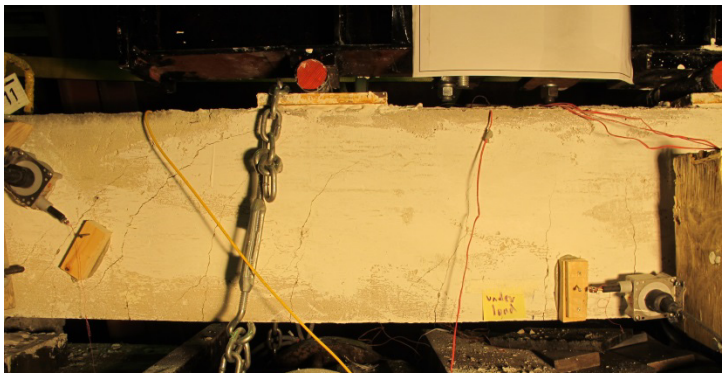

Figure 7-36 Shear and flexural crack measurement by potentiometer

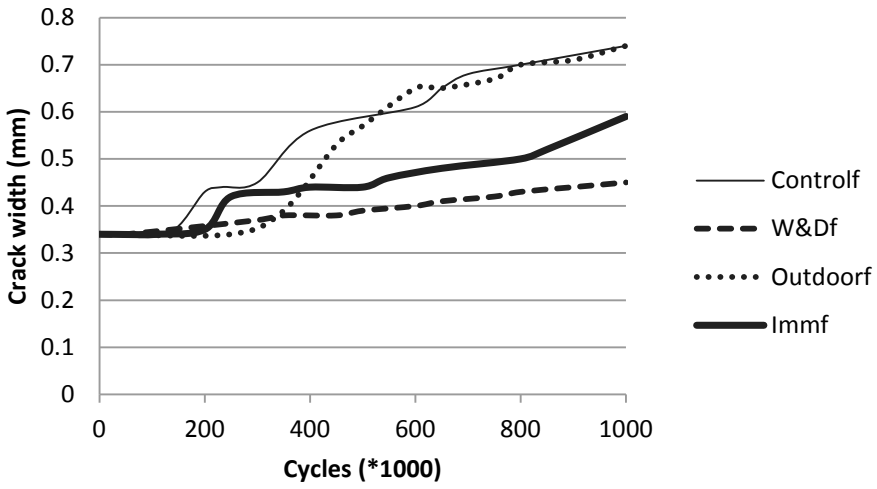

Figure 7-37 Shear crack in all conditions after first cycle

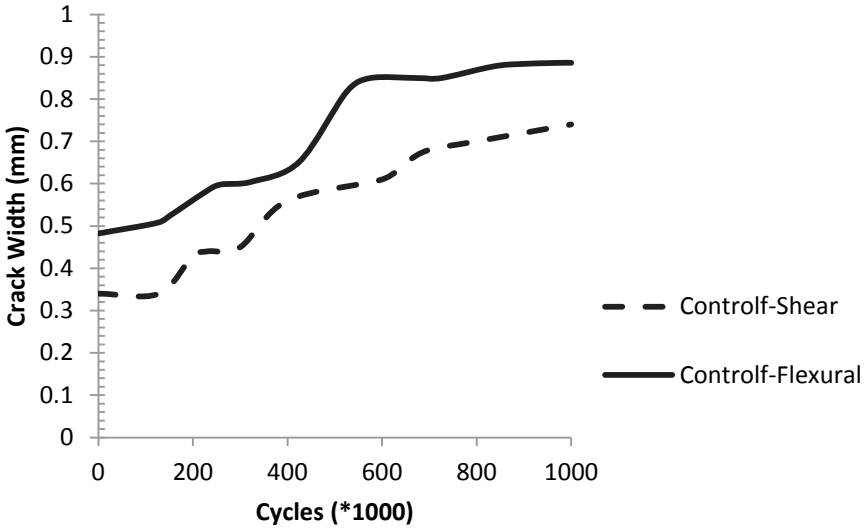

Figure 7-38 Comparing shear and flexural crack in control condition after first cycle

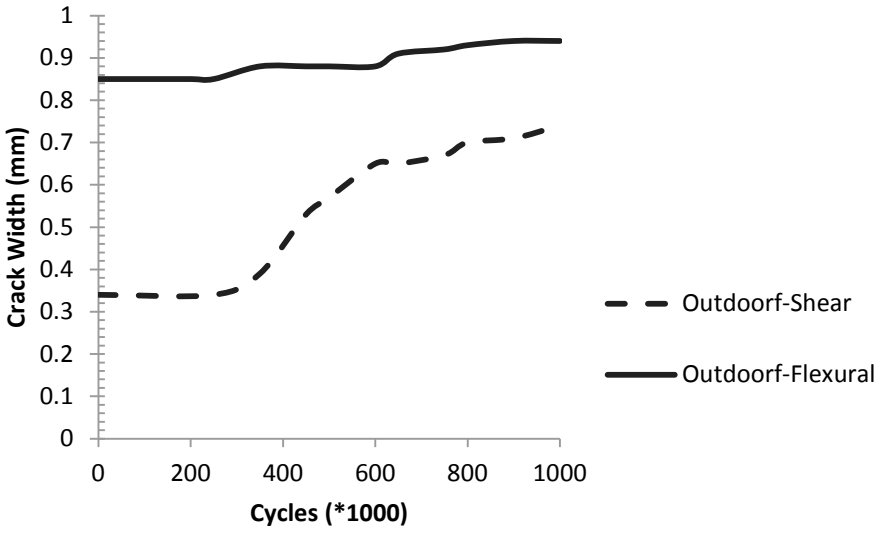

Figure 7-39 Comparing shear and flexural crack in outdoor condition after first cycle

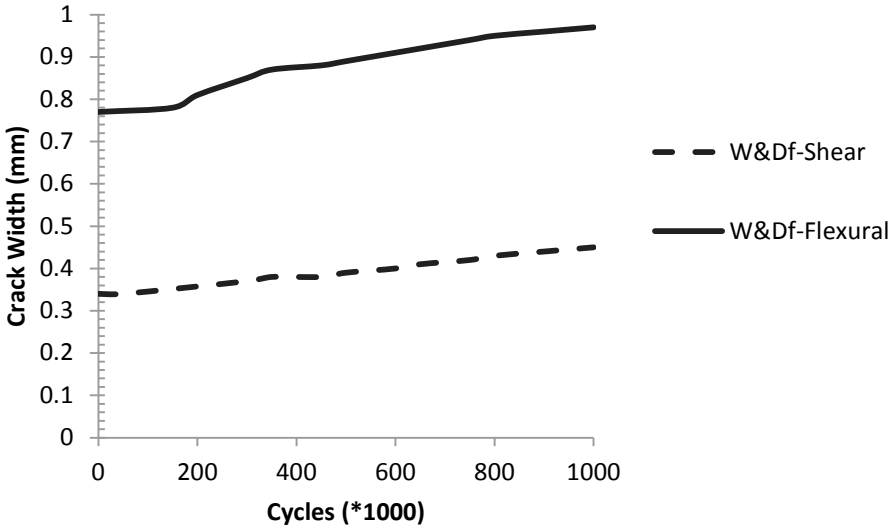

Figure 7-40 Comparing shear and flexural crack in W&D condition after first cycle

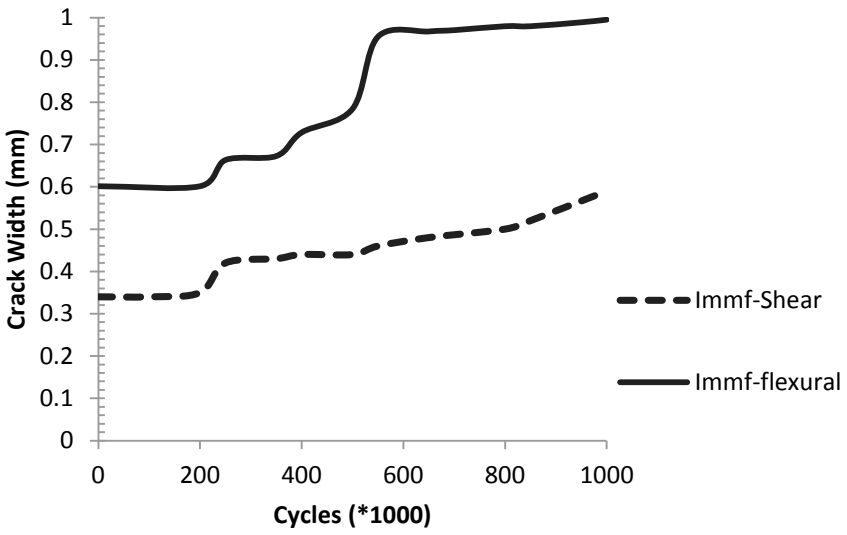

Figure 7-41 Comparing shear and flexural crack in immersion condition after first cycle

In order to compare the trend of shear crack in all conditions trend after 500,000 cycles selected to have constant target load in Controlf and Immf (Figure 3-17).The results for all the conditions are shown in Table 7-13. .

Table 7-13 Shear crack width formula in all conditions

Condition	**Crack width**	**R^2 (coefficient of variation)**
Controlf	$\omega = 0.4586N^{0.0967}$	0.91
Outdoorf	$\omega = 0.4738N^{0.1}$	0.90
W&Df	$\omega = 0.4448N^{0.1128}$	0.99
Immf	$\omega = 0.6346N^{0.0648}$	0.98

7.14. Residual Strain

The residual strains obtained from FOS-M and FOS-S in the experimental tests show that they differ by less than 10%. Thus the residual strain calculated using the strain data from FOS-M has been used. In the Figure 7-42, the variation of the cyclic strain with the number of fatigue cycles shows non-zero strain-residual after one million cycles. The residual strain at the end of the fatigue cycles is labelled here as the Total Residual Strain (TRS). This value is the summation of two different components of the accumulated strain. The first strain component relates to the cyclic loading which is shown by R1 and R2 in Figure 7-42. The second component corresponds to the residual strain (D) due to static loading and unloading cycles. The results of the experiments show there is a variation of D in different loading-unloading cycles and no specific trend observed can be observed in such variation. This can be due to the aggregate interlocking and material bridging which can be altered when the aggregates get crashed due to cyclic loading.

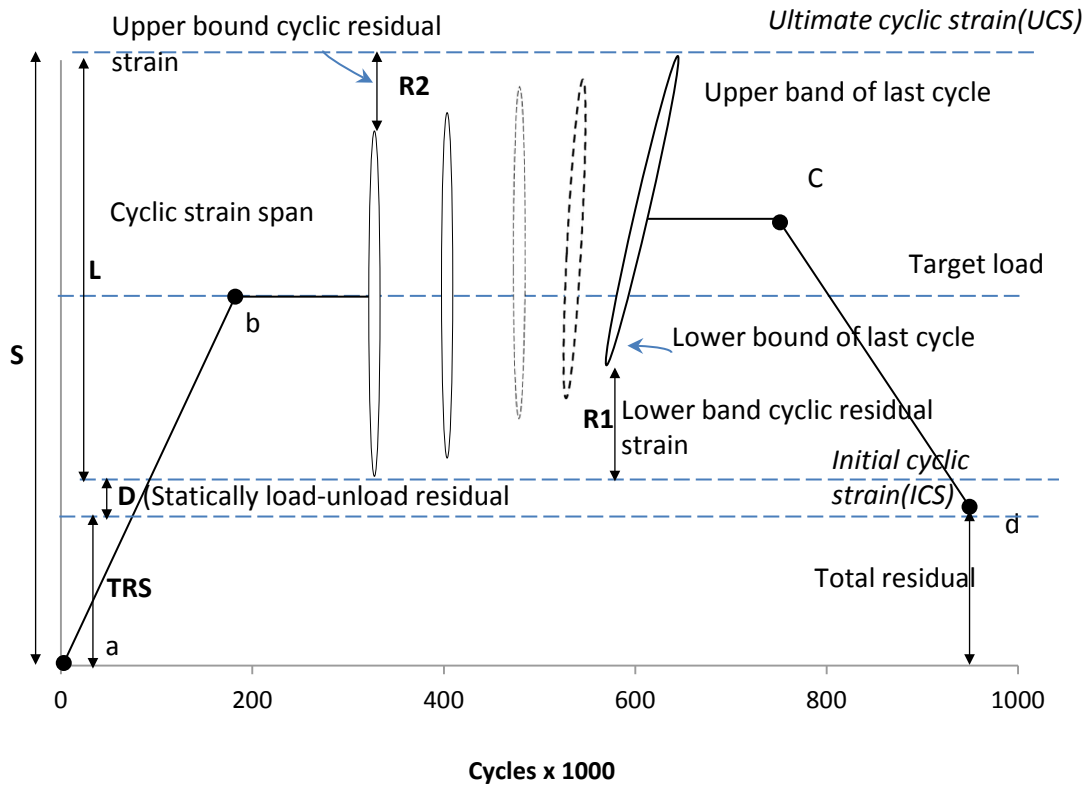

Figure 7-42 Residual strain

The cyclic residual strain encompasses two potential cyclic residual strains (R1, R2). The lower bound cyclic residual strain (R1) is found to be more than the upper bound cyclic residual strain (R2). There is accumulation of the residual strain at the early stages for the lower bound because of the previous loading-unloading cycles. In such a case, more interlocks break and some micro-cracks expand to reach to a stable material connectivity. The magnitude of "D" keeps changing and in real structures as bridge this value may not stabilize. In that case, the superimposed load remains constant and the traffic load is cyclic in nature. Thus the present investigation focuses on

the residual strain initiated by cyclic loading. For more accuracy, the strain at the first and last 2000 cycles was studied.

Equation 7-10 $TRS=S-(L+D)$

Equation 7-11 $L= \text{Max}\ \{ \varepsilon_{(n-2000)}, \varepsilon_n\} - \text{Min}\ \{ \varepsilon_1, \varepsilon_{2000}\}$

Equation 7-12 $S =\text{Max}\ \{ \varepsilon_{(n-2000)}, \varepsilon_n\} - \varepsilon_{offset}$

Equation 7-13 by assuming D=0 in the bridge $TRS=S-L$

ε_i strain at the cycle number i

$TRS=\text{Max}\ \{\varepsilon_{(n-2000)}, \varepsilon_n\} - \varepsilon_{offset} -[\text{Max}\ \{ \varepsilon_{(n-2000)}, \varepsilon_n\} - \text{Min}\ \{ \varepsilon_1, \varepsilon_{2000}\}]$

Therefore:

Equation 7-14 $TRS =\text{Min}\ \{\varepsilon_1, \varepsilon_{2000}\}-\varepsilon_{offset}$

$R1= \text{Min}\ \{\varepsilon_{(n-2000),} \dots, \varepsilon_n\} - \text{Min}\ \{ \varepsilon_{1,} \dots, \varepsilon_{2000}\}$

$R1= \text{Max}\ \{ \varepsilon_{(n-2000),} \dots, \varepsilon_n\} - \text{Max}\ \{ \varepsilon_{1,} \dots, \varepsilon_{2000}\}$

From Figure 7-41:

Equation 7-15 $L= \text{Max}\ \{ \varepsilon_{n,}\} - \text{Min}\ \{ \varepsilon_n\} +R1$

Equation 7-16 $L= \text{Max}\ \{ \varepsilon_{1,}\} - \text{Min}\ \{ \varepsilon_1\} +R2$

Figure 7-43 shows the residual strain accumulated due to fatigue. It is observed from the figure that in the Outdoor condition the maximum residual strain due to cyclic loading comes from R2. The test results show that the value of R1 is about 80-100% more than that of R2. The residual strain is close to about 3% of the ultimate. The residual strain for the Immf specimen could not be computed as the FOS strain sensors did not provide reliable data as discussed earlier.

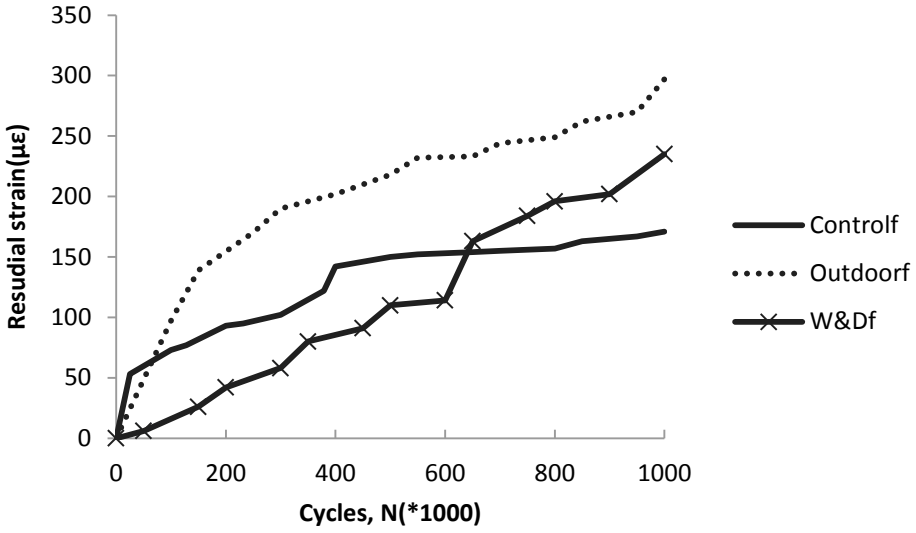

Figure 7-43 Residual strain in different conditions

7.15. Summary

The results of the control and conditioned specimens tested under cyclic loads up to 1 million cycles followed by monotonically increasing static loading until failure of the specimens have been presented in the current chapter. Based on the results presented here, the following observations have been made.

- It is noted that the experimental strains in these cases were within the permissible strain serviceability limit in FRP (2000 με) at the SLS for deflection L/360, which is especially important for the adverse conditions encountered in Outdoor and Immersion or W&D conditioning.
- In terms of the flexural resistance as observed in Figure 7-4 and 7-5, the cyclic loading does not seem to have any serious effect on the Control, Immersion and Outdoor conditions.
- The Immf and W&Df specimens show higher deformability and sustain lower failure load as compared to the Controlf and Outdoorf conditions.
- The following specimens are found to have a lower range of flexural strength as compared to the control specimens: W&D1 (78%), Imm1 (82%) and Outdoor2 (87%). This shows that the effect of different conditioning on the flexural capacity is up to 22% of the M_n value.
- The degree of degradation is found to be more due to the conditioning (alkaline environment) of the specimen than due to fatigue. Degradation due to fatigue loading in the specimens with Immersion and Outdoor conditions is almost negligible. It is observed that the cracks due to cyclic loading do not go through the compressive block of the beam.
- FRP-RC beams were found to have a robust load carrying capacity in all conditions under fatigue, up to the ultimate loading level. The results show that FOS sensors (both FOS-M and FOS-S) performed very well under fatigue and W&D conditions.

- The Immersion specimen performed the worst, while the W&D specimen had the best performance for the serviceability deflection limit. A fitted curve makes it possible to relate the change in deflection due to fatigue cycles considering all the conditions assessed. An emperical formula for the degradation considering all the conditions was developed.
- The values of k_b were calculated after one million load cycles, and the range of the values of k_b were observed to be between 0.78 and 1.07. These values are consistent with the values suggested in the (ACI committee 440.1R-06 2006). Variable fatigue stress makes the cracks grow wider than that in the case of uniform stress. A wide and expanded crack mouth was more tangible during the fatigue test in the case of outdoor conditioning.
- The numbers of fatigue load cycles corresponding to the crack and deflection SLSs was determined from the crack and deflection patterns for the combination of all specimens in fatigue. The crack width SLS and deflection SLS were attained at 800,000 1,100,000 cycles, respectively
- The crack width was found to be 0.6 mm in the case of the control specimen, and 0.4 mm in the case of Outdoorf specimen at the level of 2000 με; while in the cases of Immf and W&Df conditions, the crack width was observed to be 0.2 mm. This means that the alkalinity helped to reduce the crack width by reducing the aggregate friction and interlocking as compared to the control condition. Outdoor conditioning made the cracks grow wider to about double that of the Immersion and W&D conditions.

8. Conclusion & Discussion

8.1. Introduction

Structural Health Monitoring systems are gaining popularity both due to the use of new materials, such as FRP reinforcement, and to notable infrastructure failures in the past decade. Fiber optic sensors represent an improvement in monitoring as they are more robust than traditionally used electric strain gages. In this research, fiber optic sensors were mounted on a short length of supplemental reinforcement that possesses the advantage of installation just prior to concrete placement, therefore preventing damage to both the sensor and the connecting wires. To test the sensor system and the composite material in realistic environments, beam specimens were subjected to three conditions: outdoor exposure (including natural cyclic freezing), continuous immersion in a highly alkaline solution, and cyclic immersion in the same alkaline solution (with periods of drying) and compared with a control specimen. Flexural loading in both static and cyclic (fatigue) were investigated. As few studies have been performed on the fatigue behaviour of FRP bars, this research combines several novel contributions to the field. The results from the strain-stress graphs of the exposed beams are compared with the control sample to determine any degradation due to the presence of alkaline solution and weathering as well as performance of the FOS system. The visual assessment and penetration of alkalis of the FRP

reinforcement was studied using scanning electron microscopy (SEM). An ABAQUS finite element model was developed and validated with the experimental results.

8.2. Achievement of Objectives

The proposed research had four main objectives:

<u>Objective 1</u>: To study the mechanical performance of pre-installed FOSs on a supplementary FRP reinforcement bar attached to the main FRP bar, and then compare the results to more traditional electrical strain gauges.

The test results from strain measurements from FOS-S and FOS-M sensors in all conditions except Imm condition shows good function of sensors and good agreement in static loading (Figure 8-1). As can be seen in Tables 4-5 and Figure 4-19, the ESG did not function in several cases.

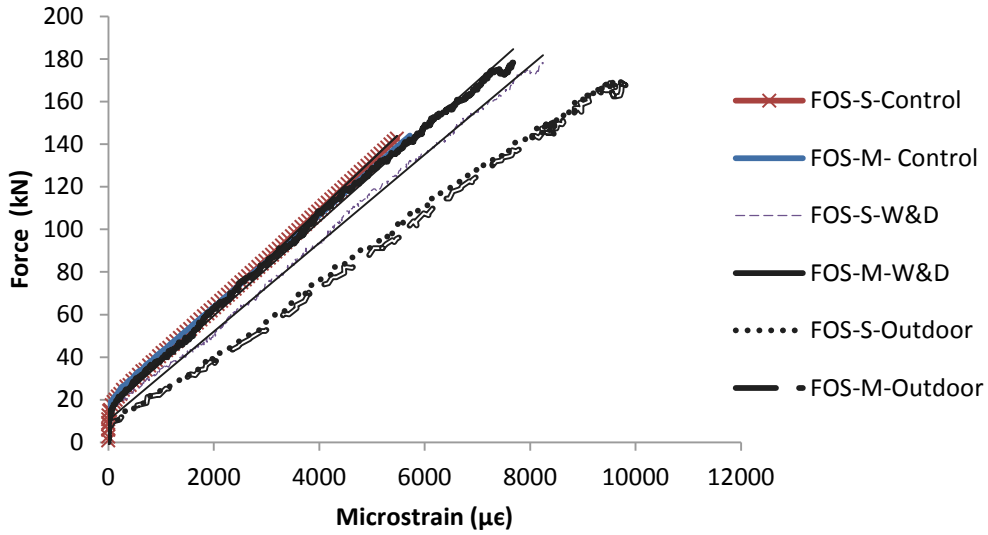

Figure 8-1 FOS function under static loading in W&D, Outdoor and Control conditions

Figure 7-12 to Figure 7-14 shows no change in the function of the FOS-M and FOS-S for the embedded sensor and mounted sensor on the FRP after one million loading cycles. Similar trend observed for the Control and Outdoor condition and no reliable results derived from the strain in Imm condition.

<u>Objective 2</u>: To study the impact of fatigue, weathering, and alkaline solution on this attachment and on the behaviour of the FRP reinforcement in general.

Degradation of the beams with different conditioning after fatigue cycles has been compared in the Figure 7-21, Imm and Outdoor conditions show the most degradation. The ratio of the moment of resistance to the design moment shows that current design is using 50% of the ultimate capacity of the beam.

<u>Objective 3</u>: To study the effects of alkaline solution on the FRP via microstructural testing.

Using SEM, there was apparent visual damage in the immersed reinforcement. As well, using EDX measurements, total alkali concentrations measured on both bare and embedded bars showed moderate to significant increases over the control (unexposed) bare bar. While the bare bar in the immersed condition presented the highest concentrations, embedded bars from the immersed condition showed concentrations three to ten times that of the control bar (Figure 5-14).

<u>Objective 4</u>: To develop a finite element model of a test sample correlated it with the experimental results to study the effect of the key parameters affecting the performance of the supplemental bar-sensor system.

Based on experimental tests, the supplemental rebar and main rebar are provided with appropriate constraints to simulate the strain capture by FOS-S comparable to that observed in the experimental tests for two different beam sizes (

Figure 6-8).

8.3. Conclusions

Based on the study conducted here on the behaviour of FOS in the main and supplemental bars for beams under different loading and environmental conditions, the following conclusions have been made. The conclusions section is subdivided in the following sections based on the types of observations made.

8.4. Major findings

- In the Control, W&D and the Outdoor specimens, the strains in the supplemental bar and the main bar are in good agreement. However, in the Immersion condition, the strain in both the main and supplemental bars is affected severely even with three layers of coatings provided for protecting the sensors.
- The following specimens were found to have lower flexural strength than the control specimen (95%); W&D1 (80%), Imm1 (84%) and Outdoor2 (89%). It shows that the effect of different conditioning on the flexural capacity is up to 20% of M_n.

- In controlling the deflection, the specimen with Immersion condition showed the worst performance, while the one in the W&D condition had the best performance.
- In terms of the flexural resistance as observed in Figure 7-4 to Figure 7-7, the cyclic loading does not seem to have any effect on the Control, Imm and Outdoor conditions.
- The Immersion and W&D specimens show more energy absorption as compared to the other two conditions**.**
- The accumulated deflection and degradation due to fatigue in Imm and Outdoor conditions are more than that in the other conditions.
- All beams were designed for compression failure and over designed for shear failure. The results showed that compression failure is a common mode of failure in most of the conditions. Bond stress increases with the load linearly after reaching M_{cr} up to the ultimate level of loading and it shows that the ESGs installed at the quarter span of the beams worked well in the Control and Outdoor conditions.

8.4.1. SEM Conclusions

- Visual microscopy showed significant damage to fibers for the embedded immersed bar, while the control and W&D showed no damage.
- It can be observed that for an equal period of exposure, the penetration of alkalis as measured by EDX was four times more in the Imm condition than in the case of W&D condition in bare bars. While the immersed embedded bars showed significant penetration on alkalis, the control and W&D embedded bars showed little penetration. The concentration of alkalis in the immersed embedded bar lies between the bare bars in Imm and W&D, which shows efficiency of cover protection in some extent to reduce penetration of alkalis.

- Decreases in alkalinity near the FRP/concrete interface were found more noticeable in the immersion case than the control case.
- Comparing the results, it can be clearly seen that compaction influences the alkali penetration. As the compaction improves, more alkalis are found at the interface.

8.4.2. FEM Study

- The load carrying capacity of the FRP-RC beams is found to be adequate or robust as compared to the design load in all conditions under fatigue up to the ultimate level of loading.
- There was close agreement between the results obtained using the finite element analysis and the experimental tests. The finite models correlated with the results of the experiments provide a reliable baseline mode for parametric study.
- It is observed that the FE model with 19vs6, 19vs10 and 13vs10 produce the strain capture by supplemental bar closer to the experimental results.
- It is observed that Equation 6-4 ($0.6\lambda\sqrt{f_c'}$) and Equation 6-7 ($0.1f_c'$) produce rebar strain close to the measured strain from the experimental study (8000 με) considering various compressive strength in the range of 25-50 MPa.

8.4.3. Fatigue Results

- It is noted that the experimental strains in these cases are within the permissible strain limits in FRP (2000 με) at the mid-span deflection of L/360, which is especially important for the adverse conditions.

- The load carrying capacity of the FRP-RC beams is found to be adequate or robust as compared to the design load in all conditions under fatigue up to the ultimate level of loading.
- The results show that the fiber optic strain sensors on both the main and supplemental bars performed very well under fatigue and W&D, Outdoor and Control conditions , but failed to perform in the case of Immersion due to the alkali-damage to the sensors.
- An extrapolated curve to relate the change in deflection due to long term fatigue cycles considering all conditions has been offered.
- Maximum crack width over a long cycle measured 0.95 mm and in the ultimate case 1mm.
- An empirical formula for the degradation of the FRP-RC beams has been developed by considering the results of all the conditions.
- The values of k_b have been calculated after one million cycles of loads, and the range of the values of k_b are observed to be between 0.78 to 1.07. These values are consistent with the values suggested in the ACI committee (440.1R-06, 2006).
- Variable fatigue stress makes the crack wider than uniform stress. A wide and expanded crack mouth was more tangible during the fatigue test in the case of the outdoor condition.
- A method has been proposed for predicting the number of fatigue cycles corresponding to the service limit stated for crack width and deflection (Span life graph of structure)
- The crack width in the cases of the control and outdoor conditions was found to be 0.6 mm and 0.4 mm, respectively at the level of 2000 με; while in the cases of Imm and

W&D conditions, the crack width is observed to be 0.2 mm. It means that the alkalinity helps reducing the crack width by reducing the aggregate friction and interlocking as compared to the control condition.

8.5. Contributions

The results from this research show that application of an innovative method of reading strain by FOS mounted on supplemental bar is reliable and can be suggested for industry use. Although other authors used similar systems, this was the first to investigate the performance under cyclic loading and environmental conditioning. The system was found to generally function well in static and cyclic loading conditions. However, in extreme cases of alkali exposure, the system may not function properly. Results from SEM helped to clarify that alkalis penetrated into the reinforcement causing visible damage. Unlike most published research in the area, damage was assessed at expected service temperatures. Finite element modelling correlated to experimental results and these models can be utilized by practicing engineers to assess the response of beams of differing dimensions and material properties. Life-span prediction based on crack SLS and deflection SLS, calculation of k_b, bond and comparing mounted sensor results and grooved sensor are all of the outcomes which add to the knowledge. A list of publication arising for the present thesis is provided in Appendix-C.

8.6. Future Work

While the present study reveals some interesting characteristics of the FOS strain sensors with different installation schemes, loading protocols and environmental conditioning, further study is

required to develop a general guideline. Scope for some of the future studies has been identified as follows.

- Full scale beam specimens with more condensed reinforcements need to be studied in order to validate and enrich the present results.
- Continuous superimposed loading can potentially change the crack pattern and deflection. This might have severe impact on the sensor behavior in different condition.
- The effect of different levels of pH should be studied to determine its sensitivity to the alkali-resistance of the FOS and its coating.
- The application of other types of coating and more layers could be an option to consider.
- For the compressive part of the beams, more sensors should be used on the top rebars in different locations to confirm section 8.3.2.
- Different locations and types of the loading need to be considered for the evaluation of the sensor response. Bridge beams in practice are subject to uniform loads due to structure as well as transient loads due to moving vehicles.
- A longer period of conditioning may provide more information about the extent of degradation with the length of exposure to various conditioning agents.
- A change in the loading protocol for the fatigue test with different levels of loading would perhaps affect performance of the beams and the sensors in a different manner from what is observed in the present study. A study on the effect of the loading protocol would further enhance the present findings.
- FRP stirrups should be considered in further studies to investigate deflection, crack, ultimate capacity and failure mode and compared with the steel stirrups.

- Study on modification of design factors with further tests
- The beam specimens tested here are intended for capturing their flexural behaviour and the corresponding performance of the sensors. However, there are other modes of failure, such as diagonal splitting failure and shear compression failure that should also be studied and appropriate sensor arrangement need to be considered for such a study.
- EDX mapping, which indicates quantitative density of elements in the composite, is more accurate than visual study to determine penetration of alkalis. Further study in this regard is suggested.
- In addition to SEM, mechanical tests on FRP reinforcement exposed to alkali would quantify their effect on tensile strength as well as shear. Newly developed ASTM methods should be used.

References

ABAQUS Analysis User's Manual. (2009). Providence, RI, USA: 6.9 ed. Dassault Systemes Simulia Corp.

Achillides, Z., & Pilakoutas, K. (2004). Bond Behavior of Fiber Reinforced Polymer Bars under Direct Pullout Conditions. *Journal of Composites for Construction*, V.8,No.2,pp.173–181.

Ahmed, E., El-Nemr, A., Tremblay, J., & Benmokrane, B. (2011). Laboratory Evaluation of FBG Sensors in Full-Scale Concrete. *Smart Monitoring Assessment Rehabilitation of Civil Structures.* Dubai, UAE.

American Concrete Institute. (2003). *ACI-435R-95,Control of Deflection in Concrete Structures.* Farmington Hills, Michigan: American Concrete Institute.

American Concrete Institute. (2006). *ACI 440.1R-06 ,Guide for the Design and Construction of Structural Concrete Reinforced with FRP Bars.* Farmington Hills, Michigan: American Concrete Institute.

American Concrete Institute. (2008). *ACI 440.2R-08, Structures Guide for the Design and Construction of Externally Bonded FRP Systems for Strengthening Concrete.* Farmington Hills, Michigan: American Concrete Institute.

American Concrete Institute. (2011). *ACI-318-11 ,Building Code Requirements for Structural Concrete.* Detroit, Michigan: American Concrete Institute.

ASCE ,Task Committee on Concrete and Masonry Structure, State of the Art Report on Finite Element Analysis of Reinforced Concrete. (1982). New York, NY: American Society of Testing and Materials.

ASTM International. (2003a). *ASTM C1018, Standard Test Method for Flexural Toughness and First-crack Strength of Fiber-Reinforced Concrete (using beam with third-point loading).* Philadelphia, Pa.: American Society of Testing and Materials.

ASTM International. (2003b). *ASTM-E1131,EStandard test method for compositional analysis by thermogravimetry.* West Conshohocken, Pennsylvania: American Society of Testing and Materials.

ASTM International. (2010a). *ASTM-C31,Standard Practice for Making and Curing Concrete Test Specimens in the Field.* West Conshohocken, Pennsylvania: American Society of Testing and Materials.

ASTM International. (2010b). *ASTM-C39,Standard Test Method for Compressive Strength of Cylindrical Concrete Specimens.* West Conshohocken, Pennsylvania: American Society of Testing and Materials.

ASTM International. (2013). *ASTM-D792,Standard Test Methods for Density and Specific Gravity (Relative Density) of Plastics by Displacement.* West Conshohocken, Pennsylvania: American Standard of Testing Materials.

Bagchi, A., Rivera, E., & Mufti, A. (13-16 November,2007). Evaluation of a Rugged Fiber Optic Sensor System for Monitoring Reinforced Concrete Structures. *The 3rd International Confrence on Structural Health Monitoring of Intelligent Structures(SHMII).* Vancouver.

Bagchi, A.; Murison, E.; Mufti, A.A; Noman, A.S. (2010). Evaluation of Rugged Fiber Optic Sensor System for Monitoring Reinforced Concrete Structure. *Experimental Techniques of Journal of the Society of Experimental Mechanics*, V.34,No. 2, pp.49-53.

Bank, L., & Puterman, M. (1997). Microscopic Study of Surface Degradation of Glass Fiber-Reinforced Polyme Rods Embedded in Concrete Casting Subjected to Environmental Conditioning. In E. Thomas S. Gates and Abdul-Hamid Zureick, *High Temperature and Environmental Effects on Polymeric Composites* (pp. 191-205). American Society for Testing and Materials.

Bank, L., Moshe, P., & Katz, A. (1998). The effect of material degradation on bond properties of fiber reinforced bars in concrete. *ACI Material Journal*, V95 ,No.3.

Benmokrane, B., & Debaiky, A. (2005). *Performance of FOS sensors in Field Application -Val Alain Bridge on Highway 20 East (Québec).* Shebrooke: ISIS Canada.

Benmokrane, B., Rahman, H., Mukhopadhyaya, P., Masmoud, R., Chekired, M., & Nicol, J. (2000). Use of fibre reinforced polymer reinforcemen integrated with fibre optic sensors for concrete bridge deck slab construction. *Canadian Journal of Civil Engineering*, pp. 928-940.

Benmokrane, B., Tighiouart, B., & Chaallal, O. (1996). Bond Strength and Load Distribution of Composite GFRP Reinforcing Bars in Concrete. *ACI Materials Journal*, pp.246-252.

Bott, T., & Barker, A. (1969). The Behavior of Model Composites in Contact with Different Environments. *Chemical Engineering Research and Design*, pp.188-193.

Broomfield, J. (1997). *Corrosion of Steel in Concrete: Understanding, Investigation and Repair.* London: E&FN Spon.

Cachim, P. (1999). Cachim PB. Experimental and Numerical Analysis of the Behaviour of Structural Concrete under Fatigue Loading with applications to concrete pavements. PhD thesis, Faculty of Engineering of the University of Porto, pp.246.

Canadian Standard Association. (2010a). *CSA-A23.3-04(R2010), Design of Concrete Structures.* Rexdale, Ontario: Canadian Standard Association.

Canadian Standard Association. (2010b). *CSA-S807,Specification for Fiber-Reinforced Polymers Canadian Standards Association.* Mississauga: Canadian Standard Association.

Canadian Standard Association. (2011). *CAN/CSA-S6,Canadian Highway Bridge Design Code (CHBCD).* Toronto, Ontario: Canadian Standard Association.

Canadian Standard Association. (2012). *CSA-S806, Design of Concrete Structures.* Rexdale, Ontario: Canadian Standard Association.

Chaallal, O., & Benmokrane, B. (1993). Pullout and Bond of Glass Fiber Rods Embedded in Concrete and Cement Grout. *Materials and Structures*, V.26,pp.167-175.

Chang, P., Faltau, A., & Liu, S. (2003). Review paper: Health Monitoring of Civil Infrastructure. *Structural Health Monitoring*, V.2, No.3, pp.257-267.

Chateauminois, A., Chapert, B., Soulier, J., & Vincent, L. (1993). Effect of Hygrothermal Aging on the Durability of Glass/Epoxy Composites. *Proceeding of the 9th International Conference on Composite Materials*, (pp. 593-600). Madrid.

Chen, Y., Davalos, J. F., Ray, I., & Kim, H. Y. (2007). Accelerated Aging Tests for Evaluation of Durability Performance of FRP Reinforcing Bars for Concrete Structures. *Journal of Composite Structures*, V.78,pp.101–111.

Chu, W., & Karbhari, V. (2002). Characterization and Moisture and Alkali Effects on E-glass/Vinylester Composites. *(CDCC'02)Proceedings of 2nd International Conference on Durability of Fibre Reinforced Polymer (FRP) Composites for Construction*, (pp. 359–369). Montreal, Quebec, Canada.

Colin, D., & Zemp, R. W. (1991). Flexural Fatigue Performance of Steel Fiber Reinforced Concrete, Influence of Fiber Content, Aspect Ratio, and Type. *ACI Materials Journal*, V.88, No.4, pp.374-383.

Construction(CISC), C. I. (2013, Summer). Advantage Steel. *No 46*, p. 37.

Davalos, J. F., Chen, Y., & Ray, I. (2008). Effect of FRP Bar Degradation on Interface Bond with High Strength Concrete. *Cement and Concrete Composites*, V.30, pp.722-730.

Diamond, S. (1981). Effects of Two Danish Flyashes on Alkali Contents of Pore Solutions of Cement Fly Ash Pastes. *Journal of American Ceramic Society*, V.11,pp.383–394.

Ehsani, M. R., Saadatmanesh, H., & Tao, S. (1993). Bond of GFRPRrebars to Ordinary-Strength Concrete. *ACI International Symposium on Non-Metalic Continous Reinforcement*, pp.333-345.

Foote, P. (2009). *Encyclopedia of Structural Health Monitoring.* Bristol,UK: John Wiley & Sons,.

Gheorghiu, C., Pierre, L., & Prou, J. (July 20,2004). Fatigue and Post-Fatigue Performance of Fabry-Perot FOS Installed on CFRP-Strengthened RC-beams. *SPIE(The International Society for Optics and Photonics).* Bellingham,WA.

Goel, S., Singh, S., Singh, P., & Kaushik, S. (2012). Prediction of Mean and Design Fatigue Lives of Self Compacting Concrete Beams in Flexure. *Structural Engineering India*, V.3,No.1,pp.55–61.

Hao, Q.-d., & Wang, Y.-l. Z.-c. (2007). Bond Strength Improvement of GFRP Rebars with Different Rib Geometries. *Journal of Zhejiang University Science*, V.8,No.9,pp.1356-1365.

Issa, M., Khalil, A., Islam, S., & Krauss, P. (2008). Mechanical Properties and Durability of High Performance Concrete for Bridge Decks. *PCI Journal*, V.53,No.4,pp.108-130.

JSCE. (1984). *JSCE-SF4, Method of Tests for Flexural Strength and Flexural Toughness of Steel-Fiber-Reinforced Concrete.* Tokyo, Japan: Concrete library of Japan Society of Civil Engineers (JSCE).

Jungkuist, D. A. (2000). Simulation of Enviro-Mechanical Durability for Life Prediction of E-glass/Vinyl Ester Composites Using a Bridge Service Environment. *M.Sc. Thesis, Virginia Polytechnic Institute and State University*.

Karbhari, V., Chin, J., Hunston, D., Benmokrane, B., Juska, T., & Morgan. (2003). Durability Gap Analysis for Fiber-Reinforced Polymer. *Journal of Composites for Construction*, V.7,No.3,pp.238-247.

Kuang, K., Quek, S., & Maalej, M. (2004). Assessment of an Extrinsic Polymer-Based Optical Fiber Sensor for Structural Health Monitoring. *Measurement Science and Technology*, V.15, pp.2133-2141.

Lee, M. K., & Barr, B. I. (2004). An overview of the Fatigue Behaviour of Plain and Fiber Reinforced Concrete . *Cement & Concrete Composites*, V.26,pp.299–305.

Lianrong, C., Sidney, M., & Dudley R., M. (1994). Specimen Geometry and Toughness of Steel-Fiber-Reinforced Concrete. *Journal of Materials in Civil Engineering*, V.6,No.4,pp.529-541.

Liao, K., Schlthseizz, C., Hunston, D., & Brinson, C. (1998). Long Term Durability of FRP-Matrix Composite Materials for Infrastructure Applications. *Journal of Advance Materials for Infrastructures*, V.30, No.4, pp.3-40.

Lin, X., & Zhang, Y. (2013). Bond–Slip Behaviour of FRP-Reinforced Concrete Beams. *Construction and Building Materials*, V.44,pp.110-117.

Malvar, L. (1998). Durability of Composites in Reinforced Concrete. *1st International Conference on Durability of Fiber-Reinforced Polymer (FRP) Composite for Construction*, (pp. 361-372). Sherbrooke.

Micelli, F., & Nanni, A. (2004). Durability of Concrete Structures. *Construction and Building Materials*, V.18, No.7, pp.491-503.

Mufti, A., Banthia, N., Benmokrane, B., Boulfiza, M., & Newhook, J. (2007). Durability of GFRP Composite Rods. *Journal of Construction International*, V.29, No.2, pp. 37–42.

Neville, A. (1996). Properties of Concrete. New York: John Wiley.

Nkuruziza, G., Debaiky, A., Cousin, P., & Benmokrane, B. (2005). Durability of GFRP bars: A critical review of the literature. *Progress in Structural Engineering and Materials*, Vol. 7, No. 4, pp. 194–209.

Pan, J., & Leung, C. (2007). Effect of Concrete Composition on FRP/Concrete. *Journal of Composites for Construction*, V.11,No.6,pp.611-618.

Ramakrishnan, V., & Lokvik, B. (June,1991). Flexural Fatigue Strength of Fiber Reinforced Concretes. *Proceedings of the International Workshop Held by RILEM, ACI and Others, Mainz, Germany, Vol.15*, (pp. 271–287). London.

Robert, M., Cousin, P., & Benmokrane, B. (2009). Durability of GFRP Reinforcing Bars Embedded in Moist Concrete. *Journal of Composites for Construction*, V.13,No.2,pp.66-73.

Ruscito, G., Nanni, F., Nad, L., & Gusmano, G. (22-24 July 2008). Health Monitoring Performances of FRP Self-Sensing Composite Rods in Concrete Beams. *Fourth International Conference on FRP Composites in Civil Engineering (CICE).* Zurich.

Seitl, S., Keršner, Z., Bílek, V., & Knésl, Z. (2009). Glass Fiber Reinforced Cement Based Composite: Fatigue and Fracture Parameters. *Applied and Computational Mechanics*, V.3,No.2,pp.363-374.

Sim, J., Moon, D., OH, H., & Park, C. (7-9 December 2005). Hybrid FRP Rod for Reinforcement and Smart-Monitoring in Concrete Structure. *Proceedings of the International Symposium on Bond Behaviour of FRP in Structures (BBFS2005)*, (pp. 297-302). Hong Kong.

Stewart, M., & Rosowsky, D. (1998). Time-Dependent Reliability of Deteriorating Reinforced Concrete Bridge Decks. *Structural Safety*, V.20, No.1, pp.91-109.

Subramaniam, K., Ghosn, M., & Ali-Ahmad, M. (2007). Impact of Freeze-Thaw Degradation on FRP-Concrete Interface Fracture. *Advances in Construction Materials*, Part V, pp.419-426.

Suresh, S. (1998). *Fatigue of Materials.* Cambridge: Cambridge University Press.

Swit, G. (2000). Recent Developments in Durability Analysis of Composite Systems. In R. a. Cardon, Fukuda, Balkema, & Rotterdam (Eds.).

Tannous, F., & Saadatmanesh, H. (1998). Environmental Effects on the Mechanical Properties of E-glass FRP Rebars. *ACI Materials Journal*, V.95,No.2,pp.87–100.

The Canadian Network Centers of Exellence on Intelligent Sensing for Innovative Structures. (2007). *ISIS,Reinforceing Concrete Structures with Fiber Reinforced Polymers.* Manitoba, Canada.

Tighiouart, B., Benmokrane, B., & Mukhopadhyaya, P. (1999). Bond Strength of Glass FRP Rebar Splices in Beams under Static Loading. *Construction and Building Materials*, V.13,pp.383-392.

Torkan, B. (2010). Master's Thesis. *Development of a Protection Mechanism for Fiber Optic Sensors in Monitoring GFRP Reinforced Concrete Beams*. Montreal,Canada: Concordia University.

VRod. (2011, Jan.). *Pultall Co.* Retrieved from http://www.trancels.com/images/stories/vrod-gfrp-rebar/V-ROD_Specifications_Feb_2011.pdf

Weather Canada. (n.d.). Retrieved from http://montreal.weatherstats.ca/charts/temperature-1year.html

Won, J., & Park, C. (2006). Effect of Environmental Exposure on the Mechanical and Bonding Properties of Hybrid FRP Reinforcing Bars for Concrete Structures. *Journal of Composite Materials*, V.40, No.12,pp.1063-1076.

Zhang, B., Benmokrane, B., & Nicole, J. (2003). Laboratory Evaluation of Fiber-Optic Sensors for Strain. *Journal of Materials in Civil Engineering*, V.15,pp.381-390.

Zou, Y., & Huckelbridge, A. (2007). Simulation of Crack Growth in FRP Reinforced Concrete. *Journal of Bridge Engineering*, V.12,pp.237-245.

Appendix A

Design Procedure

For designing the 12 beams we follow the design manual (ISIS, 2007)

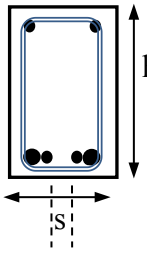

b= S+2×d_b+2cover+2$d_{sup.}$ +2$d_{stirrup}$= S+2×19+2×25+2×6+2×6+

S=38 mm b/h=0.8 Ok.

b=150 mm

As a result: S=38mm which is good space for fresh concrete flow

$\rho_{frp} = \frac{A_{sfrp}}{bd} = \frac{724}{150\times225} = 0.0184$

$\rho_{frpb} = \alpha\beta\frac{\phi_c}{\phi_{frp}}\frac{f'_c}{f_{frpu}}\left(\frac{\varepsilon_{cu}}{\varepsilon_{cu}+\varepsilon_{frpu}}\right) = 0.805\times0.895\times\frac{46}{656}\left(\frac{0.0035}{0.0035+\frac{656}{47.6\times10^3}}\right) = 0.00948$

$\rho_{frp} > \rho_{frpb}$ and $\varepsilon_{frp} = 0.0094 < \varepsilon_{frpu} = 0.0153(\#19)$ and 0.019(#6) (Table 3-1)

we will have compression failure which is desirable.

Equation A1 $F_{frp} = 0.5 \times E_{frp} \times \varepsilon_{cu}\left[\left[1 + \frac{4\alpha\beta\varphi_c f'_c}{\rho_{frp}\ \phi_{frp}\ E_{frp}\ \varepsilon_{cu}}\right]^{1/2} - 1\right] = 449$ N/mm^2

Equation A2 $\varepsilon_{frp} = F_{frp}/E_{frp}$

Equation A3 $M_n = A_{sfrp} \times f_{frpu} \times (d-a/2) = 55.77$ kN.m

a= 52 mm

With regard to ASTM-C78-02 we use the following loading apparatus with 100 mm cantilever part at each side of the supports which is over than 2.5 inches:

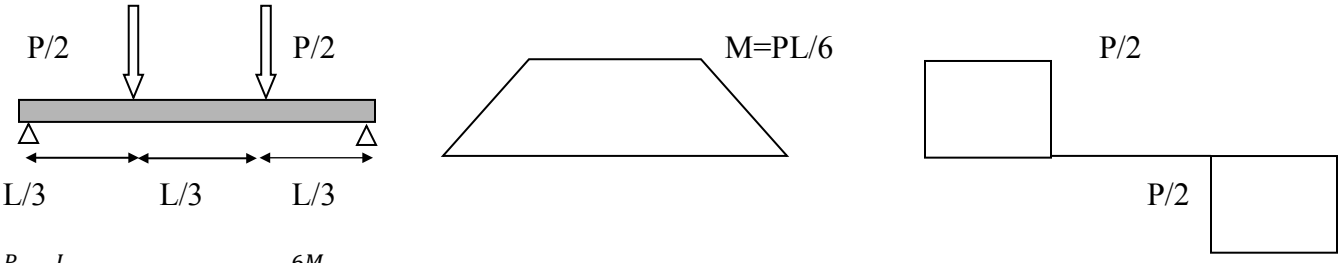

$\frac{P}{2} \times \frac{L}{3} = M_n \qquad P = \frac{6M_n}{L} \quad assume\ L = 1650\ mm \quad P = 202\ kN$

As a result we do test with a RC beam with the following size: 150×250×1750 .This size of beam is somehow light to carry at freezer for freezing-thawing and solution chamber.

Shear Design:

1) dv= max {0.9d, 0.72h} = 194 mm

2)$V_f = \frac{P}{2} = 60$ KN

2)$V_f = \frac{P}{2} = 59.5$ KN

3)$V_{r,max} = 0.25 \emptyset_c f_c' b_w d_v = 0.25 \times 0.65 \times 35 \times 150 \times 194 = 131$ KN $= 165$ kN

4)$V_{r,max} > V_f$ ∴ The section is large enough

5) $V_c = \emptyset_c \beta \sqrt{f_c'} b_w d_v$=065×0.18√35×150×194=20 kN ∴ $V_f > V_c$

6) Determining the maximum stirrup spacing:

a) Based on beam depth: $\frac{V_f}{b_w d_v}=\frac{3.15\times10^3}{150\times180}=0.116$ $\quad \frac{V_f}{b_w d_v} < \frac{V_f}{b_w d_v} < 0.125\lambda\emptyset_c f_c' \Big\} \Longrightarrow$

S_{max}=min {600, 0.7d_v}

$0.125\lambda\emptyset_c f_c'=2.43$

$S_{max}=0.7d_v = 126mm$

b) Based on min. Av $\quad Av_{min} = \frac{0.06\sqrt{f_c}' b_w S}{F_y} \Longrightarrow \quad S_{max} = 56 \times 400/0.06\sqrt{35}\times150=420mm$

Therefore S_{max} from derivations (a) and (b) would be 126 mm.

7) $V_r=V_c + V_s= 20+ \frac{\emptyset_S A_v F_y d_v Cot\theta}{S}$ =166KN >60 kN $\quad V_f < V_r$ Ok.

We use: 150×250×1750 2M19 cover 25 mm $f_c' = 46$ Ok. Stirrup M10 @100mm

Calculation ofM_{cr}:

$$y_t = \frac{bh\left(\frac{h}{2}\right) + (n-1)Ap \times d}{bh + (n-1)Ap} = \frac{150 \times \frac{250^2}{2} + (1.87-1)\times 632 \times 225}{150 \times 250 + 0.87 \times 632} = 126.4mm$$

$$I_t = \frac{1}{12} \times 150 \times 250^3 + 150 \times 250\left(126.4 - \frac{250}{2}\right)\text{^}2 + 0.87 \times 632(126.4-225)^2$$

$$= 2 \times 10^8$$

$$M_{cr} = \frac{f_r I_t}{y_t} = 0.6(46)^{.5} \times 2 \times \frac{10^8}{126.4} = 6.35 \text{ KN. m}$$

$M_{r>}1.5M_{cr}$ Minimum Felxural Resistance checked

$P_{cr} = \frac{6M_{cr}}{L} \rightarrow P_{cr} = 6 \times \frac{M_{cr}}{1.65} = 25.6\ \text{kN}$;

$P_{cr} = 51.3\ \text{kN}$

Minimum thickness of member reinforced with FRP:

According to the code for simply supported reinforced beam by steel: $\frac{L}{h} = 16$

$(\frac{L}{h})_{FRP} = (\frac{L}{h})_s\,(\frac{\varepsilon s}{\varepsilon FRP})^{\alpha d}$ $\alpha d = 0.5$ Rectangular section $(\frac{L}{h})_{FRP}$=16×$(\frac{0.0012}{0.0015})^{0.5}$ =14.31→

$h_{frp} = 105\ \text{mm}$

Used h=225>105 mm Ok.

P_{min} represents the effect of superimposed loads on a bridge(pavement, installation etc.) and preventing impact effect during cyclic loading.

Appendix B

Calculation of Deflection

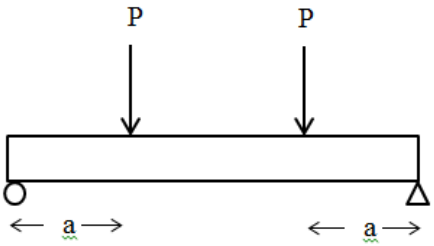

Figure 8-2 Four-point loading on simply supported beam

Equation B 1 $\delta=\frac{Px}{6EI}(3al-3a^2-x^2)$

Equation B 2 $a=L/3 \quad x=L/2: \quad \delta=\frac{5PL^3}{144E_cI_e}$

Equation B 3 $E_c=4500\sqrt{f_c'}$

Equation B 4 $I_g=\frac{1}{12}bh^3$

Equation B 5 $I_t=\frac{1}{12}bh^3+(n-1)A_{frp}(\frac{h}{2}-cover)\approx I_g$

The calculated value are as the following:

f_c'=46 MPa b=150 mm h=250 mm h=225 mm L=1650 mm E_{frp}=47.6 MPa

E_c=30520.485 MPa I_g=195312500 mm^4 I_t=2×10^8 mm^4

Equation B 6 $$I_{cr} = \frac{bd^3}{3}k^3 + n_{frp}A_{frp}d^3(1-k)^2$$ (ACI 440.1R-06)

Equation B 7 $$k = \sqrt{2n_{frp}\rho_{frp} + \left(\rho_{frp}n_{frp}\right)^2} - \rho_{frp}n_{frp}$$

Equation B 8 $$n_{frp} = \frac{E_{frp}}{E_c}$$

Equation B 9 $$\rho_{frp} = \frac{A_{frp}}{bd}$$

Equation B 10 $$I_e = \left(\frac{M_{cr}}{M_a}\right)^3 \beta_b I_g + \left[1 - \left(\frac{M_{cr}}{M_a}\right)^3\right] I_{cr} \leq I_g$$ Benmokrane et al. (1996)

Equation B 11 $$M_{cr} = \frac{f_r I_t}{y_t}$$

Equation B 12 $$\beta_d = 1/5(\rho_{f/}\ \rho_{fb}) \leq 1$$ (ACI 440.1R-06)

Equation B 13 $$\rho_{fb} = \alpha_1\beta_1 \left(\frac{f'_c}{f_{frpu}}\right)\left[\frac{\varepsilon_{cu}}{\varepsilon_{cu}+\varepsilon_{frpu}}\right]$$

The following values applied in the above calculations.

ρ_{frp}=0.0214 A_{frp} =724 mm^2 n=1.559 k=0.227 ρ_{fb} =9.48E-03

I_e=40934228 mm^4 M_{cr} =6359687 N.m α_1 =0.781 β_1 =0.855 β_d =0.452

I_{cr} =40818666 mm^4

I_g moment of inertia of gross section, mm^4

I_{cr} moment of inertia of cracked section transformed to concrete, with concrete in tension ignored, mm^4

M_{cr} cracking moment, N.mm

M_a maximum moment in a member at the load stage at which deflection is being calculated, N.mm

f_r concrete modulus of rapture, MPa

β_b reduction coefficient

E_s modulus of elasticity of steel

ρ_{fb} balanced failure reinforcement ratio

Appendix C

The required anchorage length

The anchorage length calculated using provisions of CSA standard S806-12 as the following:

Equation C1 $$l_d = 1.15 \frac{K_1 K_2 K_3 K_4 K_5}{d_{cs}} \frac{f_F}{\sqrt{f_c'}} A_b > 300\ mm$$

Equation C2 $$d_{cs} < 2.5 d_b$$

Equation C3 $$\sqrt{f_c'} < 5\ MPa \qquad (\sqrt{46} = 6.78 \text{ MPa which 5 MPa will be used})$$

where, K_1, K_2, K_3, K_4 and K_5 are modification factor for bar location, concrete density, bar size, bar fibre and bar surface profile, respectively. Assuming that K_1, K_2, K_4 and K_5=1; K_3=0.8 for #6 and #19, (for $A_b \leq 300$ mm^2), where, A_b is the area of the bar used, and f_F and $f`_c$ represent the design stress in FRP in tension and the concrete compressive strength respectively.

The lever arm d_{cs} is taken as the minimum of the distance from the closest concrete surface to the center of the bar being developed and two-thirds of the center-to-center spacing of the main reinforcement bars.

d_{cs} = *Min* { S+d_6=38 (Appendix A)+6=44 mm×2/3=29.33 and 30 mm(cover)}=29.33 $mm <$ $2.5 d_b = 47.5$

For #19 $l_d = 1.15 \times 0.8 \times 656 \times 283.5/(29.33 \times 5) = 1166$ mm$> 300\ mm$ which it is sufficient for the 1650 mm length of the rebar.

For #6 $l_d = 1.15 \times 0.8 \times 784 \times 28.27/(2.5 \times 6 \times 5) = 271.8$ mm <300 mm so used l_d =300 mm

Appendix D

List of Publications based on the present thesis

Related to these studies the following conference papers have been published to date:

- Rahmatian, A., Bagchi, A., Nokken, M. (2013), "Performance of an Innovative SHM System for RC Flexural Members under Normal and Adverse Environmental Conditions", Ca*nadian Society of Civil Engineers (CSCE).* Montreal.
- Rahmatian, A., Bagchi, A., Nokken, M. (2013), "Modelling Supplemental FRP reinforced concrete in bending using non-linear finite element", *Transportation Research Board (TRB) Annual Meeting,* Washington, DC January 13-17.
- Rahmatian, A., Bagchi, A., Nokken, M. (2012), "Non-linear Finite Element Analysis of Fiber-Reinforced Polymers Rectangular Concrete Beams in Structural Health Monitoring", *6th International Conference on Advanced Composite Materials in Bridges and Structures*, *(ACMBS),* Kingston.
- Deeba, F., Bagchi, A., Rahmatian, A. (2009), "Structural Health Monitoring of Railway Bridges", *Canadian Society of Civil Engineers (CSCE).* St. John's.